

ADVANCES IN CIVIL ENGINEERING

BRIDGE STRUCTURES

GUEST EDITORS: SAMI W. TABSH, AHMAD ITANI, AND HUSAM NAJM





Bridge Structures

Advances in Civil Engineering

Bridge Structures

Guest Editors: Sami W. Tabsh, Ahmad Itani, and Husam Najm



Copyright © 2012 Hindawi Publishing Corporation. All rights reserved.

This is a special issue published in "Advances in Civil Engineering." All articles are open access articles distributed under the Creative Commons Attribution License, which permits unrestricted use, distribution, and reproduction in any medium, provided the original work is properly cited.

Editorial Board

Abir Al-Tabbaa, UK
Serji N. Amirkhanian, USA
Ashraf F. Ashour, UK
William Burgos, USA
Siu-Lai Chan, Hong Kong
Ghassan Chehab, Lebanon
M. C. Deo, India
Ahmed Elghazouli, UK
Polat Gülkan, Turkey
Muhammad Hadi, Australia
Kirk Hatfield, USA
Bassam A. Izzuddin, UK

Tarun Kant, India
Andreas Kappos, Greece
Bryan W. Karney, Canada
Samer Madanat, USA
John Mander, USA
Abolfazl Mohammadian, USA
Ayman Mosallam, USA
Abhijit Mukherjee, India
Manolis Papadrakakis, Greece
Ram M. Pendyala, USA
Jean-Herve Prevost, USA
S. T. Quek, Singapore

Graham Sander, UK
Jun Sasaki, Japan
Rajan Sen, USA
Khaled A. Soudki, Canada
Farid Taheri, Canada
Yaya Tan, China
C. Vipulanandan, USA
Wei-Chau Xie, Canada
Jianqiao Ye, UK
Solomon C. Yim, USA
Ben Young, Hong Kong

Contents

Bridge Structures, Sami W. Tabsh, and Husam Najm
Volume 2012, Article ID 912612, 2 pages

Strain-Based Evaluation of a Steel Through-Girder Railroad Bridge, Andrew N. Daumueller and David V. Jáuregui
Volume 2012, Article ID 145850, 12 pages

Life-Cycle Management Strategy on Steel Girders in Bridges, Kevin K. L. So, Moe M. S. Cheung, and Eric X. Q. Zhang
Volume 2012, Article ID 643543, 14 pages

Optimization of Post-Tensioned Box Girder Bridges with Special Reference to Use of High-Strength Concrete Using AASHTO LRFD Method, Byungik Chang, Kamal Mirtalaei, Seungyeol Lee, and Kenneth Leitch
Volume 2012, Article ID 673821, 8 pages

Structural Behavior and Design of Barrier-Overhang Connection in Concrete Bridge Superstructures Using AASHTO LRFD Method, Byungik Chang, Kamal Mirtalaei, Seungyeol Lee, and Kenneth Leitch
Volume 2012, Article ID 935329, 7 pages

Behavior of FRP Link Slabs in Jointless Bridge Decks, Aziz Saber and Ashok Reddy Aleti
Volume 2012, Article ID 452987, 9 pages

Pounding Effects in Simply Supported Bridges Accounting for Spatial Variability of Ground Motion: A Case Study, G. Tecchio, M. Grendene, and C. Modena
Volume 2012, Article ID 267584, 10 pages

Simple Program to Investigate Hysteresis Damping Effect of Cross-Ties on Cables Vibration of Cable-Stayed Bridges, Panagis G. Papadopoulos, Andreas Diamantopoulos, Haris Xenidis, and Panos Lazaridis
Volume 2012, Article ID 463134, 15 pages

Pile Group Protection with Riprap Mattress, Christian Chretien, Luis Teixeira, and Gonzalo Simarro
Volume 2012, Article ID 693506, 7 pages

Editorial

Bridge Structures

Sami W. Tabsh¹ and Husam Najm²

¹Department of Civil Engineering, American University of Sharjah, Sharjah, UAE

²Department of Civil and Environmental Engineering, Rutgers University, Piscataway, NJ 08854, USA

Correspondence should be addressed to Sami W. Tabsh, stabsh@aus.edu

Received 8 November 2012; Accepted 8 November 2012

Copyright © 2012 S. W. Tabsh and H. Najm. This is an open access article distributed under the Creative Commons Attribution License, which permits unrestricted use, distribution, and reproduction in any medium, provided the original work is properly cited.

The objective of this special issue on bridge structures is to increase the body of knowledge on engineering, construction, and management in relation to bridges. Specifically, it aims at bringing up to date the latest bridge research findings, technical information, and practice on planning, design, construction, maintenance, replacement, management, security, and safety of highway and railroad bridges. The call for papers addressed topics on field monitoring and testing methods, innovative methods for infrastructure construction, high-performance and high-strength materials, bridge design and construction, rating of existing structures, load and resistance factor design, bridge serviceability issues, bridge management systems, aesthetics considerations, and design codes, specifications, and standards.

In response to the call for submissions, 13 papers were received, out of which one paper was later withdrawn. From the remaining 12 papers, 4 papers were rejected and 8 papers were accepted. The papers included in the special issue are on various topics, such as field testing and finite element modeling of a bridge, life-cycle management system, optimization of posttensioned bridges, barrier-overhang connection to bridge decks, FRP link slabs in jointless bridges, pounding effects in bridges with consideration of spatial variability of the ground motion, hysteresis damping effect of cross-ties on cables vibration of cable-stayed bridges, and pile group protection with riprap mattress. Additional details and information on the published papers are provided below.

The paper written by A. N. Daumueller and D. V. Jáuregu is on strain-based evaluation of a steel railroad bridge. It discusses the development of four finite-element models that were developed to study the sensitivity of a bridge in New Mexico to floor-system connection fixity and the ballast.

Accuracy of the computer models was verified through a diagnostic load test based on strain measurement.

Life-cycle management strategy for steel girder bridges is investigated by K. K. L. So et al. This article proposes an integrated life-cycle management strategy on steel girders in bridges in which corrosion deterioration and fatigue damage prediction models are mapped with girders' performance conditions. A practical example to demonstrate the applicability of the proposed strategy is also illustrated.

The paper written by B. Chang et al. addresses cost optimization of posttensioned concrete box girder bridges following the AASHTO LRFD specifications. Design charts were developed with consideration of different span length, section depth, web spacing, tendon profile, and concrete strength. It was observed that high strength concrete enables the achievement of significantly longer span lengths and larger web spacing that is not achievable when using normal strength concrete.

The same authors of the previous paper are also involved in the next one, which is on the structural behavior and design of barrier-overhang connection in concrete bridge superstructures. This investigation addresses the AASHTO's LRFD and standard design methodologies of concrete deck slab, deck overhang, and barrier and combined barrier-bridge overhang. The failure mechanism, design philosophy, and load cases including extreme event limit states for barrier and overhang are discussed.

The paper by A. Saber and A. R. Aleti is on the behavior of fiberglass-reinforced plastic (FRP) link slabs in jointless bridge decks. The study includes numerical analyses and the experimental work to investigate the behavior of the FRP link slab and confirm its feasibility. The results showed

that the technique would allow simultaneous achievement of structural need, lower flexural stiffness of the link slab approaching the behavior of a hinge, and sustainability need of the link slab.

A case study on the pounding effects in bridges with consideration of spatial variability of the ground motion is conducted by G. Tecchio et al. The study includes a parametrical analysis of the seismic response of simple span bridges to asynchronous earthquake ground motion. The analysis considers a series of nonlinear time history analyses, in which the variation of the frequency content in the accelerograms at the pier bases was described by considering the power spectral density function and the coherency function.

P. G. Papadopoulos et al. investigate the hysteresis damping effect of cross-ties on cables vibration of cable-stayed bridges. A short computer program is presented, for the step-by-step dynamic analysis of isolated cables or couples of parallel cables of a cable-stayed bridge, connected to each other and possibly with the deck of the bridge, by very thin pretensioned cross-ties and subjected to various axial forces.

The paper on pile group protection with riprap mattress is written by C. Chreties et al. It contains new experimental data on plan dimensions for riprap mattresses used in pile group protection against edge failure are analyzed. The influence of flow conditions and the distance between piles in plan dimensions of riprap mattresses are addressed, and an alternative methodology for the experimental study of edge failure in pile groups is proposed and verified.

Peer reviewers are key to advancing quality of scholarly journals. As such, the guest editors of the special issue would like to extend special thanks to the many volunteer reviewers who carefully read each of the articles submitted for publication. Their observations and comments have been a great help to both the authors to improve their papers and to the guest editors to make objective decisions with regard to the quality of the submissions.

Finally, we would like to acknowledge the contribution of all authors and hope that the readers find this issue informative and beneficial.

*Sami W. Tabsh
Husam Najm*

Research Article

Strain-Based Evaluation of a Steel Through-Girder Railroad Bridge

Andrew N. Daumueller and David V. Jáuregui

Department of Civil Engineering, New Mexico State University, Hernandez Hall Box 30001, Las Cruces, NM 88003, USA

Correspondence should be addressed to Andrew N. Daumueller, adaumuel@nmsu.edu

Received 2 December 2011; Revised 18 May 2012; Accepted 21 May 2012

Academic Editor: Husam Najm

Copyright © 2012 A. N. Daumueller and D. V. Jáuregui. This is an open access article distributed under the Creative Commons Attribution License, which permits unrestricted use, distribution, and reproduction in any medium, provided the original work is properly cited.

In the state of New Mexico (USA), passenger rail began in 2008 between Belen and Santa Fe on the Rail Runner, following the acquisition of about 100 miles of existing rail and related infrastructure. Many of the bridges on this route are over 100 years old and contain fatigue prone details. This study focuses on a steel through-girder bridge along this corridor. To accurately evaluate these structures for load carrying capacity and fatigue, an accurate analytical model is required. Accordingly, four models were developed to study the sensitivity of a bridge in New Mexico to floor-system connection fixity and the ballast. A diagnostic load test was also performed to evaluate the accuracy of the finite-element models at locations of maximum moments. Comparisons between the simulated and measured bridge response were made based on strain profiles, peak strains, and Palmgren-Miner's sums. It was found that the models including the ballast were most accurate. In most cases, the pinned ended models were closer to the measured strains. The floor beams and girders were relatively insensitive to the ballast and end conditions of the floor-system members, whereas the stringers were sensitive to the modeling of the ballast.

1. Introduction

In the state of New Mexico, the Rail Runner commuter rail service was established in 2008. The state purchased about 100 miles of rail between Belen and Lamy, NM, for this purpose, which transferred responsibility of all related infrastructure to the state. One major responsibility that the state acquired was the periodic inspection and load carrying capacity evaluation of each of the bridges. The goal of this study is to develop analytical models that accurately describe the behavior of a steel through-girder bridge along the route purchased by the state. It was found in the literature that the effects of the end fixity of the floor-system members [1] and the ballast, ties, and rails [2, 3] may be significant. This model will subsequently be used in a fatigue evaluation. This study will also add to the area of evaluating railroad bridges, particularly those under commuter traffic.

1.1. Fatigue. Fatigue is generally evaluated in one of two ways, fracture mechanics or SN methods. Fracture mechanics methods often involve the equation developed by Paris

et al. [4], which relates the rate of crack growth (with respect to the number of stress cycles) to various constants that describe the material and the geometry/type of detail. When rearranged, the Paris equation can yield the number of stress cycles until failure at a given constant amplitude stress range magnitude. This approach is not commonly used for highway and railroad bridges in the U.S. since the corresponding bridge design specifications [5, 6] emphasize the SN method. This method requires curves that relate the stress range magnitude, S , to the number of constant amplitude fatigue cycles, N , that can be withstood by the detail before failure (i.e. SN curves). In the AASHTO [5] and AREMA [6] specifications, various curves are given that describe the fatigue limits for a range of common details. The SN curves provided in the specifications are based on full-sized fatigue tests using a uniform probability of failure.

One issue that must be addressed in using SN curves for bridges is that the curves are developed under constant amplitude stress ranges, whereas real bridge live loads are of variable amplitude since vehicles of varying weight traverse the structure. This issue is commonly addressed in one of

two ways. The first is to determine an “equivalent” constant amplitude stress range, and the corresponding number of cycles. This is done by estimating the stress histories caused by historical truck or train traffic that has crossed the structure. Obtaining accurate stress histories is often one of the most difficult aspects of a fatigue evaluation since a representative structural model is required, along with reliable historical traffic data. Once the stress histories are obtained, further analysis is required to obtain the stress ranges which may be achieved by applying a rainflow algorithm. This analysis is simplified somewhat by the fact that the fatigue model used is typically a linear model, meaning that repeating vehicles only need to be evaluated once, and the result multiplied by the number of stress cycles caused by the vehicle based on the number of crossings. The effective stress range can then be determined as follows, using the root mean cube of stress ranges:

$$S_{Re} = \left(\sum_i \left(\frac{n_i}{N_{total}} S_i^3 \right) \right)^{1/3}, \quad (1)$$

where S_{Re} is the effective stress range; n_i is the number of stress cycles at the i th stress range magnitude; N_{total} is the total number of stress ranges considered; S_i is the i th stress range magnitude. The effective stress range with its corresponding N (N_{total} from (1)) can then be plotted and the suitability for fatigue can be determined based on whether that point lies above or below the corresponding SN curve.

The other common method for performing a fatigue evaluation based on SN curves is based on the equation developed by Palmgren [7] and popularized by Miner [8], known as the Palmgren-Miner’s rule. This is a linear cumulative fatigue estimate as given by the following equation:

$$D = \sum_i \frac{n_i}{N_i}, \quad (2)$$

where D is the Palmgren-Miner’s sum; n_i is the number of stress ranges at the i th stress range magnitude; N_i is the number of stress cycles that can be withstood by the detail at the i th stress range magnitude according to the corresponding SN curve. One advantage of this method is that the remaining life of the structure can be estimated. To do so, the Palmgren-Miner’s sum to date is first determined and the effect of future traffic is then approximated by measuring the strains under live load for a representative period of time to create a “loading block.” The same traffic pattern can then be assumed to repeat indefinitely or increase in volume and/or weight at some assumed rate (e.g., 5% per year). If the traffic is assumed to remain the same, the Palmgren-Miner’s sum of all traffic in the “loading block” can be determined, and the remaining life may be calculated as:

$$T = \frac{D_f - D_h}{D_{LB}}, \quad (3)$$

where T is the time until fatigue failure; D_f is the Palmgren-Miner’s sum at failure; D_h is the Palmgren-Miner’s sum to date; D_{LB} is the Palmgren-Miner’s sum accumulated under



FIGURE 1: Photograph of Rail Bridge at MP 880.37 (Algodones, NM).

the “loading block.” The Palmgren-Miner’s sum at failure is theoretically 1.0; however, some studies have shown that a lower value is appropriate, particularly when the magnitude of the stress ranges increases over time [9].

1.2. Bridge Location and Description. The state of New Mexico’s purchase of the railroad track between Belen and Lamy, NM, to carry the New Mexico Rail Runner required the state to inspect and evaluate all the bridges on the line in accordance with federal regulations [10]. Since many are steel structures over 100 years old, fatigue may be an issue due to the large number of trains that have crossed these structures. Another reason for concern is that the first fatigue provisions entered the AREMA specifications in 1910 after some of these structures were designed [6], including the bridge evaluated in this paper.

The bridge investigated herein is located at milepost (MP) 880.37 near Algodones, NM and carries the railway over an arroyo (see Figure 1). This structure is a ballast-deck, steel through-girder bridge built in 1898. Ballasted decks have a deck that supports crushed stone, which in turn supports the ties and rails on which the trains travel. Through-girder structures consist of two plate girders located on either side of the railway; floor beams are placed transversely and support smaller longitudinal members called stringers, which in turn carry the deck. Currently, this Bridge only carries Rail Runner and Amtrak trains, but historically freight trains and other passenger trains crossed this structure on a regular basis.

The ballast depth of Bridge 880.37 is approximately 25.4 cm from the top of the timber deck to the bottom of the ties based on measurements taken during the last inspection in March 2011. The treated timber ties are spaced 49.5 cm center-to-center and are 16.5 cm high, 21.6 cm wide, and 2.59 m long. The rails are spaced at 1.44 m from inside to inside (i.e., gauge distance) and weigh 67.5 kg/m.

The floor system of bridge 880.37 consists of two 26.67 m long riveted plate girders that are built up using a 2.53 m \times 0.953 cm web plate and two 15.2 cm \times 15.2 cm \times 2.22 cm angles for the top and bottom flanges. Cover plates that are 40.6 cm \times 1.59 cm are also used; at midspan, four cover plates are used on both the top and bottom flanges. The floor beams are also built-up steel members that consist of a 61.0 cm \times 1.43 cm web plate and 15.2 cm \times 15.2 cm \times 2.06 cm double angles. The stringers are rolled steel I 12X35 shapes that are

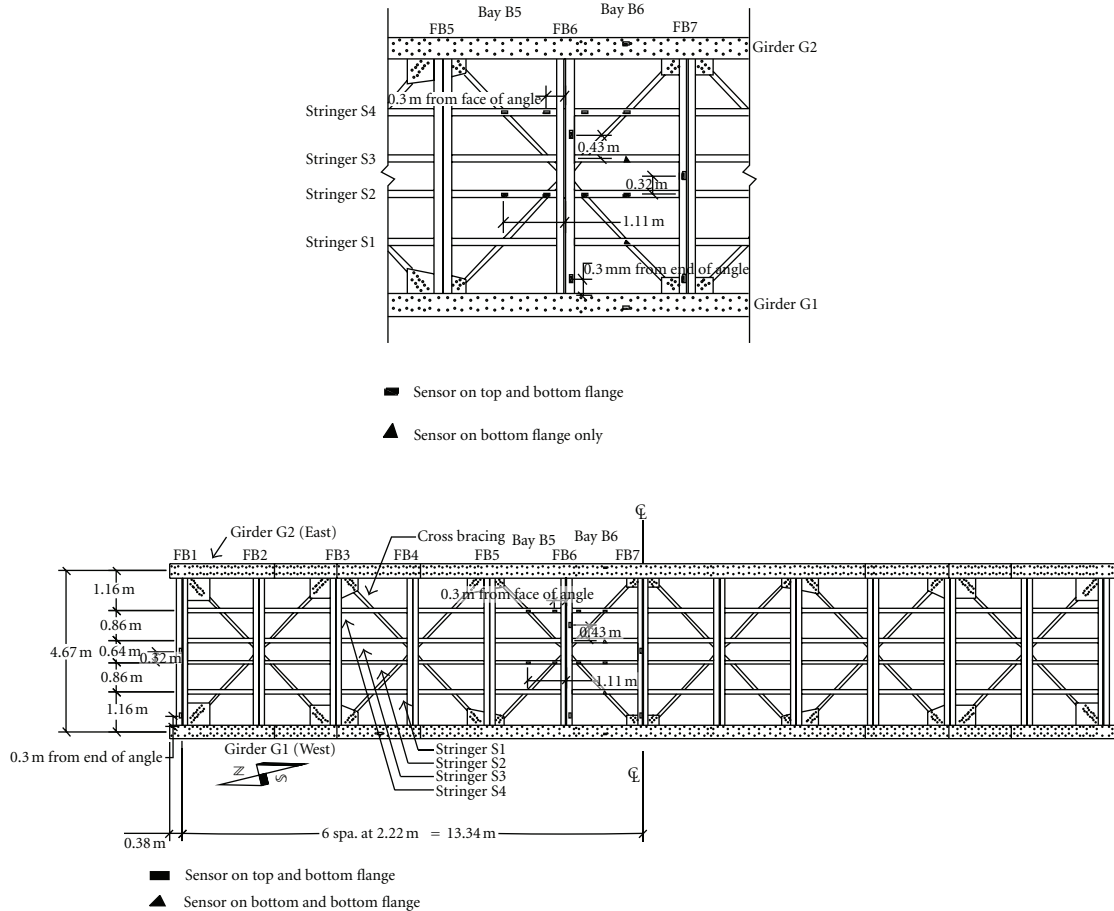


FIGURE 2: Framing plan and sensor locations for Bridge 880.37.

rivet connected to the floor beams using 15.2 cm × 15.2 cm × 1.27 cm double angles. The girders (labeled G1 and G2), floor beams (labeled FB1 through FB13), and stringers (labeled S1 through S4) are shown in Figure 2. All connections are made using rivets with a shank diameter of 2.22 cm.

The deck between the floor beams consists of 14.0 cm × 19.1 cm × 4.27 m treated timbers placed perpendicular to the stringers and resting directly on the top flanges. Over the floor beams, 1.27 cm thick steel apron plates bridge over the top flange so that all loads are distributed to the floor beams via the stringers. Timber ballast curbs are placed along the edges of the deck to ensure that the ballast remains in place.

2. Finite Element Models

Four static linear elastic finite-element models were developed. Models 1 and 2 only included the primary structural members (i.e., girders, floor beams, and stringers). Furthermore, model 1 used pinned connections between floor system elements, while model 2 used fixed connections. Models 3 and 4 were then created to more accurately model the live load distribution by adding the ballast and track structure to models 1 and 2.

2.1. Basic Models. In the basic models (models 1 and 2), the primary structural members of the floor system were modeled with frame elements. All of the frame elements were placed in the same vertical plane to simplify the floor system connections. Nodes were placed at locations of connectivity and approximately 0.152 m spacing for the floor beams and girders. For the stringers, nodes were spaced at 0.305 m intervals and at the connection locations. Moment influence lines were obtained using SAP2000 [11] by using a series of load cases, each with a unit load evenly distributed to the four stringers and representing a 0.305 m movement of the load.

Section properties were calculated for the builtup structural members. Since the girders and floor beams were riveted, the holes needed to be considered. Rivet holes in tension areas were deducted as per AREMA [6], whereas rivets in compression areas were assumed effective. As a result, the gross cross-sectional properties were used to calculate compressive stresses from simulated moments, and the net cross-sectional properties were used to calculate tensile stresses. Table 1 shows the net cross-sectional properties for girders and floor beams, and the gross properties for the stringers used in the basic models.

The moment influence lines for models 1 and 2 at select locations of the floor system members are shown in Figures

TABLE 1: Section properties of the floor system members.

	Area	Torsional constant	I_x	I_y	Major axis shear area	Minor axis shear area	S_x	S_y
	cm ²	cm ⁴	cm ⁴ (*10 ³)	cm ⁴	cm ²	cm ²	cm ³ (*10 ³)	cm ³
Girder X1 ⁺	490.8	196.2	5059	540.7	241.4	174.2	3837	1108
Girder X2 ⁺	513.7	238.7	5384	29611	241.4	200.0	3924	1457
Girder X3 ⁺	560.0	292.9	6215	29611	241.4	264.5	4882	1457
Girder X4 ⁺	674.2	1051	8122	47371	241.4	393.5	6302	2331
Girder X5 ⁺	787.7	3111	10076	65128	241.4	522.6	7724	3205
Girder X6 ⁺	901.9	7122	12078	82888	241.4	651.6	9148	4079
Floor beam	294.7	148.3	170.4	5927	86.64	125.8	5.590	291.7
Stringer	65.81	21.13	9.448	416.2	32.93	32.88	0.6194	20.48

⁺X1 through X6 denotes the different girder cross-sections based on the number of cover plates.

TABLE 2: Section properties of rails and ties.

	Area	Torsional constant	I_x	I_y	Major axis shear area	Minor axis shear area	S_x	S_y
	cm ²	cm ⁴	cm ⁴	cm ⁴	cm ²	cm ²	cm ³	cm ³
Rail	86.00	259.7	3921	601.0	23.47	31.09	462.1	31.05
Ties	356.5	16986	8097	13846	356.5	356.5	980.8	505.0

3 through 5. Comparing moment influence lines for models 1 and 2 shows the sensitivity of the bridge response to the end fixity of the floor system members. It is clear that there was virtually no effect on the girders, and only a small effect on the stringers. The fixity of the floor system connections did not affect the girders because the end conditions of the girders were not changed and therefore acted as a simply supported beam in all cases. The end fixity had the greatest effect on the floor beams, particularly floor beam FB1, which was likely due to bearing restraint. The bearings were modeled as fixed in the transverse direction, and therefore the end condition of floor beam FB1 represented that of a fixed-ended beam. Away from the bearings, the torsional rigidity of the girder plays a significant role in the degree of end-fixity of the floor beams. The moment influence lines for the stringers indicate that sharp peaks should be expected in the simulated strain histories. However, it is anticipated that this model may actually overestimate measured stresses since significant longitudinal load distribution may occur due to the 0.254 m of ballast.

2.2. Refined Models. Two additional models (models 3 and 4) were created that simulate the effect of the track structure and ballast on the distribution of train loads. For models 3 and 4, the ballast, ties, and rails were added to models 1 and 2 (see Figure 6). Table 2 shows the section properties for the rails and ties which were modeled using frame elements.

The ballast was modeled using elastic springs with a stiffness calculated based on the ballast beneath the ties. The ballast under each of the rail ties was assumed to extend a distance of $h/2$ in the longitudinal and transverse directions, where h is the ballast depth (see Figure 7). Assuming linear elastic behavior, Hooke's Law was used to determine the spring constant, which amounted to 506 MN/m. The elastic modulus for the ballast was taken as 137.9 MPa, which is

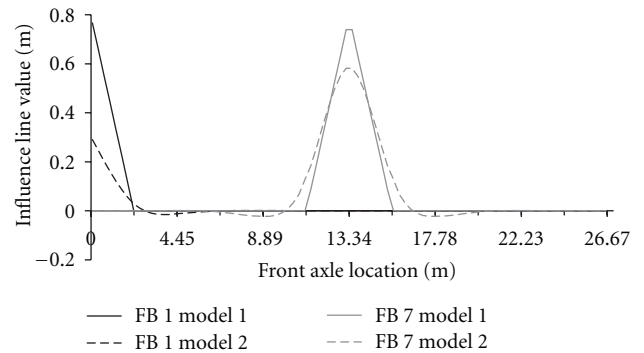


FIGURE 3: Moment influence lines for models 1 and 2 at midspan locations of floor beams FB1 and FB7.

approximately the average of the two values reported by Yang et al. [2] and Kuo and Huang [3] of 100 MPa and 170 MPa, respectively. In the models, the four springs beneath the tie and above each of the stringers were assumed to work in parallel, and therefore 1/4 of the total stiffness or 127 MPa/m was assigned to each spring element. Moment influence lines were created for Models 3 and 4 for comparison with models 1 and 2. Models 1 and 3 are compared in Figures 8 and 9 for the floor beams and stringers, respectively. It is important to note that similar to the connection fixity (see Figure 4), the ballast had essentially no effect on the girder response and therefore no results are shown. Since the girders are insensitive to both the fixity of the floor-system elements and the live-load spreading effect of the ballast, ties, and rails, measurements from the girders may be confidently used in a weigh-in-motion system since there are fewer parameters that affect these strain readings. As shown in Figure 8, the ballast slightly decreased the peak magnitude of the moment influence line of the interior floor beam, however, no change

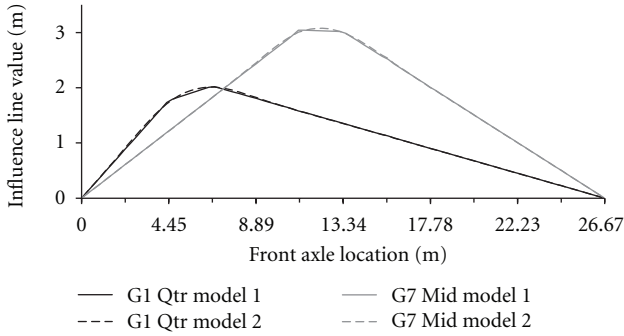


FIGURE 4: Moment influence lines for models 1 and 2 at Bay B6 midspan location and quarter point of girder G1.

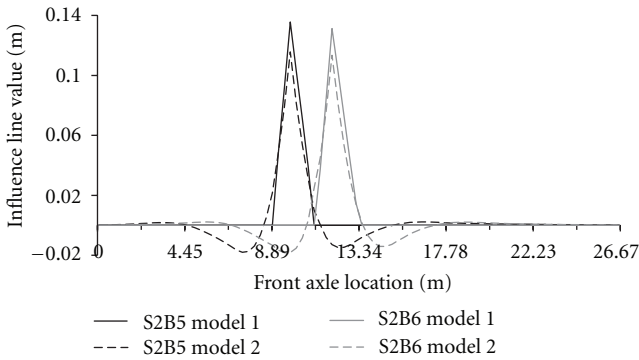


FIGURE 5: Moment influence lines for models 1 and 2 at Bays B5 and B6 midspan locations of stringer S2.

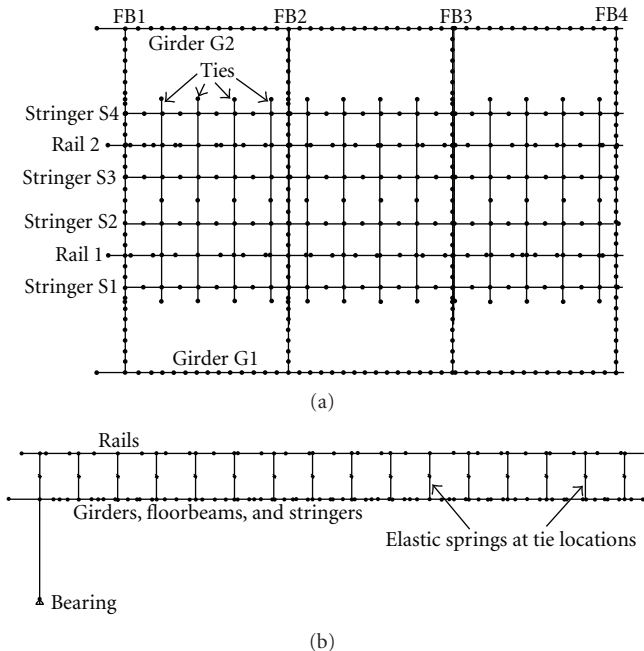


FIGURE 6: Models 3 and 4 of Bridge 880.37 near north support: (a) plan view and (b) profile view.

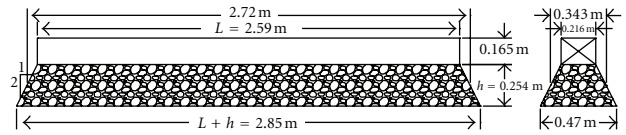


FIGURE 7: Ballast beneath ties used to determine spring constant.

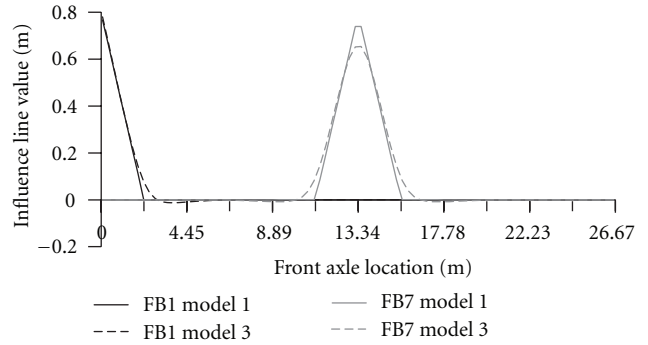


FIGURE 8: Moment influence lines for models 1 and 3 at midspan locations of floor beams FB1 and FB7.

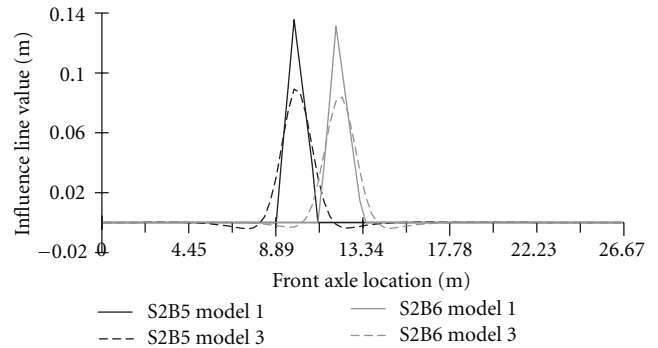


FIGURE 9: Moment influence lines for models 1 and 3 at Bay B5 and B6 midspan locations of stringer S2.

occurred at the end floor beam. The stringers were affected significantly by the modeling of the ballast, track, and rails. This is evident by the large reductions in the peak moment influence line magnitudes shown in Figure 9. Note that compared to the basic model (model 1) where the response is the same for all four stringers, the reduction was greater for the exterior stringers for model 3. The larger response of the interior stringers can be explained by the fact that the ties in the lateral direction act as a continuous beam over four elastic supports. As such, the interior supports support a greater portion of the load when the load is equidistant from the exterior and interior stringer.

2.3. Generation of Influence Profiles. The moment influence lines previously developed were used to simulate strain histories for comparison to measured strains from diagnostic load tests. This was achieved using the following matrix operation: $[M] = [IL] * [L]$, where $[M]$ is the moment history; $[IL]$ is a row vector containing the moment influence

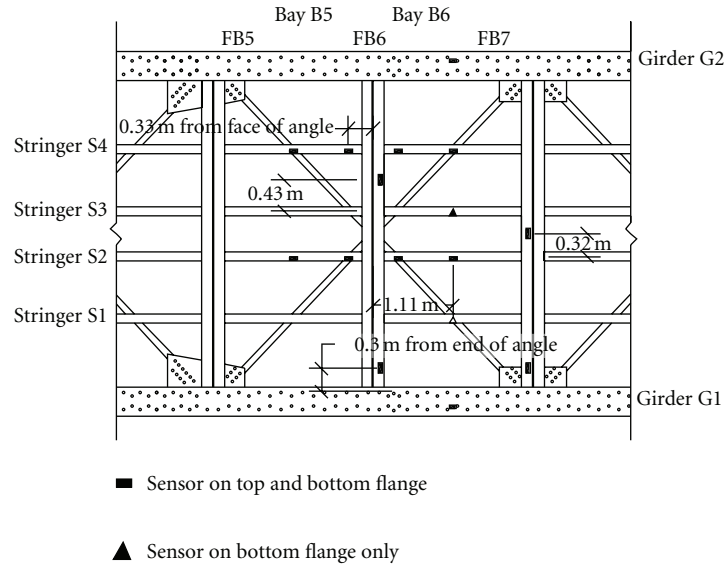


FIGURE 10: Sensor locations in Bays B5 and B6 of Bridge 880.37.

line ordinates; $[L]$ is a loading matrix that represents a moving train. The moment history can be easily converted to a strain history as follows: $[\varepsilon] = [M] / (S * E)$, where $[\varepsilon]$ is the strain history; S is the section modulus for the member; E is the elastic modulus for steel. The loading matrix must be developed carefully to ensure meaningful results. Each row of the $[L]$ matrix represents a longitudinal location which must correspond to each longitudinal location in the $[IL]$ vector. Each column of the $[L]$ matrix represents one load step (i.e., the first column represents the train front axle directly above floor beam FB1, and the 7th column is 1.38 m past floor beam FB1 using a 0.305 m increment). To simplify the matrix, the longitudinal spacing for the moment influence line ordinates should equal the distance the train travels for each load case. Consequently, only the first row of the loading matrix (which represents the train configuration) requires user input. The matrix can be completed by entering a zero in the first column of each row beneath the first, and the remaining cells taken as the value of the cell above and to the left, thus, representing the movement of the train. Further details regarding this process are given in [12].

3. Diagnostic Load Testing

To better understand the load distribution and determine the best-fit model of Bridge 880.37, a diagnostic load test was performed. The sensors used in this study were strain “intelliducers” (which self-identify to the data acquisition system) from Bridge Diagnostics, Inc., (BDI), and the data acquisition system was the Structure Testing System (STS) II equipment and software [13]. The gauges were attached to the bridge by bolting steel tabs to the sensor, which were subsequently attached to the bare steel of the bridge using a strong epoxy adhesive.

3.1. Instrumentation Plan and Setup. The primary purpose of the load test was to capture the live-load distribution of

the structure. Strain transducers were placed near the ends of selected stringers and floor beams to evaluate the level of end fixity of the riveted connections. To assess the longitudinal and transverse load distribution, sensors were placed on all four stringers and both girders near the center of the bridge. Figures 2 and 10 show the sensor locations. The gauges were placed on the bottom of the girders and stringers, the top of the bottom flange for the floor beams, and at the bottom of the top flange for all members where a top sensor is used.

3.2. Train Loading and Testing Procedure. The strain transducers were attached to the structure and connected to junction boxes which were routed to the data acquisition box and laptop computer. Using the BDI testing software, the system was initiated and the sampling rate was set at the maximum of 100 Hz since the trains were traveling at full speed (about 127 kph).

To reduce the effect of temperature and random drift of the sensors, the gauges were rezeroed between trains. Readings initiated on sight of the train and stopped once the last axle of the train exited the structure. A total of six load tests were completed under six different trains as described in Table 3. Axle weights and spacings were extracted from Dick [14] except those for the Rail Runner locomotive which were found on the manufacturer’s website [15]. Table 4 and Figure 11 describe the train configurations applied in the load tests.

3.3. Processing of Strain Measurements. The raw strain data was first cropped and then corrected for drift and adjusted for a time lag that was observed in 20 of the sensors due to a recording delay between the channels of the data acquisition system. To crop the data, the measurements taken at floor beam FB1 were used to determine when the train had entered the structure for southbound trains or when the train had travelled the length of the bridge for northbound

TABLE 3: Observed configurations of trains used in load tests.

Train Number	Train type	Time of crossing	Direction	Configuration
1	Rail runner	12:30 PM	Southbound	1 engine; 3 passenger cars
2	Amtrak	3:10 PM	Southbound	2 engines; 1 baggage car; 4 coach; 1 diner; 1 lounge; 3 sleepers
3	Rail runner	4:45 PM	Northbound	3 passenger cars; 1 engine
4	Rail runner	5:05 PM	Southbound	1 engine; 4 passenger cars
5	Rail runner	5:59 PM	Northbound	2 passenger cars; 1 engine
6	Rail runner	6:15 PM	Southbound	1 engine; 3 passenger cars

TABLE 4: Engine and rail car configurations.

	Weight per axle kN	LPFC* m	AS* m	TC* m
Rail runner engine	322	20.7	2.74	13.1
Rail runner passenger car	122	25.9	2.90	19.5
Amtrak engine	296	21.0	2.75	13.2
Amtrak baggage car	133	25.9	1.68	18.1
Amtrak coach and lounge	178	25.9	2.59	18.1
Amtrak diner and sleeper	189	25.9	2.59	18.1

* Abbreviations defined in Figure 11.

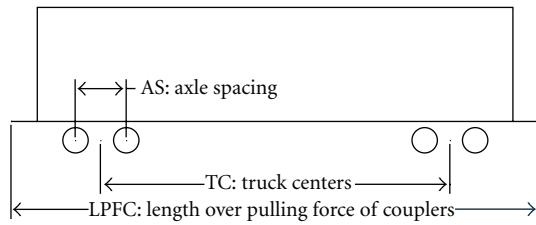


FIGURE 11: Definitions of abbreviations in Table 4.

trains. Sensor drift was then corrected using the following relationship:

$$\epsilon_{n'.adj} = \epsilon_{n'.measured} - \epsilon_0 + \frac{n'}{N'} * (\epsilon_{N'} - \epsilon_0), \quad (4)$$

where $\epsilon_{n'.adj}$ is the adjusted strain reading; $\epsilon_{n'.measured}$ is the raw measured strain; ϵ_0 is the average strain before the train enters the structure; n' is the reading number; N' is the total number of readings between the train front axle entering and the last axle leaving the bridge; $\epsilon_{N'}$ is the average strain after the last axle leaves the structure.

As mentioned previously, a time lag was observed in 20 of the 36 sensors and at one location, the strain readings on the top and bottom flanges were offset. Since the time between the first peaks in the readings represented the time lag, the lagging data was simply shifted to the left. Figure 12 shows an example strain data set for a stringer before and after processing.

3.4. General Behavior Based on Measured Strains. The measured strains for each of the six trains at all 19 instrumented locations were processed as discussed in Section 3.3. In general, the shapes of the strain histories were as expected

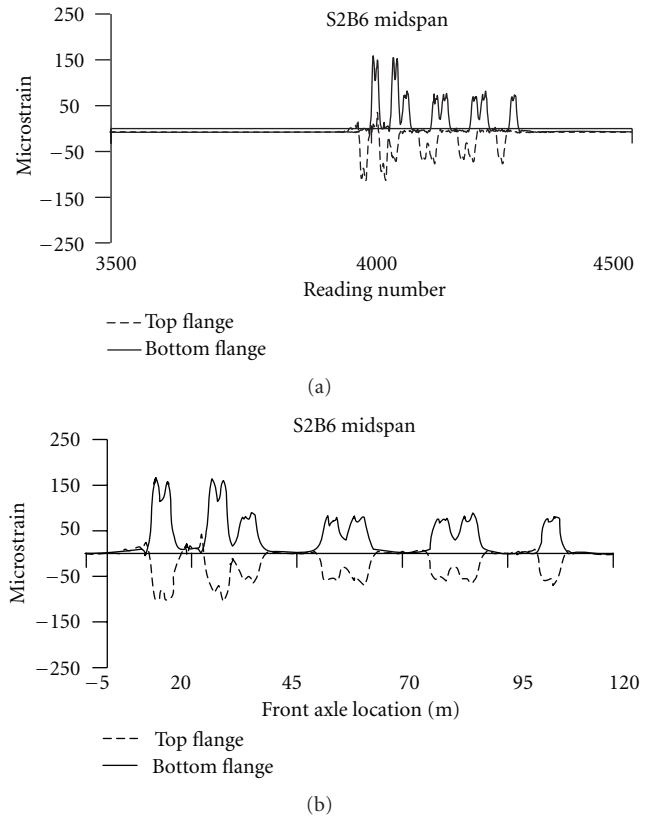


FIGURE 12: Typical response for stringer S2 at Bay B5 midspan: (a) raw strain data and (b) processed strain data corrected for drift, time lag, and axle location.

(e.g., a peak for each set of axles and peaks of similar magnitudes for each rail car). In Bay B6, the peak strain magnitudes were smallest in stringer S1 and largest in stringer S4, consistently increasing from west to east, as shown in Figure 13. This behavior was only observed under the locomotive, and possibly attributed to asymmetric weight distribution, or some dynamic effect of the diesel engine. Another observation was that tensile stresses developed in the stringers, particularly in Bay B5. At the instrumented ends of these stringers, pure tension was measured and at midspan, the tension flange strains were significantly larger than the compression flange strains. Similar behavior was observed in Bay B6, but to a smaller extent. This can be

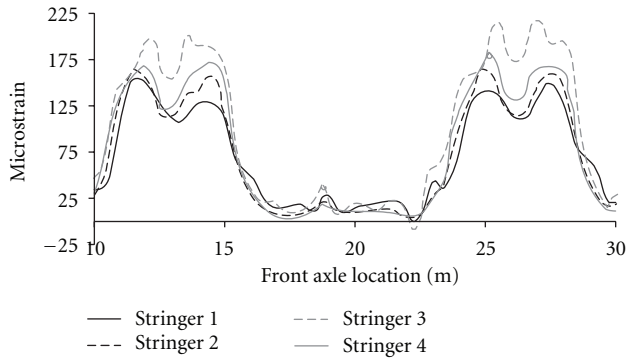


FIGURE 13: Illustration of asymmetric live-load distribution under the locomotive for Train 1.

TABLE 5: Neutral axis positions determined from drawings and strain measurements.

	From drawings	From strain data	Difference (%)
	cm	cm	%
Floorbeams	30.5	31.2	2.9%
Girder X5	132	123	-6.3%
Girder X6	133	131	-2.0%
Stringers	15.2	18.5	21.5%

Note: Neutral axis locations taken from bottom of member.

explained by the fact that the stringers behave in conjunction with the girders and resist some of the tensile flexural stresses that would otherwise be resisted by the girder bottom flanges.

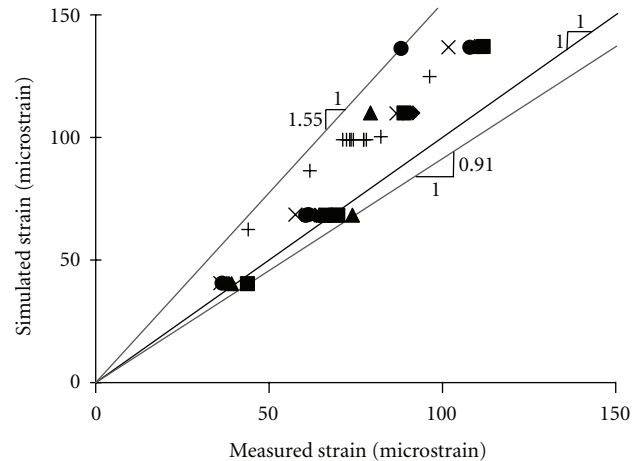
Assuming linear strain distribution, the neutral axis positions were estimated at all locations where strains were measured at the top and bottom flanges. The average measured neutral axis positions are given in Table 5 compared to those calculated from the as-built plans. For the girders and floor beams, the average neutral axis locations based on strain measurements were close to the values obtained from the drawings. For the stringers, the average neutral axis location based on measured strains was significantly higher, which can be explained by the behavior discussed earlier, and partial composite action with the deck. It was also observed that minimal negative flexure developed at the ends of the stringers and floor beams with two exceptions: the stringers in Bay B5 and floor beam FB1. This may indicate negative flexure, since the instrumented location may have been near the points of inflection.

4. Evaluation of Best-Fit Model

The finite-element models were evaluated by comparing the shapes of the simulated and measured strain profiles, and also the peak strains from each passing train. It was found that the actual train speeds varied from 125 kph to 126 kph. The models were further evaluated based on Palmgren-Miner's sum for future use in a fatigue evaluation.



(a)



(b)

FIGURE 14: Simulated (Model 1) versus measured response near midspan of girder G2: (a) strain profiles for Train 1 and (b) peak strains for all trains.

4.1. Measured versus Simulated Girder Strains. Figure 14 shows the simulated versus measured strains near midspan of Girder G2 for model 1 since all four models behaved nearly the same. As shown in Figure 14(a), the strains match very well under Train 1, particularly for the rail cars, which are represented by the three smaller peaks in the data. For all the trains, it is also apparent that the locomotive weights may have been overestimated since the simulated strains consistently exceeded the measured strains under the locomotives as shown in Figure 14(b) (locomotive strains are represented by the first peak in the strain data). For the Rail Runner trains, the peak strain correlation was very close to the 1:1 line for the passenger cars, but as much as 1.5:1 for the locomotives. For the Amtrak train, both the locomotive and passenger cars showed higher simulated strains compared to the measured strains. The difference between the measured and simulated strains may be attributed to differences in the actual weights of the rail equipment when compared to the estimated weights taken from the manufacturer, which were used when developing the simulated strain histories.

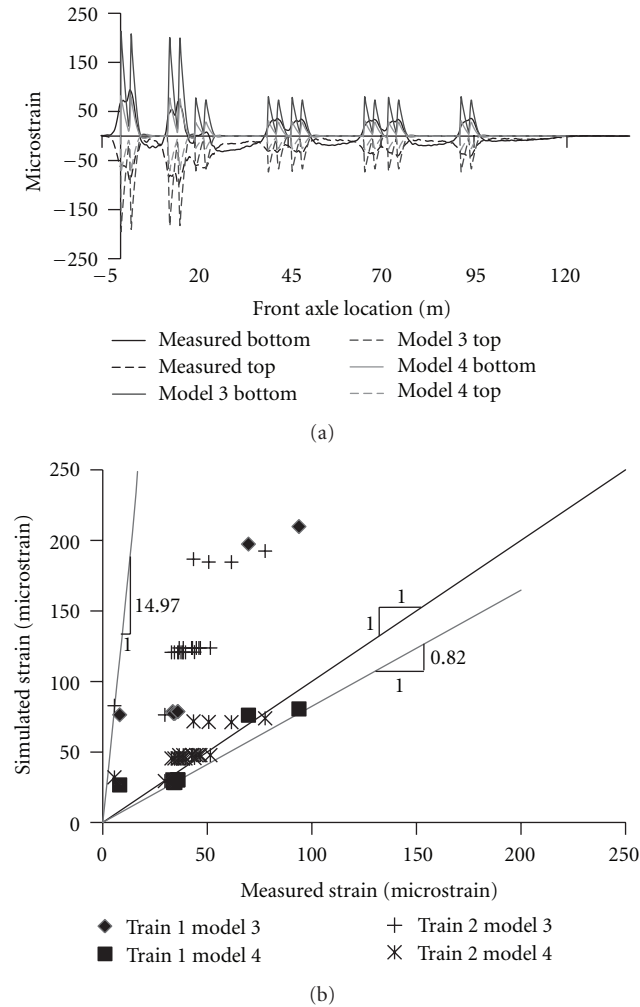


FIGURE 15: Simulated versus measured response at midspan of floor beam FB1: (a) strain profiles for Train 1 and (b) peak strains for Trains 1 and 2.

4.2. *Measured versus Simulated Floor Beam Strains.* Similar comparisons were made for the floor beams however, unlike the girders there were differences between the models. For the end floor beam FB1, the simulated response was significantly affected by the end fixity. As shown in Figure 15, the pinned connection model (i.e., model 3) significantly overestimated the measured strains whereas the fixed connection model (i.e., model 4) resulted in a very close agreement of peak strains, although the model does yield some results below the 1 : 1 line.

For the interior floor beams (FB6 and FB7), it was found that the influence of the end-fixity and ballast was minimal. The pronounced effect of the end-fixity on the end floor beam compared to the interior floor beams can be attributed to the bearings and torsional rigidity of the girders as mentioned earlier. None of the floor beams were affected significantly by the modeling of the ballast, ties, and rails. This is logical since, assuming the load is spread over a relatively small distance, the difference in the distribution to the floor beams is small. The results from this section

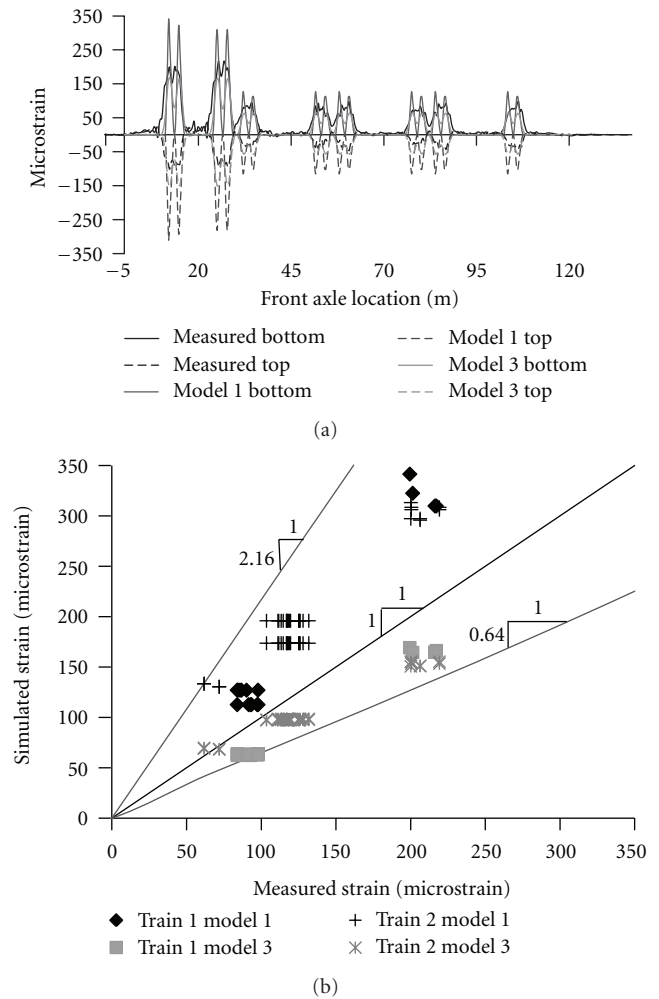


FIGURE 16: Simulated versus measured response at midspan of Stringer S4 in Bay B6: (a) strain profiles for Train 1 and (b) peak strains for Trains 1 and 2.

show potential in guiding a bridge inspector to locations that are more likely to experience fatigue related failure since it was shown that the end floor beam may develop negative moments at the ends, thus, causing stresses that were not likely considered in design.

4.3. *Measured versus Simulated Stringer Strains.* The strain comparisons are given in Figure 16 for Stringer S4 at the midspan of Bay B6. This location was chosen since the maximum measured stringer response occurred here. models 1 and 3 were compared since the stringers were more sensitive to load spreading through the ballast than end-fixity. Models 2 and 4 resulted in lower strains than models 1 and 3, respectively. The shapes of the curves also match much better when the pinned-end models are used. Based on the strain profile comparisons, model 3 appears to more accurately capture the shape of the measured strains and the peak magnitudes, although the results fell below the 1:1 line. For this model, the simulated strains for the interior stringers were greater than those for the exterior stringers. If the

TABLE 6: Palmgren-Miner's sums based on measured and simulated strains.

	Miner's sums					Difference from measured (%)			
	Measured (*10 ⁻⁹)	Model 1 (*10 ⁻⁹)	Model 2 (*10 ⁻⁹)	Model 3 (*10 ⁻⁹)	Model 4 (*10 ⁻⁹)	Model 1	Model 2	Model 3	Model 4
Train 1									
G1B3 midspan	1.27	2.26	2.32	2.26	2.31	78%	83%	78%	82%
G2B6 midspan	2.48	4.10	4.19	4.11	4.18	65%	69%	66%	68%
FB1 midspan	4.14	53.7	2.7	51.0	2.96	1196%	-34%	1131%	-29%
FB7 midspan	5.38	26.2	24	22.6	26.1	387%	348%	319%	385%
S2B6 midspan	1.30	17.0	8.51	3.11	1.99	1205%	555%	139%	53%
S4B6 midspan	2.72	17.0	7.93	1.43	0.85	524%	192%	-47%	-69%
Train 2									
G1B3 midspan	2.47	4.62	4.58	4.52	4.55	87%	86%	83%	84%
G2B6 midspan	4.09	7.95	7.92	7.81	7.90	94%	94%	91%	93%
FB1 midspan	10.4	152	8.1	150	8.86	1369%	-22%	1349%	-15%
FB7 midspan	12.3	80.1	66	64.2	67.6	551%	434%	422%	450%
S2B6 midspan	3.87	50.8	29.9	9.51	7.32	1211%	674%	146%	89%
S4B6 midspan	7.68	50.8	27.1	4.36	3.13	560%	253%	-43%	-59%

* G1B3 indicates girder G1 in Bay B3; G2B6 indicates girder G2 in Bay B6; S2B6 and S4B6 indicate stringers S2 and S4, respectively, in Bay B6.

maximum stringer response from model 3 (i.e., the response for an interior stringer) is compared to the measured strains at stringers S4, bay B6 midspan (as shown in Figure 16), the simulated strains more closely approximate the measured strains, and the slope of the lower-bound line is 0.81 rather than 0.64.

Modeling the stringers requires greater care than the modeling of the girders and floor beams since the stringers are sensitive to both the end-fixity and to the modeling of the ballast, ties, and rail. Correctly modeling the end-fixity is also more difficult for the stringers than for the floor beams since the level of fixity is affected by the rigidity of the double angle connections and the out-of-plane rigidity of the floor beam web. The potential contribution of the stringers in tension and the possibility for partial composite behavior with the deck also must be considered. Considering the many factors affecting the behavior of the stringers, the results from the finite-element models described the measured behavior quite well.

4.4. Comparisons Based on Palmgren-Miner's Sums. Apart from the comparisons of strain histories and peak strains, the Palmgren-Miner's sums were determined to further evaluate the models. For Bridge 880.37, the critical fatigue details for the girders and floor beams are classified as category D based on the AREMA specifications [6] and category A for the stringers away from the connections. To obtain the Palmgren-Miner's sums, the strain histories were first converted to stress histories (by multiplying by the modulus of elasticity) which were then processed using a rainflow counting algorithm [16] developed in MATLAB [17] to determine the stress range magnitudes and corresponding number of stress cycles. Subsequently, the

Palmgren-Miner's sums were determined using the following equation:

$$D = \sum_1^k \frac{n_i}{N_i} = \sum_1^k \frac{n_i}{n_o} * \left(\frac{\Delta\sigma_i}{\Delta\sigma_o} \right)^3, \quad (5)$$

where D is the Palmgren-Miner's sum; n_i is the number of stress cycles at the i th stress range magnitude; $\Delta\sigma_i$ is the i th stress range magnitude; n_o is the number of cycles at the knee point of the SN curve; $\Delta\sigma_o$ is the stress range at the knee point; k is the number of different stress cycles. For the riveted details, n_o is 6 million cycles and $\Delta\sigma_o$ is 48.2 MPa as specified in AREMA [6] and for the stringers away from the connections, n_o is 2 million cycles and $\Delta\sigma_o$ is 165 MPa.

The Palmgren-Miner's sums based on the measured and simulated strains vary widely between models and between different locations for the same model (see Table 6).

Results are only shown for Trains 1 and 2; however, the trends and percentage of differences are consistent from train to train. The percentage of difference indicates the percentage of difference between the measured and simulated Palmgren-Miner's sum for a particular location. The pinned connection models (i.e., models 1 and 3) have higher Palmgren-Miner's sums than the fixed connection models (i.e., models 2 and 4) for the stringers and end floor beam locations. Models 3 and 4 have lower Palmgren-Miner's sums than Models 1 and 2 for the stringers because of the load spreading effect. Floor beam FB1 appears to be the least accurately depicted by the pinned connection models. At this floor beam, the Palmgren-Miner's Sum based on measured strains was much smaller. In addition, the Palmgren-Miner's sums based on simulated strains for floor beam FB1 were double the corresponding values for an interior floor beam. This behavior is mainly

attributed to the larger degree of end-fixity developed at the end floor beam compared to the interior floor beams as discussed earlier. Thus, the fixed connection models match the measured data the best for the end floor beam.

At S4B6 midspan, model 3 underestimated the Palmgren-Miner's sum based on measured strains; however, if this model was used in an engineering analysis, the most critical stringer would be used, since the member with the highest stress ranges would be the critical member in the analysis. The critical stringer location using model 3 is S2B6 midspan and S4B6 midspan for the measured strains. If these Palmgren-Miner's sums are compared then model 3 is conservative by 14% for Train 1 and 24% for Train 2, which would yield very good results in a fatigue evaluation. The Palmgren-Miner's sums for the girders and interior floor beam were very similar from model to model, signifying insensitivity to the end-fixity of the floor-system members and the ballast modeling, and model 3 appeared to be the closest to the measured values. The models overestimated the Palmgren-Miner's sum by 65% to 94% for Girders G1 and G2, and by 319% to 551% for Floor beam FB7. More accurate locomotive weights would likely lead to greater convergence between the simulated and measured behavior.

5. Conclusions and Future Work

Based on the four models, it was found that those which consider the ballast, ties and rails perform better than the simpler models. For the girders and interior floor beams, the difference in response for the four models was small since these members were insensitive to the end-fixity of the floor-system members and to the modeling of the ballast, but model 3 was found to give the best results. This insensitivity to the parameters mentioned indicates that measurements taken at the girders may be useful in a weigh-in-motion system since only the axle weights will likely affect the measurements significantly. For the end floor beam, model 4 was closest to the actual response and model 2 also gave reasonably accurate results. There was a significant difference between the pinned and fixed ended models for the end floor beam due to the stiffness of the bearing in the transverse direction. Based on these results for the girders and floor beams, the level of analysis had a small impact on the accuracy of the simulated responses. Therefore, a relatively simple model is sufficient if only the girders and floor beams require evaluation; however, a slight improvement is achieved when the ballast, ties, and rails are included in the model.

The stringers were sensitive to both the end-fixity and the modeling of the ballast. It was found that if the critical stringer is evaluated, model 3 provides the most accurate results, particularly if a Palmgren-Miner's sum is desired for a fatigue evaluation. Although the stringers require a more complex model, it may not be required in many cases when evaluating fatigue. Based on the results of this study, the end-fixity of the stringers is minimal, and, therefore, the stress ranges at the ends are likely to be small, thus, the midspan of the member is critical for fatigue. Since the stringers are rolled steel shapes, they are relatively unsusceptible to

fatigue failure, and as such an analysis utilizing a simple, yet significantly conservative model may be sufficient to indicate that the stringers are unlikely to pose a fatigue-related risk. For the end floor beam, in spite of being closer to the actual response, the simulated values were at times underestimated. This can be remedied by applying a factor that accounts for the modeling error. Furthermore, if this model was used in a fatigue evaluation using the AREMA [6] specifications, factors would also be applied to account for vertical impact and rocking effects.

Work based on this study, including a fatigue evaluation of Bridge 880.37 to estimate the remaining fatigue life is published elsewhere [18]. To achieve this, representative trains were developed for various eras dating back to the construction of the bridge, which were used along with the known current train traffic. These loads were then applied to the most accurate models, as determined in this paper. The matrix multiplication discussed in Section 2.3 can be rearranged to obtain the moment influence line for a specific location based on strain measurements. These influence lines can then be used to observe changes in the live load distribution of the bridge that may indicate structural damage. The moment influence lines can also be used in lieu of analytical models for evaluating the bridge under historical loading [18].

References

- [1] M. Al-Emrani and R. Kliger, "FE analysis of stringer-to-floor-beam connections in riveted railway bridges," *Journal of Constructional Steel Research*, vol. 59, no. 7, pp. 803–818, 2003.
- [2] L. A. Yang, W. Powrie, and J. A. Priest, "Dynamic stress analysis of a ballasted railway track bed during train passage," *Journal of Geotechnical and Geoenvironmental Engineering*, vol. 135, no. 5, pp. 680–689, 2009.
- [3] C. M. Kuo and C. H. Huang, "Two approaches of finite-element modeling of ballasted railway track," *Journal of Geotechnical and Geoenvironmental Engineering*, vol. 135, no. 3, pp. 455–458, 2009.
- [4] P. C. Paris, M. P. Gomez, and M. E. Anderson, "A rational analytical theory of Fatigue," *Trends in Engineering*, vol. 13, pp. 9–14, 1961.
- [5] AASHTO, *LRFD Bridge Design Specifications*, American Association of State Highway and Transportation Officials, Washington, DC, USA, 5th edition, 2010.
- [6] AREMA, *Manual for Railway Engineering*, American Railway Engineering and Maintenance-of-Way Association, Lanham, Md, USA, 2007.
- [7] A. Palmgren, "Die Lebensdauer von Kugellagern. (The life of roller bearings)," *Zeitschrift des Vereines Deutscher Ingenieure*, vol. 68, no. 14, pp. 339–341, 1924 (German).
- [8] M. A. Miner, "Cumulative damage in fatigue," *ASME Journal of Applied Mechanics*, vol. 12, no. 3, pp. A159–A1964, 1945.
- [9] H. Agerskov, "Fatigue in steel structures under random loading," *Journal of Constructional Steel Research*, vol. 53, no. 3, pp. 283–305, 2000.
- [10] Federal Register, "Bridge safety standards," vol. 75, no. 135, 2010.
- [11] *SAP2000 Version 14.2.2*, Computers and Structures, Berkely, Calif, USA, 2010.

- [12] A. Daumueller and D. Jauregui, "Development of a structural health monitoring system for the assessment of critical transportation infrastructure," Tech. Rep. Sand2012-0886, Sandia National Laboratories, Department of Energy, February 2012.
- [13] BDI, *Structural Testing System II Operation Manual*, Bridge Diagnostics, Boulder, Colo, USA, 2005.
- [14] S. M. Dick, *Bending moment approximation for use in fatigue life evaluation of steel railway girder bridges [Ph.D. thesis]*, Department of Civil, Environmental and Architectural Engineering, University of Kansas, Lawrence, Kan, USA, 2002.
- [15] MotivePower, "MPX Commuter Locomotive," Locomotives, 2010, <http://www.motivepower-wabtec.com/locomotives/com-muter/mpxpress.php>.
- [16] A. Niesłony, "Determination of fragments of multiaxial service loading strongly influencing the fatigue of machine components," *Mechanical Systems and Signal Processing*, vol. 23, no. 8, pp. 2712–2721, 2009.
- [17] *MATLAB R2010b*, The MathWorks, Natick, Mass, USA, 2010.
- [18] A. Daumueller, *Strain-based evaluation of a riveted steel railroad bridge [Ph.D. dissertation]*, New Mexico State University, Las Cruces, NM, USA, 2012.

Research Article

Life-Cycle Management Strategy on Steel Girders in Bridges

Kevin K. L. So,¹ Moe M. S. Cheung,² and Eric X. Q. Zhang³

¹ Faculty of Science and Technology, The Technological and Higher Education Institute of Hong Kong, Tsing Yi Island, Hong Kong

² Department of Building Engineering, Tongji University, China

³ Department of Civil and Environmental Engineering, The Hong Kong University of Science and Technology, Clear Water Bay, Hong Kong

Correspondence should be addressed to Kevin K. L. So, kevin@ust.hk

Received 16 December 2011; Revised 22 May 2012; Accepted 23 May 2012

Academic Editor: Sami W. Tabsh

Copyright © 2012 Kevin K. L. So et al. This is an open access article distributed under the Creative Commons Attribution License, which permits unrestricted use, distribution, and reproduction in any medium, provided the original work is properly cited.

The major problems affecting the service life of bridges are related to various factors such as fatigue-sensitive details, increased service loads, corrosion deterioration, and the lack of proper maintenance. Among them, corrosion deterioration and fatigue damages of structures particularly to steel girder bridges are the most common ones. Bridges of different structural forms, at different locations or under different climates, may suffer from various degrees of deterioration. Steel girders at different positions of a bridge may also suffer from different degrees of damage. How to effectively maintain the bridge asset at a minimal cost and how to predict the time for future works are crucial, particularly when government funding sources become stretched. A comprehensive bridge management framework assisting stakeholders to appropriately and reasonably prioritize their future maintenance-related works in their bridge stocks, such that stakeholders can better allocate the limited resources, is utmost concerned. This paper proposes an integrated life-cycle management (LCM) strategy on steel girders in bridges in which corrosion deterioration and fatigue damage prediction models are mapped with girders' performance conditions. A practical example to demonstrate the applicability of the proposed LCM strategy is also illustrated.

1. Introduction

In recent decades, the long life of active use of transport infrastructure has become a worldwide issue. The developmental spending or investment for preparation of new infrastructures is becoming very difficult in all over the world particularly due to the poor economic condition. The life extension of the bridges not just makes the large economic profit, but also alleviates the financial burden on asset management, and effective decreases in the global warming and other environmental pollutions in life cycle of structure. Bridges are essential in transport infrastructure, and bridge maintenance or replacement is one of the largest expenditure items in the bridge life span.

In Japan, much infrastructure was constructed to support the spreading transportation network from 1950's to the 1970's. Recently, many infrastructures in Japan are getting old, and the numbers of bridges that have been in active service more than 50 years are increasing dramatically, and it is expected that these bridges will be more than 50,000

in 2021. From reasons, the inspection, maintenance, and rehabilitation planning are very important problem for long-lived active use of bridge and infrastructure [1]. In Australia, there are over 30,000 roads and rail bridges. For example, the Queensland government allocated \$350 million towards replacing approximately 100 old and obsolete road bridges in regional Queensland over the next five years, from 2006 to 2010 [2]. In USA, more than 43% of the bridges are made of steel. Currently, there are 190,000 steel bridges (simply supported and continuous) of which over 40,000 (25%) are structurally deficient and over 35,000 (18.5%) are functionally obsolete [3].

2. Steel Bridge Problems

The major problems affecting the service life of bridges are related to various factors such as fatigue-sensitive details, increased service loads, corrosion deterioration, and the lack of proper maintenance [4]. Among typical types of damage as shown in Figure 1, corrosion deterioration and fatigue

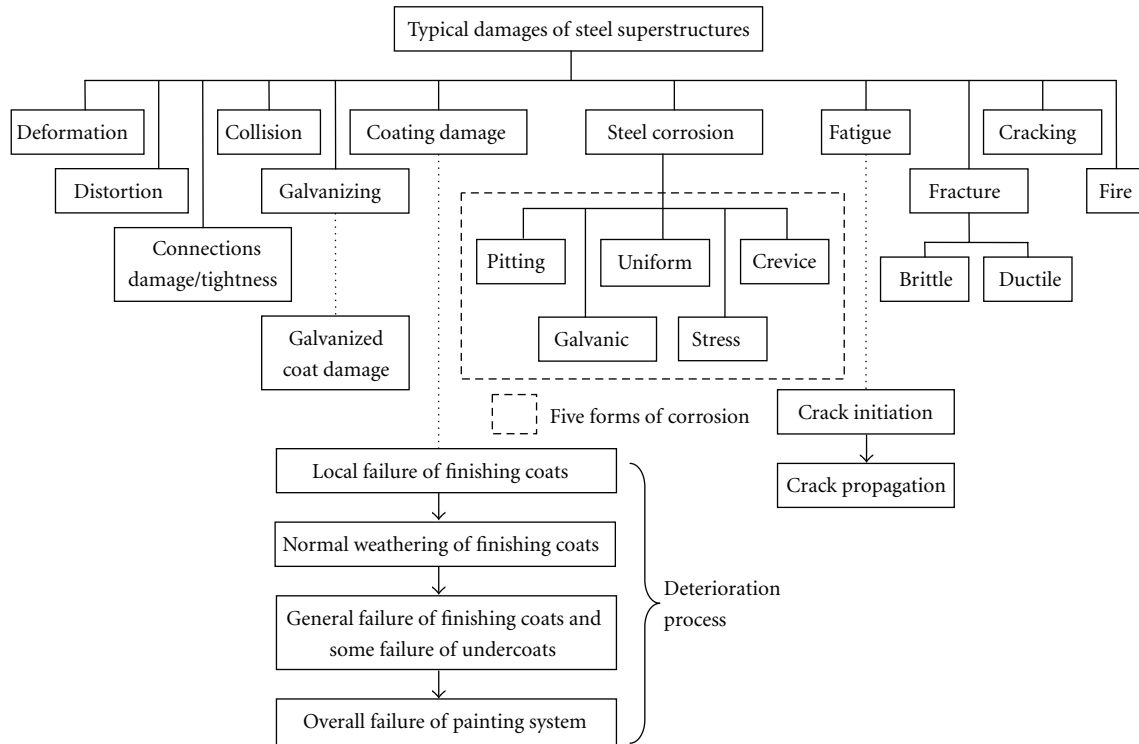


FIGURE 1: Typical types of damage of steel superstructures.

damages of structures particularly to steel girder bridges are the most common ones which are influenced by the environment and the vehicle loadings and its stress ranges.

In conventional practice, inspection, maintenance, or repair works are scheduled in accordance with the maintenance and rehabilitation manual and the maintenance authority would conduct scheduled works and record all the findings accordingly. However, the manual basically is a typical one rather than being specially made for a particular asset. Bridges of different structural forms, at different locations or under different climates, may suffer from various degrees of deterioration. Steel girders at different positions of a bridge may also suffer from different degrees of damage. How to effectively maintain the bridge asset at a minimal cost and how to predict the time for future works are important issues, when government funding sources become stretched.

To relieve the long-term financial burden on asset maintenance, whole life-cycle management (LCM) concept has been introduced in recent decade and is now getting more important in engineering design, construction, and management. In the whole LCM concept, the prediction of structural member deterioration is essential to plan for future maintenance actions. This paper proposes an integrated LCM strategy on steel girders in bridges in which corrosion deterioration and fatigue damage prediction models are mapped with girders' performance conditions. A practical example to demonstrate the applicability of the proposed strategy is also illustrated.

3. LCM in Steel Girder Bridge

This paper proposes an integrated LCM strategy considering three structural assessment factors altogether simultaneously: (1) the serviceability limit: deflection; (2) the ultimate limits: moment and shear, and (3) the fatigue strength limit. Clearly, the ultimate limits are not only two considerations, moment and shear. The bearing capacity can also be affected by corrosion. However, in common practice, if a steel bridge will not receive proper maintenance and painting, it will probably be constructed with bearing stiffeners to increase the bearing capacity. In order to reduce the complexity in showing the implementation of proposed integrated LCM strategy, the technical analysis of bearing behavior is not included in the paper. A steel girder bridge is provided as an example to demonstrate the use of the proposed strategy with corrosion deterioration and fatigue damage models being incorporated.

4. Corrosion Deterioration Model

Except for high-performance steel such as anticorrosion weathering steel, steel girder bridges are usually subject to corrosion to certain degrees. If undetected over a period of time, corrosion will weaken webs and flanges of steel girders by reducing the material thickness and possibly lead to dangerous structural failures [7].

In serviceability limit analysis, measurements of remaining thickness of corroded steel web and bottom flange are

TABLE 1: Statistical parameters for A and B [5, 6].

Parameters	Carbon steel		Weathering steel	
	A (μm)	B	A (μm)	B
(a) Rural environment				
Mean value, μ	34.0	0.65	33.3	0.498
Coefficient of variation, σ/μ	0.09	0.10	0.34	0.09
Coefficient of correlation, ρ_{AB}	—	—	-0.05	—
(b) Urban Environment				
Mean value, μ	80.2	0.593	50.7	0.567
Coefficient of variation, σ/μ	0.42	0.4	0.30	0.37
Coefficient of correlation, ρ_{AB}	0.68	—	0.19	—
(c) Marine Environment				
Mean value, μ	70.6	0.789	40.2	0.557
Coefficient of variation, σ/μ	0.66	0.49	0.22	0.10
Coefficient of correlation, ρ_{AB}	-0.31	—	-0.45	—

commonly considered. The effective thicknesses of webs and flanges are reduced with time as [7]:

$$t_f(t) = t_{f0} - C(t), \quad (1a)$$

$$t_w(t) = t_{w0} - 2C(t), \quad (1b)$$

where t_{f0} = the initial flange thickness (mm), t_{w0} = the initial web thickness (mm), $C(t)$ = the average corrosion penetration (mm) at time t .

Corrosion is influenced by the environment such as the amount of moisture in the air and the presence of salt. There is a common agreement that the corrosion time versus penetration rate can be modeled, with a good approximation, by an exponential function [8]:

$$C(t) = At^B, \quad (2)$$

where $C(t)$ = average corrosion penetration in micrometres (μm) after t years, t = time (years) of exposure, A = corrosion loss parameter after one year of exposure, and B = parameter determined from regression analysis of experimental data.

Parameters A and B were determined by Albrecht and Naeemi [5] and further verified by Kayser [6] as shown in Table 1.

Researchers have pursued extensive studies to predict time-variant corrosion propagation to capture the actual corrosion. However, these studies often neglect the influence of the periodic repainting effect on the corrosion process [3, 6, 8–10].

Lee et al. [7], based on previous studies, introduced a modified corrosion propagation model with periodic repainting as shown in (3). Lee's corrosion model is adopted for service life prediction of steel girders in this paper.

$$p_i(t) = \begin{cases} C(t - iT_{\text{REP}} - T_{\text{CI}})^m & \text{for } (i)T_{\text{REP}} + T_{\text{CI}} \leq t < (i+1)T_{\text{REP}} \\ p_{i-1}(iT_{\text{REP}}), & \text{otherwise,} \end{cases} \quad (3)$$

where $p_i(t)$ is corrosion propagation depth in micrometer (μm) at time t in years during i th repainting period; C is

random corrosion rate parameter; m is random time-order parameter; and T_{CI} , T_{REP} = random corrosion initiation and periodic repainting period (yrs), respectively.

5. Fatigue Damage Model

Several models have been developed to describe the process of fatigue damage, including the S-N model, the Miner's linear cumulative fatigue damage model, and the crack growth model under linear-elastic fracture mechanics (LEFM) approach [8]. S-N and Miner's models both have limitation in addressing the probabilistic nature, whereas LEFM approach based on crack propagation theory yields more accurate results for fatigue and fracture reliability assessment if the current crack size is measured [5]. Since the effect of crack size is taken into consideration, this approach yields more accurate results for fatigue and fracture reliability assessment if the current crack size can be measured [6]. In welded bridge details, the welding process inherently results in initial flaws from which crack growth may occur under cyclic loadings [9].

The commonly used crack growth model is the Paris-Erdogan model which is simplified to determine the required cycles for fatigue failure and this model is adopted for service life prediction in this paper. The number of cycle required to grow for fatigue crack can be estimated by taking integration from initial crack dimension a_0 to critical crack dimension a_c [11]. Zhao's model equation is shown in (4):

$$\int_{a_0}^{a_c} \frac{da}{[F(a)\sqrt{\pi a}]^m} = \int_{N_0}^{N_c} CS^m dN, \quad (4)$$

where $F(a) = F_e F_s F_w F_g$ is defined as the crack-size-dependent correction factor; F_e is crack the shape correction factor; F_s is the front free surface correction factor; F_w is the finite plate width correction factor; F_g is the stress gradient

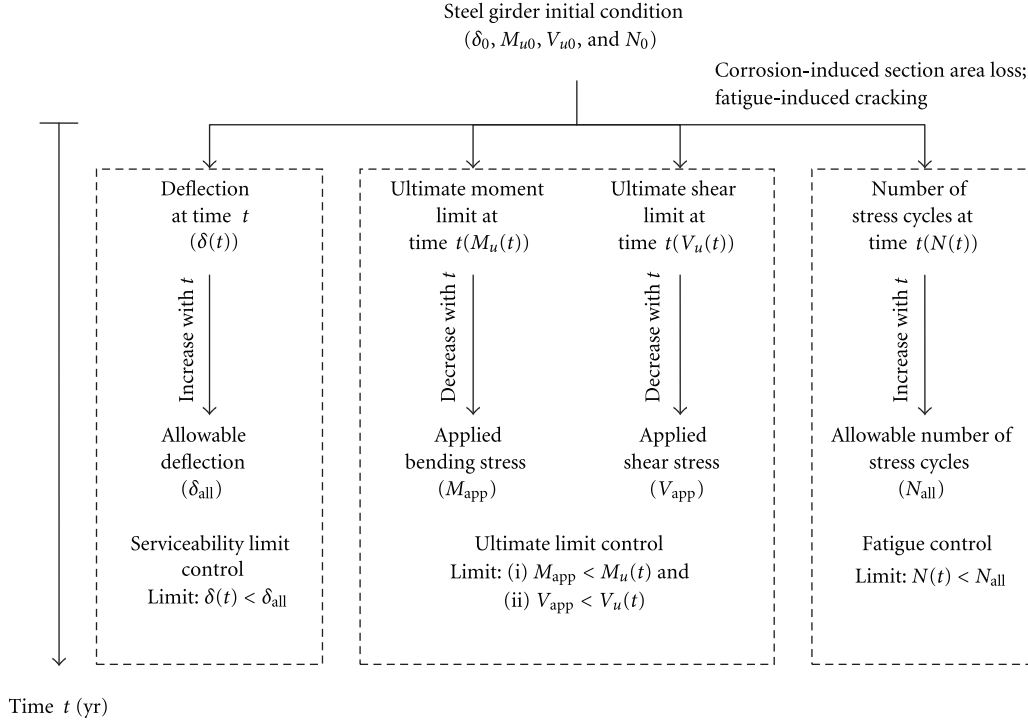


FIGURE 2: Integrated LCM strategy on steel bridge girders due to corrosion and fatigue.

correction factor; S is the stress range; C is the crack growth constant:

$$\int_{N_0}^{N_c} CS^m dN = C \sum_{i=1}^k S_i^m (N_{ic} - N_{i0})$$

$$\int_{N_0}^{N_c} CS^m dN = C \sum_{i=1}^k S_i^m (N_{ic} - N_{i0}) \quad (5)$$

$$= C S_{rMiner}^m N_T.$$

Since randomly variable loading was involved in every case of fatigue crack propagation, an effective stress intensity range was used based on Miner's rule and the corresponding Miner's effective stress. S_{rMiner} is the effective stress range while the N_T is the required number of cycles to cause fatigue failure. The crack growth component m equal to 3 has been observed to be applicable to basic crack growth rate data for structural steels as well as test data on welded members. The corresponding mean value of growth constant C was found to be 1.26×10^{-13} [11, 12]. Equation (4) can be further simplified to determine the required cycles for fatigue failure:

$$N_T = \int_{a_0}^{a_c} \frac{da}{1.26 \times 10^{-13} [F(a) S_{rMiner} \sqrt{\pi a}]^3}. \quad (6)$$

Having estimated the fatigue life in cycles, N_T , for the steel component, the data on average daily traffic specific to the bridge roadway, distribution of traffic volume per traffic lane, and expected traffic growth in future years are used to convert N_T in terms of time measures in years. If $t =$ fatigue life in years, then

$$N_T = (1 + r)^t \text{ADTT}(365) S_c, \quad (7)$$

where r is the yearly rate of traffic volume increase, ADTT is a random variable representing the average daily truck traffic and S_c is a random variable representing equivalent number of stress range cycles per truck crossing. The remaining fatigue life will be $t - t_0$, where t_0 is the current age of the steel component in years [13].

6. Integrated Life-Cycle Management Strategy

Corrosion deterioration and fatigue damages may weaken structural members and result in the increment of deflection, the reduction of ultimate bending, and shear strengths and the reduction of fatigue strength. The above corrosion and fatigue models with integration of predefined limits as below form service life prediction models to predict the service condition of steel members at any time throughout its life.

Conventional LCM is based on fixed predefined limit states either the serviceability limit (i.e., deflection) or the ultimate limits (i.e., moment and shear capacities) or the fatigue strength limit. However, it may not be always true that the one limit dominates over one another or vice versa in all circumstances. This paper proposes collective considerations of the serviceability limit: deflection, the ultimate limits: moment and shear, and the fatigue strength limit simultaneously which are essential in the further life-cycle cost (LCC) analysis. This proposed LCM strategy on steel girders covering serviceability limit, ultimate limits, and fatigue strength limit is graphically illustrated in Figure 2.

7. Definition of Limits

All structures have two basic requirements in common: safety from collapse and satisfactory performance of the structure for its intended use. The limit states usually define the various ways in which a structure fails to satisfy these basic requirements.

7.1. Serviceability Limit. Serviceability limit states usually relate to satisfactory performance and correspond to excessive deflection, vibration and local deformation. In this paper, the serviceability limit is defined in terms of deflection of a girder at any time, $\delta(t)$, in the design life. If the deflection exceeds the code requirement, δ_{all} , a serviceability failure is assumed to occur. It is also assumed that replacement or rehabilitation works must be conducted before girders reaching its deflection limit.

7.2. Ultimate Limits. Ultimate limit states usually relate to safety and correspond to strength, stability, and very large deformation. In the paper, the ultimate limits are governed by the structural capacity condition in bending, M , and shear, V , for any time in the life span. It is assumed that replacement or rehabilitation works must be conducted before the ultimate moment or shear capacity of the girder, $M_u(t)$ and $V_u(t)$, reaches the total applied moment or shear.

7.3. Fatigue Strength Limit. The fatigue strength limit suggested in this paper is defined in terms of accumulated numbers of stress cycles at any time, $N(t)$, throughout its life. If the number of stress cycles exceeds to its allowable, N_{all} , a fatigue failure is assumed to occur. Similarly, it is assumed that replacement or rehabilitation works must be conducted before reaching the limit.

7.4. Performance-Based Models. To mathematically present the condition of structural members towards its limits at particular time, buffer functions, $F(t)$, measured in percentage for each limit are then formulated accordingly as (8) to (11) where subscripts δ, M, V , and N for $F(t)$ refer to buffer functions for deflection, moment, shear and fatigue strength, respectively, and subscripts DL, SDL, LL, and I for M or V refer to moment or shear induced by dead load, superimposed dead load, live load, and impact load respectively:

$$F_{\delta}(t) = \frac{\delta_{all} - \delta(t)}{\delta_{all}}, \quad (8)$$

$$F_M(t) = \frac{M_u(t) - M_{DL} - M_{SDL} - M_{LL} - M_I}{M_u(t)}, \quad (9)$$

$$F_V(t) = \frac{V_u(t) - V_{DL} - V_{SDL} - V_{LL} - V_I}{V_u(t)}, \quad (10)$$

$$F_N(t) = \frac{N_{all} - N(t)}{N_{all}}. \quad (11)$$

8. Assignment of Condition States to the Steel Girder

In the proposed LCM strategy, four performance condition states, Good (G), Satisfactory (S), Fair (F), and Poor (P) are assigned to the percentage range of the deflection, the moment, the shear, and the fatigue strength buffer as mentioned above, respectively. Minimum acceptable criteria for Good (G_{min}), Satisfactory (S_{min}), and Fair (F_{min}) conditions are also needed to be defined.

$$\Omega_j = \begin{cases} G & F_{\delta}(t) \geq G_{min}, \\ S & S_{min} \leq F_{\delta}(t) < G_{min}, \\ F & F_{min} \leq F_{\delta}(t) < S_{min}, \\ P & F_{\delta}(t) < F_{min}. \end{cases} \quad (12)$$

Let Ω_j denote the set of possible limit states, then, $j = 1, 2, 3$, and 4 with respect to different limits: deflection, bending moment, shear, and fatigue accordingly. The general performance condition model as (12) is further modified as follows.

Serviceability Limit. For deflection:

$$\Omega_1 = \begin{cases} G & F_{\delta}(t) \geq 15\%, \\ S & 10\% \leq F_{\delta}(t) < 15\%, \\ F & 5\% \leq F_{\delta}(t) < 10\%, \\ P & F_{\delta}(t) < 5\%. \end{cases} \quad (13)$$

Ultimate Limits. For bending moment:

$$\Omega_2 = \begin{cases} G & F_M(t) \geq 40\%, \\ S & 30\% \leq F_M(t) < 40\%, \\ F & 20\% \leq F_M(t) < 30\%, \\ P & F_M(t) < 20\%, \end{cases} \quad (14)$$

for shear:

$$\Omega_3 = \begin{cases} G & F_V(t) \geq 40\%, \\ S & 30\% \leq F_V(t) < 40\%, \\ F & 20\% \leq F_V(t) < 30\%, \\ P & F_V(t) < 20\%. \end{cases} \quad (15)$$

Fatigue Strength Limit. For fatigue strength:

$$\Omega_4 = \begin{cases} G & F_N(t) \geq 40\%, \\ S & 30\% \leq F_N(t) < 40\%, \\ F & 20\% \leq F_N(t) < 30\%, \\ P & F_N(t) < 20\%. \end{cases} \quad (16)$$

The percentage ranges of buffers for different limit states are in fact various dependent on the stakeholders' decisions. Several factors, such as long-term costs, project risks, environmental policies, or local maintenance practices, may affect the decision of stakeholders. In this paper, for demonstration purpose, the percentage ranges of buffers are

assumed as shown in (13) to (16) and “F” condition state is also assumed as the minimum acceptable condition level. Once acceptable service condition states for each limit have been predefined, future replacement or rehabilitation works shall be carried out at the time before reaching its acceptable condition limits. The predicted action time will then be adopted in the life-cycle cost model for the subsequent cost-benefit analysis.

8.1. Options for LCM Strategy. In the proposed LCM strategy, the service life limits are generalized as three options.

Option 1: Serviceability Limits Control. Deflection:

$$t_{\text{lim}} = F_{\delta}(t) < 5\%. \quad (17)$$

Option 2: Ultimate Limits Control. Shear and moment capacities at time t :

$$t_{\text{lim}} = F_V(t) \text{ or } F_M(t) \leq 20\%. \quad (18)$$

Option 3: Fatigue strength Limit Control. Fatigue strength at time t :

$$t_{\text{lim}} = F_N(t) \leq 20\%. \quad (19)$$

9. Methodology of the Integrated Life-Cycle Cost (LCC) Model

LCC model is commonly used as the basis to evaluate the cost effectiveness of different management strategies. In the model, proper actions taken at appropriate time are a crucial element for the model accuracy. The LCC of a structure is a combination of the present values of all future costs of occurring within the life span of the structure. The minimum expected LCC denoted as LCC_{ET} has been the most widely used criterion in design optimization of new structural systems considering lifetime performance. The mathematical presentation of the expected LCC of a structure over T years of life span can be generalized as:

$$LCC_{\text{ET}} = \sum_{i=1}^n \sum_{t=0}^T \left(\beta_i(t) \frac{C_i(t)}{(1+r)^t} \right), \quad (20)$$

where LCC_{ET} is expected total life-cycle cost, $C_i(t)$ is cost of future action i at time t , β_i is probability of occurrence of future action i , r is a discount rate (constant discount rate assumed in the paper), i is type of future actions, t is time in year, and T is service life span in years. The cost of future actions can be further subdivided into expected design cost $C_{\text{des}}(t)$, expected construction cost $C_{\text{con}}(t)$, expected inspection cost $C_{\text{ins}}(t)$, expected maintenance cost $C_m(t)$, expected replacement and rehabilitation cost $C_{\text{rep}}(t)$, expected demolition cost $C_{\text{dem}}(t)$, and expected failure cost $C_{\text{fail}}(t)$, respectively. To assist better understanding of possible strategies-induced costs, the scopes of inspection, maintenance, and replacement and rehabilitation works are defined and elaborated.

10. Inspection, Maintenance, and Replacement and Rehabilitation Strategies

10.1. Inspection Strategy. Inspection strategies vary, depending on the policy of the stakeholders. Frequent inspections provide more updated information for future maintenance plans. However, the LCC of inspection work is usually insignificant in comparison to the whole LCC of the structure, and a cost-effective management approach should be maintained [17]. The cost of inspection work (C_{ins}) is generally categorized into two kinds with defined scopes as follows.

(1) General Inspection ($C_{\text{ins},1}$) A visual inspection can be conducted annually for obvious defects which might lead to safety problems or lead to loss of use of the structure or restriction of use [17]. Visual inspections allow discovering the rusting or loss of material sections. Steel members should be examined regarding (i) the condition of its protective system including protective painting or galvanizing; (ii) the condition of materials towards corrosion; (iii) the condition of connections; (iv) cracking or fracture defects; and (v) structural deformation or distortion.

(2) Detailed Inspection ($C_{\text{ins},2}$) Inspection work includes visual examination of all visible and accessible parts of a structure. Some minor nondestructive inspection (NDI) of representative areas would be carried out. NDI methods commonly include radiography and ultrasonics for the determination of internal defects while dye penetration and magnetic particle inspection for the detection of surface defects. The purpose of detailed inspection is to verify the deterioration state of the structure, if it is on the schedule R&R plan. Thus, the detailed inspection time is adjusted based on simulated R&R time. It is assumed that detailed inspection works shall be conducted before replacement or rehabilitation works taken place [18].

10.2. Maintenance Strategy. Maintenance of protective coatings is important for visual and physical preservation of steel components. A durable paint combination with long maintenance intervals is not only an economical but also an environmentally acceptable solution [18]. Typically, there are three types of coatings for corrosion rate reduction which are paints, steel galvanizing, and oxidized steel formed on weathering steel of a combination of these coatings. Because of the difficulty in galvanizing large sections of steel elements, the industry has generally used paints for protection. Paints or high-performance coatings, as some of the newer systems are known, are separated into three categories: the inhibitive primer, the sacrificial primer, and the barrier coat [19]. Once defects on coating surface have been found, proper cleaning on the surface and subsequent repainting works should be taken place.

10.3. Replacement and Rehabilitation (R&R) Strategy. Repairing process of steel structural elements usually in many cases is very complex and it requires the use of advanced material solution and techniques. The most important damage to the steel bridge elements can be classified into

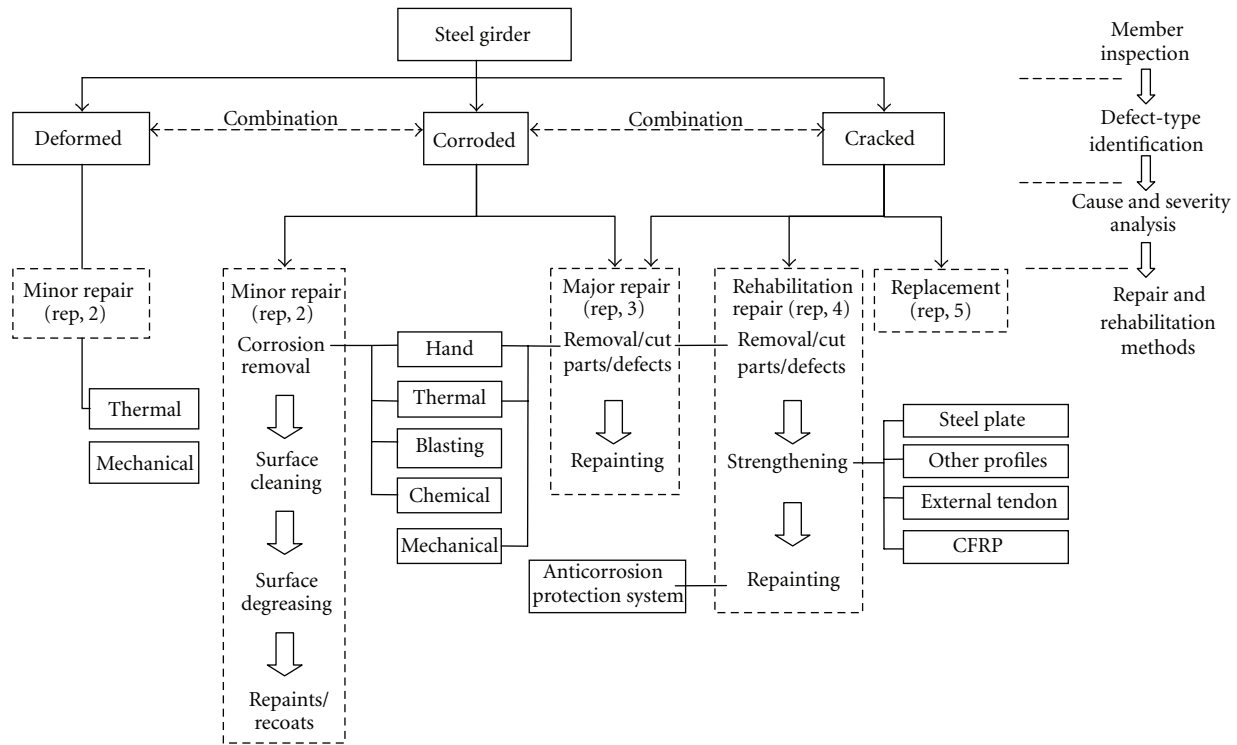


FIGURE 3: Replacement and rehabilitation methods for conventional steel girder.

TABLE 2: Proposed replacement and rehabilitation action set.

Action description	Action matrix	Possible replacement and rehabilitation methods
Do nothing	Rep, 1	Observation
Minor repair	Rep, 2	Corrosion removal, surface cleaning, degreasing, and repainting Rectify deformed parts
Major repair	Rep, 3	Removal/cut defects and parts and repainting Removal/cut defects and parts, strengthening, and repainting
Rehabilitation repair	Rep, 4	Structure strengthening by steel plate Structure strengthening by CFRP Structure strengthening by external tendons
Replacement	Rep, 5	Structure replaced by new members

three groups: (i) corrosion destruction of the members and/or their joints; (ii) fatigue effects in steel and its brittle fracture; (iii) mechanical fracture, including collision, of the elements themselves and/or the joints.

Before carrying out any rehabilitation works, the cause of defects and the severity of such defects towards the main structural system should be identified and subsequently analyzed. Depending on the severity and the type of damage causes, different rehabilitation techniques can be applied. General classification of the typical R&R methods for steel girder is proposed and illustrated in Figure 3. Any R&R work should be considered individually and it should be preceded by evaluation and assessment of the condition of the structure, the relevant theoretical analysis as well as the selection of an appropriate repair technology [20].

Regarding the degree of R&R works, it may be classified into five different actions as shown in Table 2 and defined with specified meanings and scopes.

- (1) Do nothing (Rep, 1): it means no action is carried out and there is no change in the condition of the structure.
- (2) Minor repair (Rep, 2): it provides no improvement in durability performance but slows the deterioration rate such that the condition of the structure or its components could be maintained for a certain further period.
- (3) Major repair (Rep, 3): it provides no improvement in durability performance but restores the durability, structural strength, and function or appearance of the

TABLE 3: Moments and shears due to dead and superimposed dead loads (M_{DL} , M_{SDL} , V_{DL} , and V_{SDL}).

Girder nos.	Position	Due to dead load		Due to superimposed dead	
		Mean M_{DL} (kNm)	Mean V_{DL} (kN)	Mean M_{SDL} (kNm)	Mean V_{SDL} (kN)
1 and 5	Mid span	1,185.30	—	612.20	—
	End of cover plate	314.47	—	162.42	—
	Support	—	169.33	—	87.46
2, 3, and 4	Mid span	1,185.30	—	214.67	—
	End of cover plate	314.47	—	56.95	—
	Support	—	169.33	—	30.67

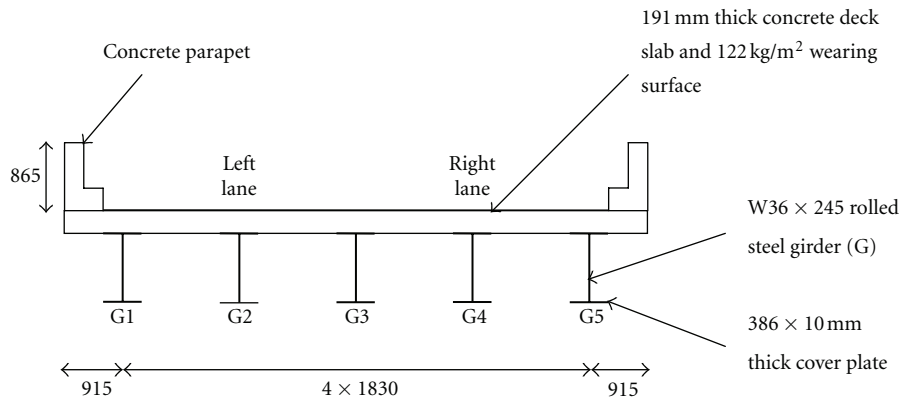


FIGURE 4: Typical cross section of two-lane rolled steel girder bridge (unit: mm).

structure. The condition of the structure or its components is improved. However, similar damage may reoccur during the remaining life of the structure such that subsequent repair work is expected. The condition of the structure will be reset to the initial condition after major repair work.

- (4) Rehabilitation repair (Rep, 4): it restores the durability, structural strength, and function or appearance of the structure and improves the durability performance of the repaired structure or its components. Similar damage may occur later with lower probability. The condition of the structure will be reset to the initial condition after the work.
- (5) Replacement (Rep, 5): it refers to the replacement of existing members, which may improve local capacity, durability of the structure, and so forth. The condition of the structure will be reset to the initial condition after the work.

11. Example of LCM Strategy of Steel Girders in Bridges

A simply supported composite steel girder bridge with rolled-beam stringers is adopted as an example to illustrate the proposed LCM strategy. The bridge has a simple span of 28.0 m with two-lane traffic in the same direction. 191 mm thick concrete deck slab with wearing surface at weight 122 kg/m² is supported by five rolled steel girders at size W36 × 245. Each girder has a welded cover-plate with size 386 ×

10 mm thick under bottom flange. 865 mm high of concrete parapets are installed at both sides. The distance from each end of the cover plate to the adjacent bearing is 2.0 m. The cross section of the bridge is shown in Figure 4.

11.1. Loading Analysis

11.1.1. Dead and Superimposed Dead. It is assumed the dead and superimposed dead loads are normally distributed with coefficient of variation (C.O.V.) 0.1 [9, 10, 21]. The induced mean moments at the mid span and the end of cover plate and the induced mean shears at end supports are calculated and summarized in Table 3.

From Table 3, the maximum bending moment at mid span is 1,798 kNm, the bending moment at the ends of cover plates is 476.89 kNm, and the maximum shear load at supports is 257 kN for Girder Nos. 1 and 5. Whereas, for Girder Nos. 2, 3, and 4, the maximum bending at mid span is 1,400 kNm, the bending moment at ends of cover plates is 372 kNm, and the maximum shear load at supports is 200 kN.

11.1.2. Live and Impact. The live load on the bridge is assumed due to traffic only. Girders moments and shears summarized in Table 4 are calculated based on the survey results of Nowak [21] with literature references in which the average daily truck traffic (ADTT) is 5,000 with 66% of the cases that a truck was in the left lane, 33% of the cases that a truck was in the right lane, and 1% of the cases that trucks

TABLE 4: Moments and shears due to live load (M_{LL} and V_{LL}).

Girder no.	Position	Left lane			Right lane			Both lanes		
		Mean M_{LL} (kNm)	Mean V_{LL} (kN)	C.O.V. ⁽¹⁾	Mean M_{LL} (kNm)	Mean V_{LL} (kN)	C.O.V. ⁽¹⁾	Mean M_{LL} (kNm)	Mean V_{LL} (kN)	C.O.V. ⁽¹⁾
1	Mid span	2,333.46	—	—	567.56	—	—	2,720.61	—	—
1	End of cover plate	815.24	—	0.24	198.29	—	0.33	950.50	—	0.23
1	Support	—	333.35	—	—	81.08	—	—	388.66	—
2	Mid span	2,390.08	—	—	998.17	—	—	3,247.35	—	—
2	End of cover plate	835.02	—	0.18	348.73	—	0.23	1,134.52	—	0.18
2	Support	—	341.44	—	—	142.6	—	—	463.91	—
3	Mid span	1,786.97	—	—	1,735.61	—	—	3,356.65	—	—
3	End of cover plate	624.31	—	0.19	606.37	—	0.19	1,172.71	—	0.19
3	Support	—	255.28	—	—	247.94	—	—	479.52	—
4	Mid span	1,107.47	—	—	2,413.79	—	—	3,356.65	—	—
4	End of cover plate	386.92	—	0.23	843.30	—	0.18	1,172.71	—	0.19
4	Support	—	158.21	—	—	344.84	—	—	479.52	—
5	Mid span	654.47	—	—	2,440.12	—	—	2,920.77	—	—
5	End of cover plate	228.65	—	0.27	852.50	—	0.22	1,020.43	—	0.21
5	Support	—	93.50	—	—	348.59	—	—	417.25	—

⁽¹⁾C.O.V.: coefficient of variation.

TABLE 5: Statistical parameters of random variables for the illustrative example.

Parameters	Materials	Variables	Mean (μ)	C.O.V. ⁽¹⁾ (σ/μ)	Distribution	Sources
Corrosion deterioration rate	Carbon steel	A	70.6 μm	0.66	LN ⁽²⁾	[5, 6]
		B	0.789	0.49		
		ρ_{AB}	-0.31	—		
Corrosion Initiation	Weathering steel	A	40.2 μm	0.22	LN	[7]
		B	0.557	0.10		
		ρ_{AB}	-0.45	—		
Repaint duration	—	T_{CI}	15 yr	0.30	LN	[7]
Repaint duration	—	T_{REP}	20 yr	0.25		
Initial crack dimension	Structural steel	a_0	0.762 mm	0.5	LN	[14]
Crack growth constant		C	1.26×10^{-13}	0.63		
Crack growth exponent		m	3	—	Constant	[15]
Critical crack dimension		a_c	0.0254 m			
Fracture toughness		K_{IC}	43.97 MPa m ^{0.5}	0.19		
Compressive strength	Concrete	f_c	21 MPa ⁽⁴⁾	0.19	LN	[9]
Yield stress	Steel	F_y	248 MPa	0.10		
Modulus of elasticity	Concrete	E_c	30,000 MPa	0.20	LN	[16]
	Steel	E_s	210,000 MPa	0.06		
Deck slab thickness	Concrete	t_c	191 mm	0.20	N ⁽⁴⁾	[14]

⁽¹⁾C.O.V.: coefficient of variation.

⁽²⁾LN: lognormal distribution.

⁽³⁾TN: truncated normal distribution.

⁽⁴⁾N: normal distribution.

TABLE 6: Deflection of steel girder bridge with cover plate.

Years	Nominal corrosion penetration (mm)			Nominal maximum deflection (mm)		
	Carbon steel without coat	Carbon steel with coat	Weathering Steel	Carbon steel without coat	Carbon steel with coat	Weathering steel
0	0.000	0.000	0.000	29.332	29.332	29.332
10	0.434	0.000	0.145	29.554	29.332	29.405
20	0.750	0.251	0.213	29.719	29.460	29.440
30	1.033	0.251	0.267	29.870	29.460	29.468
40	1.297	0.503	0.314	30.012	29.589	29.492
50	1.546	0.503	0.355	30.149	29.589	29.513
60	1.786	0.754	0.393	30.282	29.721	29.533
70	2.016	0.754	0.428	30.413	29.721	29.551
75	2.129	0.754	0.462	30.478	29.721	29.560

were in both lanes [9, 10, 14]. It is also assumed that the live load from vehicles is kept unchanged throughout the bridge's service life. To account for the dynamic effects of a vehicle riding over the bridge, an impact factor is adopted as a multiplier. The impact fraction of live load according to ASSHTO Specification (2004) [22] is 0.231. The moment and the shear due to impact will then be added on the live load schedule.

11.2. Service Life Prediction

11.2.1. Serviceability Limit: Deflection. Corrosion reduces the effective cross-section and occurs mainly at the web and the top of bottom flange of steel girders. Reduction

of section area leads to weaken the flexural strength and the shear strength and increases the deflection of bridge deck under service loadings. According to the ASSHTO specification, the deflection limit due to live load plus impact is $\text{span}/800 = 35$ mm for typical highway bridges. In order to investigate the long-term effectiveness of different preventive measures of steel girders, three scenarios include carbon steel without protective paint, carbon steel with protective paint, and weathering steel are compared. The steel bridge is modeled against corrosion in marine environment based on the statistical parameters listed in Table 5. The nominal maximum deflections under three different scenarios are calculated according to (1) to (3) and summarized in Table 6.

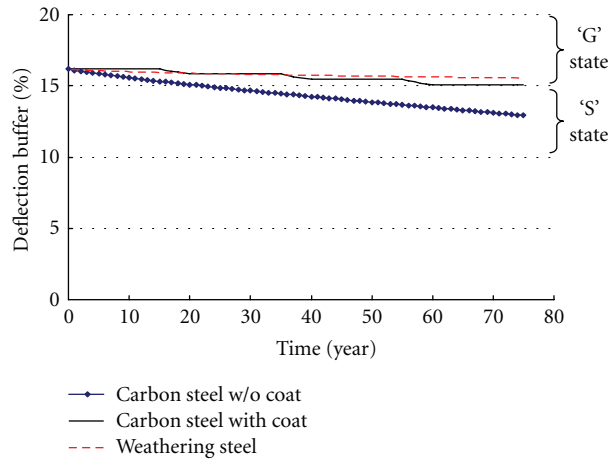


FIGURE 5: Deflection Buffer Over Life Span.

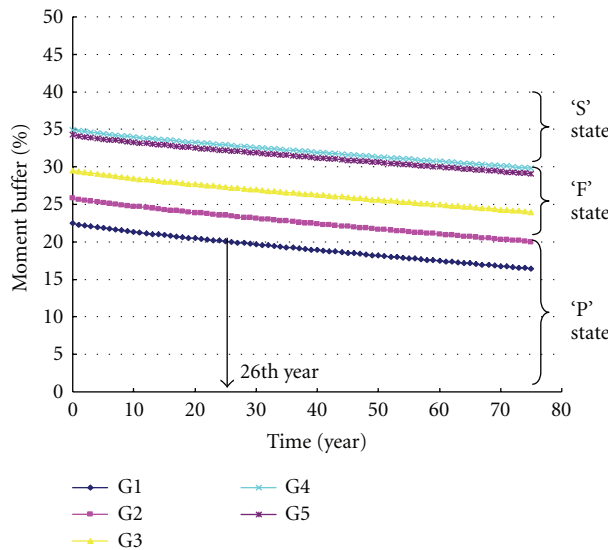


FIGURE 6: Moment buffer over life span of carbon steel girders.

The deflection buffer against time over the life span is plotted in Figure 5. Results show that the deflection for girders without any protective systems is the highest one while the deflection for girders made of weathering steel is the lowest. According to the proposed management strategy, throughout the 75 years service life, none of steel girder types falls below the fair condition state (i.e., “F”—State) in the Deflection Condition State Set (i.e., (13)). In other words, no R&R works for deflection is expected throughout the life span.

11.2.2. Ultimate Limits—Moment and Shear. It is assumed that R&R actions only be taken places when condition reaches “P” state range in accordance with (14) and (15). Simulated time to reach “P” state in terms of moment and shear buffer limits at 80 percentile value are plotted in Figures 6 and 7 respectively. Concerning the moment condition, result shows that Girder No. 1 will reach the moment buffer

limit in the 26th year and the other girders will remain “F” state and “S” state throughout the life span. As to the shear condition, results demonstrate all girders will remain “G” state that means shear stress causes insignificant impact to girders.

11.2.3. Fatigue Damage Limit. The maximum live load model developed above is insufficient to determine the effective range of the stress intensity factors. For fatigue analysis, the loading effects are modeled by the fatigue truck provided in the American Association of State Highway and Transportation Officials (AASHTO) specification with gross weight 240 kN. Each truck passage is assumed to cause one stress cycle only. Under repeated tensile stresses, fatigue cracks may form at the end weld of the cover plate and penetrate into the bottom flange. Under given bending moment in a girder, the critical fatigue stress is located in the bottom flange at the end of cover plate such that it should

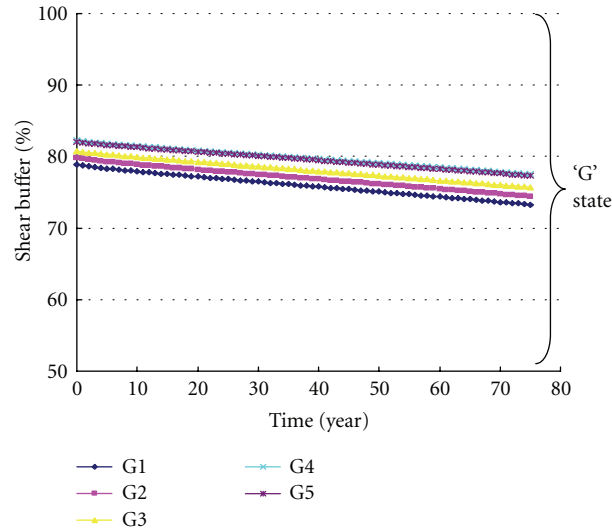


FIGURE 7: Shear buffer over life span of carbon steel girders.

TABLE 7: Time (year) to “P” state of fatigue buffers.

Girder no.	Time
G1	48
G2	43
G3	47
G4	50
G5	62

be calculated based on the cross section of the girder without cover plate. The service life of each girder is simulated based on the statistical parameters in Table 5 and the simulated time for each girder to reach its “P” state is summarized in Table 7.

Results show that girder no. 2 is the most sensitive girder to the fatigue damage, and it will reach the fatigue limit in the 43rd year.

12. Discussion

There are two important messages incurred from the example: (1) fatigue damages may not always dominate. Conventional LCM is in accordance with fixed predefined limit states either the serviceability limit or the ultimate limits or the fatigue limit. However, it may not be always valid that one limit dominates over one another or vice versa under all situations. Results demonstrate that the earliest simulated replacement or rehabilitation time for girders under bending stress is in the 26th year while the earliest simulated repair time for girders under fatigue damages is in the 43th year and (2) service lives of each girders are various. Conventional management approach treats all girders on equal ground. However, some girders may deteriorate faster than expected and some may not. In the case of fatigue damages, girder no. 5 has the longest life while girder no. 2 has the shortest

one. Concerning the bending failure, the most critical one is girder no.1 while the least are girder nos. 4 and 5.

Service life prediction models integrated into the management strategy could provide a better picture for the stakeholders to identify the sensitive steel girder under corrosion deterioration or fatigue damages. Other factors affecting the condition of steel girders are neglected in the paper. However, steel components damages are definitely not conclusive to these two types.

Moreover, proposed acceptable limits can be further tied into reliability index if sufficient statistical information of the parameters in deterioration models is available. The rehabilitation time can be determined by the predefined reliability index value. Even though the reliability assessment has not been incorporated in this paper, the proposed LCM concept is not affected.

Furthermore, owing to the lack of sufficient cost data, the paper only addresses the LCM strategy and the methodology of service life prediction models being integrated into the LCC model. If sufficient financial data is available, it could provide further decision making information for selecting the most appropriate management strategy by LCC comparison.

13. Further Research Approach

Further research approach on the proposed flow for LCM strategy on steel girder in bridges as shown in Figure 8 can be conducted to test and verify its practicability. The proposed verification approach is categorized into 7 stages from Design Stage to Analysis Stage. However, some key important data should be obtained in the investigation stage prior to the LCC analysis process.

(1) *Cost Data.* Collection of possible future cost data is necessary to provide further decision making information for selecting the most appropriate management strategy.

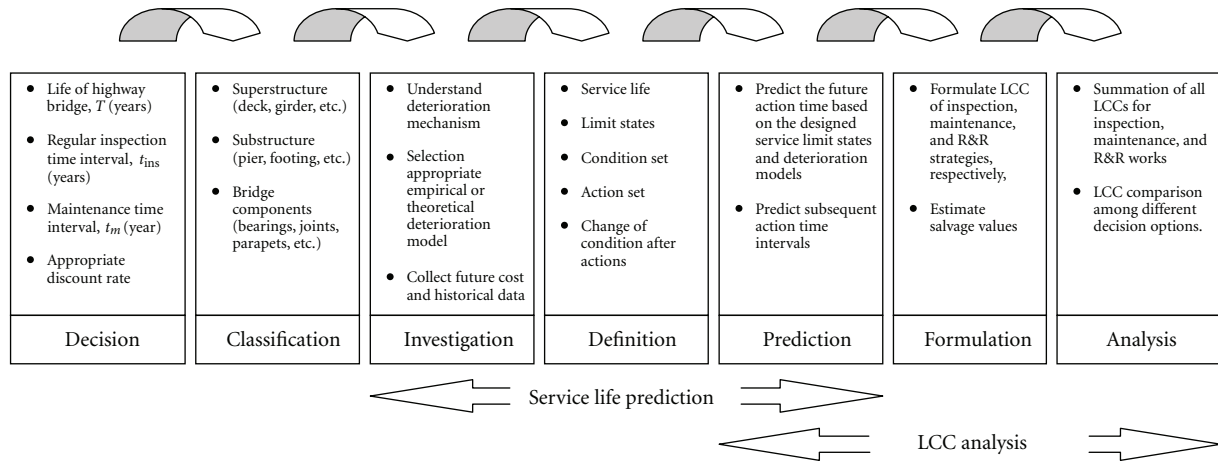


FIGURE 8: Suggested LCM flows for inspection, maintenance, and replacement and rehabilitation Works.

The cost of different types of future work should comprise inspection, operation, maintenance, management, repair, rehabilitation, replacement, demolition and failure.

(2) *Historical Data.* Collection of historical repair or rehabilitation data can be used to estimate the probability of any occurrence in case the future action time could not be predicted by appropriate deterioration models.

(3) *Deterioration Mechanism.* Steel component damage is definitely not exclusive to corrosion deterioration and fatigue damage. In the study, other factors affecting the condition of the steel girders are neglected. In fact, the bearing capacity of the steel girders and deterioration of other bridge components such as bridge bearings, expansion joints, and profile barriers could be incorporated into the LCM strategy. The proposed LCM strategy can be further enlarged.

14. Conclusion

Technical review on structural steel corrosion and fatigue models is addressed in this paper. However, in order to properly develop a LCM strategy for steel bridges in particular regions, it is necessary to consider some adjustments of parameters on the service life prediction models to suit the regional characteristics and needs. Further investigations on different empirical models under Hong Kong environments will be undertaken to identify the most appropriate empirical models for service life prediction purpose.

This paper proposes an integrated LCM framework assisting stakeholders to appropriately and reasonably prioritize their future maintenance-related works on steel girders in their bridge stocks such that stakeholders can better allocate the limited resources. In the framework, corrosion deterioration and fatigue damage prediction models are mapped with girders' performance conditions on deflection, ultimate moment and shear capacities, and fatigue strength limit simultaneously. The illustrative example on

the proposed strategy on steel girders is also provided to demonstrate its applicability.

Acknowledgment

The work was financially supported by the Research Grants Council of the Hong Kong Special Administrative Region, China under Grant no. 610505.

References

- [1] T. Obata, A. Nakajima, and K. Maeda, "Study on application of reliability analysis for bridge management system on steel bridge structures," in *Life-Cycle Cost and Performance of Civil Infrastructure Systems*, H.-N. Cho, D. M. Frangopol, and A. H.-S. Ang, Eds., p. 291, Taylors & Francis Group, London, UK, 2007.
- [2] Queensland, "Another \$2 billion for Queensland infrastructure," *Engineers Australia*, vol. 77, no. 11, 25 pages, 2005.
- [3] A. A. Czarnecki and A. S. Nowak, "Time-variant reliability profiles for steel girder bridges," *Structural Safety*, vol. 30, no. 1, pp. 49–64, 2008.
- [4] M. Tavakkolizadeh and H. Saadatmanesh, "Fatigue strength of steel girders strengthened with carbon fiber reinforced polymer patch," *Journal of Structural Engineering*, vol. 129, no. 2, pp. 186–196, 2003.
- [5] P. Albrecht and A. H. Naeemi, "Performance of weathering steel in bridges," *National Cooperative Highway Research Program Report*, 1984.
- [6] J. R. Kayser, *The effects of corrosion on the reliability of steel girder bridges [Ph.D. thesis]*, University of Michigan, Ann Arbor, Mich, USA, 1988.
- [7] K. M. Lee, H. N. Cho, and C. J. Cha, "Life-cycle cost-effective optimum design of steel bridges considering environmental stressors," *Engineering Structures*, vol. 28, no. 9, pp. 1252–1265, 2006.
- [8] M. S. Cheung and W. C. Li, "Serviceability reliability of corroded steel bridges," *Canadian Journal of Civil Engineering*, vol. 28, no. 3, pp. 419–424, 2001.
- [9] A. M. Sommer, A. S. Nowak, and P. Thoft-Christensen, "Probability-based bridge inspection strategy," *Journal of Structural Engineering*, vol. 119, no. 12, pp. 3520–3536, 1993.

- [10] M. Jiang, R. B. Corotis, and J. Hugh Ellis, "Optimal life-cycle costing with partial observability," *Journal of Infrastructure Systems*, vol. 6, no. 2, pp. 56–66, 2000.
- [11] Z. Zhao, A. Haldar, and F. L. Breen Jr., "Fatigue-reliability evaluation of steel bridges," *Journal of Structural Engineering*, vol. 120, no. 5, pp. 1608–1623, 1994.
- [12] C. MacDougall, M. F. Green, and S. Shillinglaw, "Fatigue damage of steel bridges due to dynamic vehicle loads," *Journal of Bridge Engineering*, vol. 11, no. 3, pp. 320–328, 2006.
- [13] J. Mohammadi, S. A. Guralnick, and R. Polepeddi, "Bridge fatigue life estimation from field data," *Practice Periodical on Structural Design and Construction*, vol. 3, no. 3, pp. 128–133, 1998.
- [14] M. S. Cheung and W. C. Li, "Probabilistic fatigue and fracture analyses of steel bridges," *Structural Safety*, vol. 25, no. 3, pp. 245–262, 2003.
- [15] J. W. FISHER, *Fatigue and Fracture in Steel Bridges, Case Studies*, John Wiley & Sons, New York, NY, USA, 1984.
- [16] M. S. Cheung and W. C. Li, "Serviceability reliability of corroded steel bridges," *Canadian Journal of Civil Engineering*, vol. 28, no. 3, pp. 419–424, 2001.
- [17] K. K. L. So, M. M. S. Cheung, and E. X. Q. Zhang, "Life-cycle cost management of concrete bridges," *Proceedings of the Institution of Civil Engineers: Bridge Engineering*, vol. 162, no. 3, pp. 103–117, 2009.
- [18] A. Saloranta, "High performance coatings for steel bridges," *Progress in Organic Coatings*, vol. 22, no. 1–4, pp. 345–355, 1993.
- [19] C. K. Tam and S. F. Stiemer, "Development of bridge corrosion cost model for coating maintenance," *Journal of Performance of Constructed Facilities*, vol. 10, no. 2, pp. 47–56, 1996.
- [20] W. Radomski, *Bridge Rehabilitation*, Impress College Press, 2002.
- [21] A. S. NOWAK, "Calibration of LRFD bridge design code," Final Report prepared for NCHRP, TRB, National Research Council, Department of Civil Engineering, University of Michigan, Ann Arbor, Mich, USA, 1993.
- [22] ASSHTO LRFD Bridge Design Specifications, American Association of State Highway and Transportation Officials, Washington, DC, USA, 2004.

Research Article

Optimization of Post-Tensioned Box Girder Bridges with Special Reference to Use of High-Strength Concrete Using AASHTO LRFD Method

Byungik Chang,¹ Kamal Mirtalaei,² Seungyeol Lee,³ and Kenneth Leitch¹

¹ Department of Engineering and Computer Science, West Texas A&M University, WTAMU Box 60767, Canyon, TX 79016, USA

² Engineering Technical Group, Arizona Department of Transportation, 205 South 17th Avenue, MD 618E, Phoenix, AZ 85007, USA

³ Design Section, Nfra Inc., 77 E. Thomas Road, Suite 200, Phoenix, AZ 85012, USA

Correspondence should be addressed to Byungik Chang, bchang@wtamu.edu

Received 9 January 2012; Revised 17 May 2012; Accepted 24 May 2012

Academic Editor: Sami W. Tabsh

Copyright © 2012 Byungik Chang et al. This is an open access article distributed under the Creative Commons Attribution License, which permits unrestricted use, distribution, and reproduction in any medium, provided the original work is properly cited.

With the Federal Highway Administration-mandated implementation of the LRFD specifications, many state departments of transportation (DOTs) have already started implementing LRFD specifications as developed by the AASHTO. Many aspects of the LRFD specifications are being investigated by DOTs and researchers in order for seamless implementation for design and analysis purposes. This paper presents the investigation on several design aspects of post-tensioned box girder bridges designed by LRFD Specifications using conventional or High-Strength Concrete (HSC). A computer spreadsheet application was specifically developed for this investigation. It is capable of analysis, design, and cost evaluation of the superstructure for a cast-in-place post-tensioned box girder bridge. Optimal design of a post-tensioned box girder is achievable by correct selection of design variables. Cost evaluation of superstructures with different geometrical and material configurations has led to the development of optimum design charts for these types of superstructures. Variables used to develop these charts include, among others, span length, section depth, web spacing, tendon profile, and concrete strength. It was observed that HSC enables the achievement of significantly longer span lengths and/or longer web spacing that is not achievable when using normal strength concrete.

1. Introduction

American Association of State Highway and Transportation Officials (AASHTO) standard specification [1] has been the main bridge design specification in the United States since the 1940s. During the last two decades, there have been significant developments in concrete bridge design methods and utilization of new concrete materials. The implementation of load and resistance factor design (LRFD) and the use of High Strength/High Performance Concrete (HSC/HPC) are important subjects of investigation. The state DOTs have increased the use of HPC/HSC concrete and implementation of the AASHTO LRFD specification [2]. LRFD is based on the latest developments in structural analysis and materials to assure desired serviceability and ultimate behavior, safety, aesthetics, and economy. It benefits the valuable experiences of AASHTO allowable stress design (ASD) and load factor

design (LFD) methods, which have been in use since the 1940s and comprise the Standard specification.

This new specification resulted in design procedures significantly different compared to the earlier methods. The new LRFD specification is based on a probability-based approach in which load and resistance factors are based on a specific level of structural failure [3]. The changes in the new LRFD design methods are significant and challenge the bridge engineers working with standard specification for so many years.

In the present work, a detailed investigation was performed on different aspects of cast-in-place (CIP) post-tensioned box girder bridges. These include a general comparison of the two design specifications, utilization of post-tensioned high-strength concrete and cost based design optimization of the prestressed box girder bridges. A comprehensive spreadsheet was developed which enables

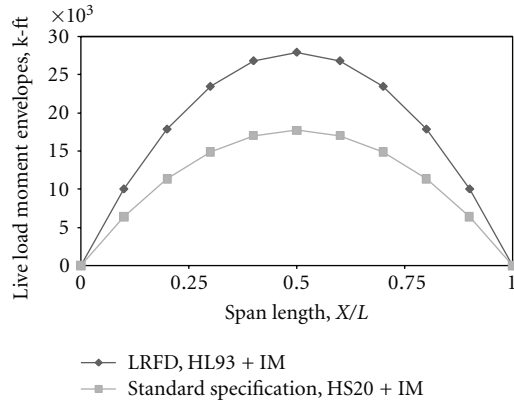


FIGURE 1: Comparison of moment envelopes due to only distributed live load plus impact for 180 ft single-span box girder with eight webs spaced at 9 ft.

the user to input almost every necessary design parameter and perform the analysis, design, and cost estimate of a post-tensioned box girder bridge superstructure according to both AASHTO standard and LRFD specifications. A copy of the program is obtainable by contacting the authors.

2. Design Comparison

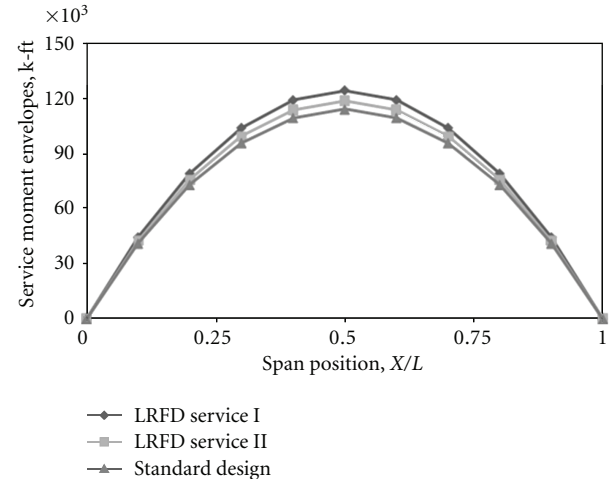
Different design parameters were studied for the comparison of the newer LRFD and the older standard AASHTO specifications. These include live load bending moment and shear force envelopes, service and factored bending and shear envelopes, bending capacity, moment and shear distribution factors, prestressing losses, designed number of prestressing strands, and superstructure cost.

2.1. Live Load and Load Combinations for Moments. LRFD HL-93 live load is by itself significantly heavier than the standard HS-20 loading, but this difference will partly offset by the introduction of completely new live load distribution methods, service, and ultimate load factors. Figure 1 shows live load bending moment envelopes for HL-93 and HS20 (live load plus impact effects) which was calculated based on the whole cross-section, 55 m (180 ft) single-span box girder with eight webs spaced at 2.75 m (9 ft). According to the figure, an approximate 70% increase in moment is observed with the LRFD HL-93 live load.

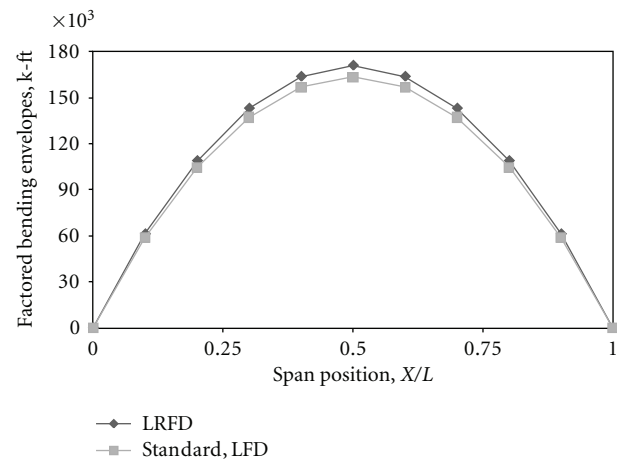
When the combined effect of live and dead loads is considered, two different service load combinations (service I and service II) are used in LRFD method when allowable compressive and tensile stresses need to be checked in prestressed concrete members. Figure 2(a) compares all three cases, showing that moments by the LRFD method are very close to that of standard specification (approximately 9% and 4% increases for Service I and II, resp.)

(i) standard specification service $DL + (LL + I)$.

(ii) LRFD service I $DL + (LL + I)$, 9% increase in moments compared to standard.



(a) Service load conditions



(b) Due to factored loads (strength I was considered for LRFD and LFD)

FIGURE 2: Comparison of moment envelopes for 180 ft single-span box girder with eight webs spaced at 9 ft.

(iii) LRFD service III $DL + 0.8(LL + I)$, 4% increase in moments compared to standard.

This is because live loads are much smaller than dead loads in a concrete bridge, and the distribution factor is smaller for LRFD. These will significantly offset the effect of the large LRFD HL-93 live load. The ultimate moment envelope combinations for standard design and LRFD specifications were also compared, and the results are shown in Figure 2(b). The following shows the load combinations:

(i) standard specification LFD combination: $M_u = 1.3(M_D + 1.67M_{D+I}) = 1.3M_D + 2.17M_{L+I}$,

(ii) LRFD load combination: $M_u = 1.25M_D + 1.75M_{L+I}$ (approximately 4% increase).

According to formulas shown above, standard design method gives higher-load factors and smaller-distribution factors as compared to LRFD. These will significantly offset the effect of higher LRFD HL-93 live load.

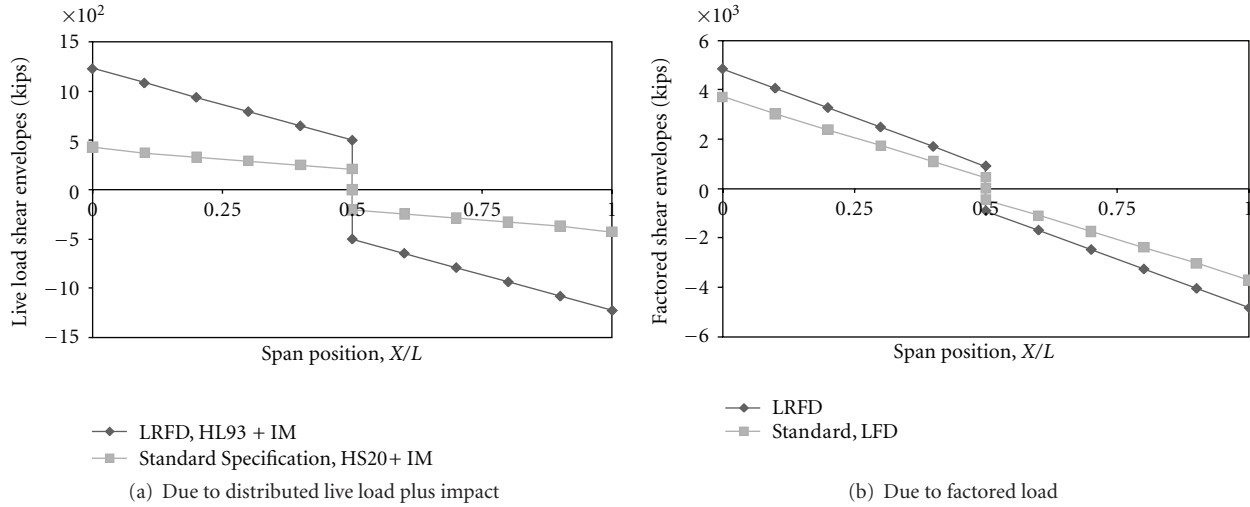


FIGURE 3: Comparison of shear force envelopes for 180 ft single-span box girder with 8 webs spaced at 9 ft.

2.2. *Live Load and Load Combinations for Shears.* In case of the live load shears, it is seen that LRFD gives a significantly higher shear force (up to 180% of those for the standard specification) as shown in Figure 3(a). This is because the LRFD shear distribution factor is significantly larger than the one in standard specification. Factored shears are compared in Figure 3(b) and the figure shows an approximately 30% increase in the use of the LRFD specification.

2.3. *Distribution Factors.* Live load distribution is one of the most important factors for a bridge design and the evaluation of existing bridges, and it has been the basis for design for several decades. The standard design specifications and LRFD specifications contain simplified methods to compute the live load effects. The new specification considers several structural properties of the bridge deck such as girder spacing, number of cells, and span length, and the examples are shown in (1) and (2) for LRFD and Standard, respectively, which shows how much the span length affects the factor.

$$(DF)_{LRFD} = \left(\frac{13}{N_C}\right)^{0.3} \left(\frac{S}{5.8}\right) \left(\frac{1}{L}\right)^{0.25}, \quad (1)$$

for interior girders (two or more lanes),

$$(DF)_{Standard} = \frac{S}{14}, \quad (2)$$

where L is span length, ft, S is girder spacing, ft, N_C is number of cells, N_G is number of girders ($N_G = N_C + 1$), L is span length, ft, and S is girder spacing, ft.

Live load distribution is one of the most important factors for a bridge design bridge and for the evaluation of existing bridges, and has been the basis for design for several decades. The standard design specifications and LRFD specifications contain simplified methods to compute the live load effects. Extensive research work has been conducted for the live load distribution factors and for simplifying the equations [4–10].

Barr et al. [4] conducted an evaluation of flexural live load distribution factors for a series of three-span prestressed concrete girder bridges. In their work, the response of one bridge, measured during a static live load test, was used to evaluate the reliability of a finite-element model scheme. Bishara et al. [5] studied distribution factor expressions for wheel-load distribution to interior and exterior girders of concrete on multisteel beam composite bridges of medium span length. According to the work, the derived distribution factor expressions give values that are generally much lower than the current AASHTO values, particularly for skew bridges. In the *National Cooperative Highway Research Program* (NCHRP) Report 592 [9], the research provided live load distribution methods which are simpler than present LRFD methods, and hundreds of bridges were analyzed with finite element analysis and simplified methods. The LRFD equations were developed based on the NCHRP Project 12–26 [10] and influenced a wide variation in modern bridge design.

A comparison of the distribution factors variation with span length can be seen in Figure 4. As shown in the figure, the LRFD predicts significantly lower values reducing with a span increase, while standard specification gives a higher value independent of span length.

2.4. *Prestressing Steel Comparison.* As discussed earlier, the LRFD live load (HL-93) is by itself significantly greater than the one compared to the standard specification live loading (HS20). For the design of prestressed members, it is considered in LRFD only 80% of the live load plus impact in its service III load combination (also refer to Figure 2). This load combination is specified only for the design of prestressed members when the tensile stress in the concrete needs to be checked. As an example, the designed number of strands for the same bridge using both methods is shown in Figure 5(a). The number of required strands in LRFD shows no significant difference with that of obtained by standard specification. This was examined for different girder

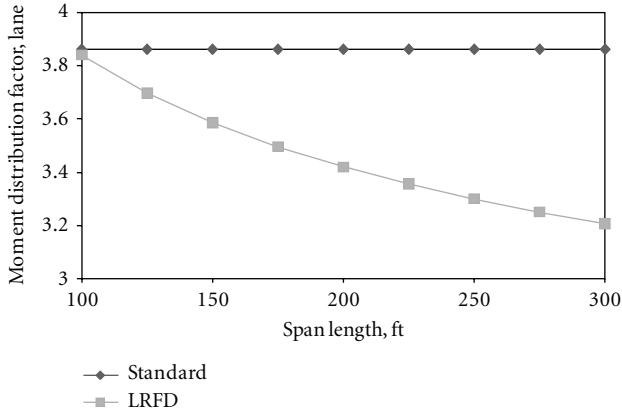
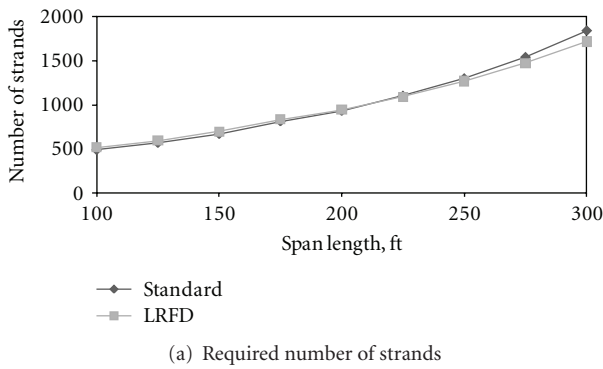
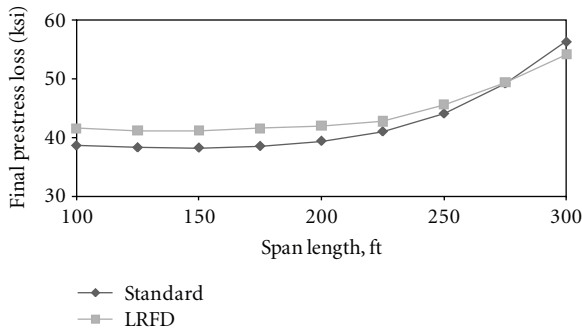


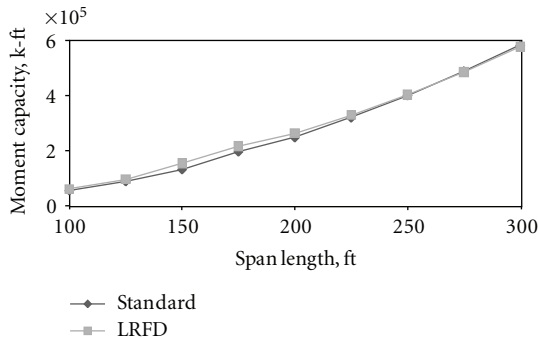
FIGURE 4: Moment distribution factors for a box girder (seven cells spaced at 9 ft) for standard and LRFD specifications.



(a) Required number of strands



(b) Final prestress losses



(c) Moment capacities

FIGURE 5: Comparison in box girder (seven cells spaced at 9 ft) for different span length.

geometries and span lengths. It was also observed that the amount of extra steel strands required by LRFD is about 3 to 4% more as compared to the standard specification.

2.5. *Prestress Losses.* Apart from the new formulation for prestressing loss due to elastic shortening in LRFD-C5.9.5.2.3b [2], other loss calculations remain unchanged. Figure 5(b) shows a comparison of final prestress losses and that the final loss predicted by LRFD is approximately 6% more than the losses predicted by the standard specification.

2.6. *Moment Capacity.* Moment capacities were calculated in accordance with both standard specification and LRFD. The same formulation of standard specification for rectangular sections is used in LRFD. Other parameters mentioned previously have minor effects and the resulting moment capacities are very close as shown in Figure 5(c).

2.7. *Superstructure Cost.* Superstructure cost for post-tensioned cast-in-place concrete box girder was calculated based on the cost estimates of similar recent projects in Arizona. Similar span-to-depth ratios, web and bottom slab thickness, and reinforcements were used for both methods. Differences in design parameters appeared to be the number of strands and deck reinforcements. The LRFD introduces two design methods for deck reinforcement, and the traditional method in this paper was used with slightly lower steel reinforcement. Among two methods, the total cost in standard specification is slightly lower when using LRFD (Figure 6).

3. Web Spacing

Web spacing S is an important parameter affecting other design variables as follows:

- (i) distribution factor (DF) is directly dependent on a value of S for both methods, and as it is seen in Figure 7, LRFD predicts smaller moment distribution factors than standard (see (1) and (2));
- (ii) top slab (deck) thickness and reinforcement are both dependent on web spacing;
- (iii) superstructure weight is depending on the number of webs and top slab thickness;
- (iv) prestressing steel area and superstructure cost are dependent on web spacing.

In the study of the effect of web spacing on other parameters, a box girder with 45.7 m (150 ft) span length and constant width of 30.5 m (100 ft) was considered. The web spacing varied from 1.83 to 5.18 m (6 to 17 ft). For each case, deck thickness, deck reinforcement, and prestressing strands were designed.

3.1. *Optimum Web Spacing.* The optimum web spacing for the box girder was considered to be the spacing for which the superstructure cost is minimized. Superstructure cost

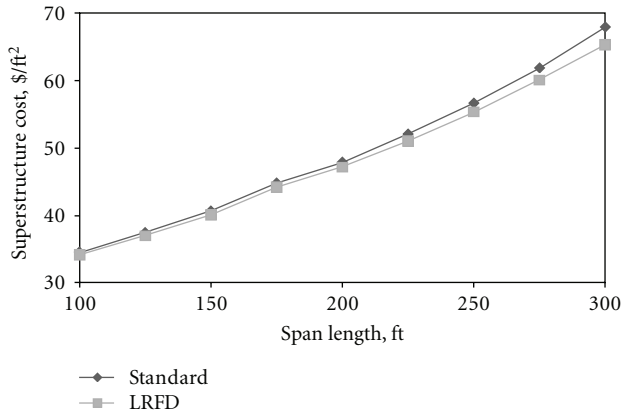


FIGURE 6: Superstructure cost, \$/ft² for a box girder (seven cells spaced at 9 ft).

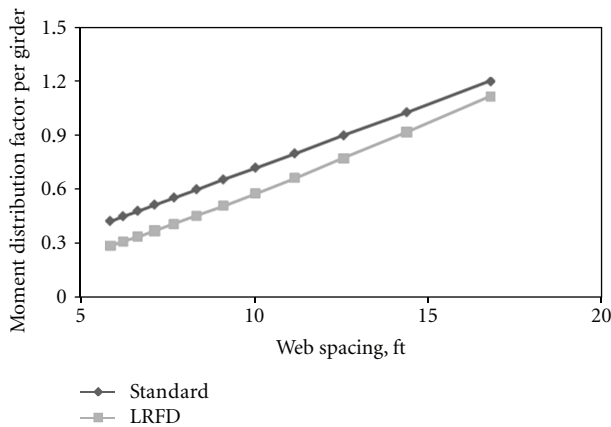
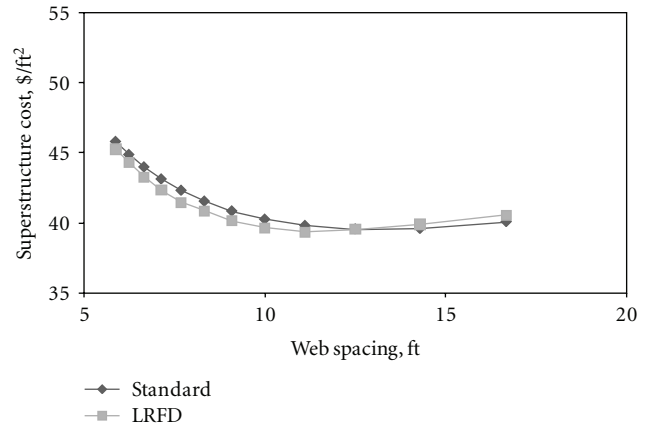
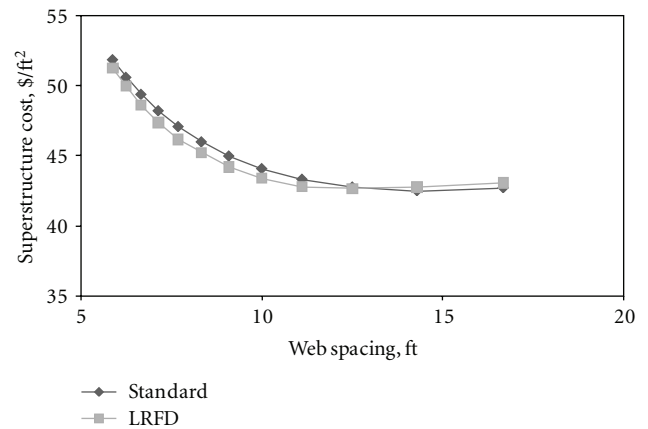


FIGURE 7: Distribution factors for box girder (150 ft span, 100 ft width, and varying web spaces).

was determined based on the cost estimates of recent similar project in Arizona. In the design process, all design constraints such as the maximum number of tendons and the maximum number of strands per tendon were considered. Any other design limitations set by the respective specifications were also considered as a constraint. Web and bottom slab thicknesses were assumed to be 30.5 cm (12 in.) and 15.2 cm (6 in.), respectively, for all design cases. The primary variable is web spacing, which will affect top slab depth, top slab steel, overall weight, prestressing steel, and shear reinforcement. As seen in Figures 8(a) and 8(b), two span lengths of 45.7 m (150 ft) and 54.9 m (180 ft) were considered for optimization process. In both cases, a minimum point can be observed on the curve corresponding to the optimum web spacing. For the 150 ft span using LRFD method, the optimum spacing is about 3.35 m (11 ft) (see Figure 8(a)). For the standard specification, the optimum distance is slightly more. Considering the 180 ft span (Figure 8(b)), the 0 minimum point is not well pronounced as it was in the previous case. Although the curve is rather flat in this region, an optimum spacing of about 3.66 m (12 ft) can still be observed.



(a) Span of 150 ft and width of 100 ft



(b) Span of 180 ft and width of 100 ft

FIGURE 8: Superstructure cost and optimum web spacing.

4. Utilization of High-Strength Concrete in Box Girders

The advantage of high-strength/high-performance concrete (HSC/HPC) has been well documented during the past 25 years. Most of the researches in this area address the importance of HPC/HSC to improve the concrete durability, physical properties (strength, creep, shrinkage, etc.) and concrete strength capacity when used as a structural member [11, 12]. It is true that poor concrete quality and lack of durability rather than structural problems cause most damages to concrete structures. Myers and Yang [13] provide a comprehensive reference list of research in this area. Several structural features can be improved and/or economized by utilization of high-strength concrete [11]. These structural features are those which are significantly dependent on concrete strength.

4.1. HSC Effect on Prestressing Steel. The required amount of prestressing steel depends on the compressive and tensile strength of concrete. The allowable compressive stress is directly dependent on concrete strength, f'_c , while the allowable tensile stress is proportional to the square root of concrete compressive strength. For calculation, it was assumed

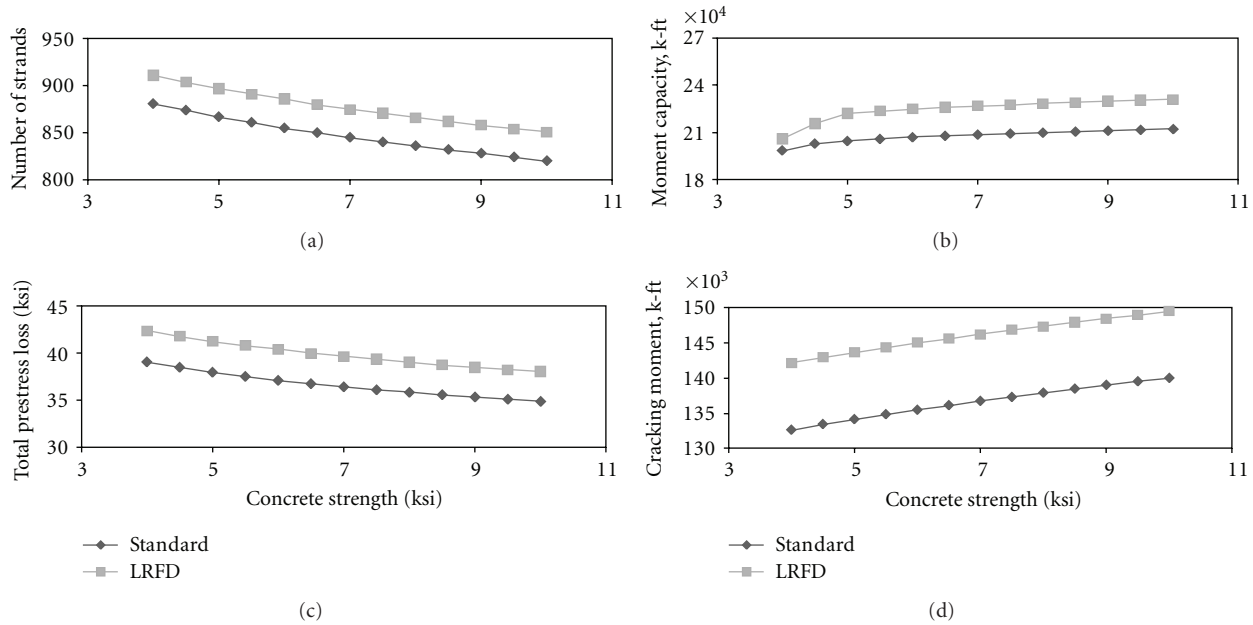


FIGURE 9: Effect of concrete strength for the span of 180 ft and 8 webs spaced at 10 ft: (a) on designed number of strands, (b) on moment capacity, (c) on final prestressing loss, and (d) on cracking moment.

that the compressive strength of the concrete at transfer is 85% of its final specified strength. For LRFD service III load combination (applied for concrete in tension), using a higher concrete strength is very helpful and provides more flexibility for the design engineer to control the stress limits within practical limitations (using specific girder geometry, web spacing, tendon profile, etc.). Similarly, for the release condition, higher concrete strength is very helpful when LRFD tensile and compressive stress limits need to be checked. Figure 9(a) shows how the number of strands decreases with an increase in concrete strength while the LRFD always requiring slightly more strands. For the special case considered, with every approximate 7 MPa (1 ksi) increase in concrete strength, a saving of 20 strands was observed.

4.2. Ultimate Bending Capacity. Bending capacity of a flexural member is not sensitive to the concrete compressive strength. It is mainly dependent on the effective depth and the amount of steel used in the section. For the strength range from 24 to 35 MPa (3.5 to 5 ksi), some increase in moment capacity can be seen (Figure 9(b)) in both methods. Considering the calculation process, it was observed that for the lower strength range, the shape of the compression zone (for moment capacity calculation) transitions from a “T” to a rectangle. LRFD introduces a new formulation for the neutral axis depth of “T” sections to obtain the bending capacity. For concrete strengths beyond 38 MPa (5.5 ksi), the moment capacity will not change significantly. It is observed that there is a little decrease (about 1%) in bending capacity with an increase in concrete strength from 35 to 70 MPa (5 to 10 ksi). The reason for decrease is that while the concrete strength is increasing, there is slight reduction in

the designed number of strands which in turn will reduce the moment capacity.

Furthermore, the number of strands was kept constant, and the effect of concrete strength was observed. A change of concrete strength from 35 to 70 MPa (5 to 10 ksi) will increase the moment capacity of the box section by only 4%, which is still insignificant. The reason is that by increasing the concrete strength, the depth of compressive zone will slightly decrease to make the same compressive force (equal to the steel tensile force). As a result, we cannot solely rely on the concrete strength to improve the bending capacity of the section.

It is worth noting here that by using higher concrete strength, in fact the compressive strain capacity of concrete will increase (approximately from 0.3% to 0.5%). This is a very good advantage, which provides more rotation capacity (and hence, ductility) for the section even though the moment capacity remains the same.

4.3. Loss of Prestress. Among several prestress losses, only elastic shortening and anchor set are dependent on the concrete modulus of elasticity, which can be improved when using high-strength concrete. The effect of concrete strength is not currently considered on creep and shrinkage of concrete, which are the two most important time-dependent parameters. It should be mentioned that a higher concrete strength may significantly reduce their effects in prestressed members. Figure 9(c) shows the effect of concrete strength on final prestressing loss.

4.4. Cracking Moment. The cracking moment depends on the tensile strength of concrete, which is in turn affected by compressive strength. An increase of 5% in cracking moment

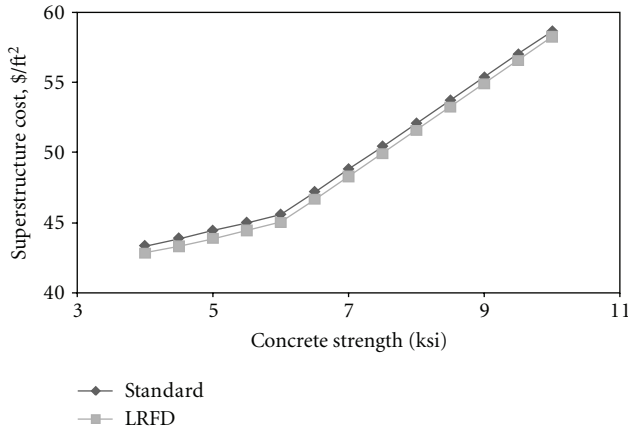


FIGURE 10: Approximate superstructure cost versus concrete strength.

may be predicted for concrete strengths changing from 35 to 70 MPa (5 to 10 ksi) (see Figure 9(d)).

4.5. Superstructure Cost. Superstructure cost will be affected by the use of high-strength concrete. For high-strength concrete the rate of cost increase is higher compared to conventional concrete (Figure 10). Since there is not a high production capacity for high-strength concrete at the present time, the anticipated cost increase may be significant. Approximate cost increase can be at least \$32/m² (\$3/ft²) of superstructure at a strength increment of 7 MPa (1 ksi). This cost increase may not be justified only for structural improvements. Considering the inherent durability improvements when using high-strength concrete, there will be significant long-term saving in the project. As it was also seen before, the superstructure cost for LRFD is slightly less than that of the standard specification. The main reason was found to be reduced deck steel calculated with LRFD.

4.6. Increase of Span Length with Concrete Strength. In the process of prestressed concrete design, the most beneficial effect of high-strength concrete would be its higher tensile strength when using LRFD service I and service III load combinations. In this part, all the parameters were kept constant except concrete strength and the span length. Figure 11 shows the capability of concrete strength to stretch the bridge span, and Table 1 summarizes the span lengths, concrete strength, and number of strands. The first two rows in the table indicate that for 51.2 m (168 ft) span length and 27.5 MPa (4 ksi) concrete, 850 strands are required. If we keep the same number of strands and increase the concrete strength to 62 MPa (9 ksi), the span length can be increased to 55 m (180 ft). Comparing second and third rows reveals that the design will need 60 strands less if 62 MPa (9 ksi) concrete is used instead of 28 MPa (4 ksi). A reduction in strands number is very helpful for condition in which the maximum number of strands per tendon becomes a controlling factor.

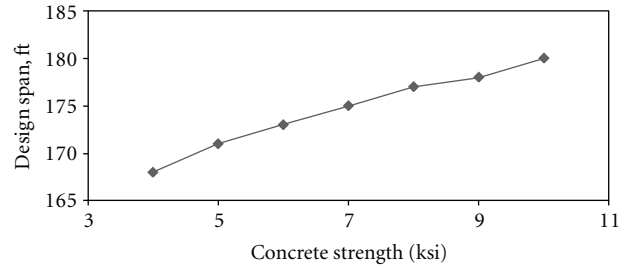


FIGURE 11: Span stretching by using higher concrete strength.

TABLE 1: Design summary.

Span length, ft	Concrete strength, ksi	No. of strands
168	4	850
180	9	850
180	4	910
168	9	800

5. Span-to-Depth Ratio

Conventionally, a span-to-depth ratio of 0.045 is used for simple span concrete box girders. Based on experiences, it seems that the use of this ratio will ensure the control of deflection. In this part of investigation, the superstructure costs were observed for different span-to-depth ratios. As it is seen in Figure 12, the lowest cost is associated with a ratio of 0.05. For example (150 ft span), it means that an extra depth of 23 cm (9 in.) will lead to a saving of almost 100 strands.

6. Conclusions

Single-span cast-in-place post-tensioned box girders were analyzed and designed according to standard and LRFD specification. The primary objective was to compare all design parameters using these specifications and also to perform some detailed parametric studies subjects such as geometrical optimization of the box girder section and structural utilization of high strength concrete (HSC). Comparison reveals that despite significant increase in live loads, other design parameters (distribution factors, load factors, and design methods) are observed as following:

Comparison of Standard and LRFD Specification. (1) The LRFD design needs slightly more (about 4%) prestressing steel as compared to the Standard Specification.

(2) Predicted shear carried by the concrete is significantly lower when using LRFD method. This will lead to a greater stirrup requirement.

(3) Final prestressing loss is about 7% more for LRFD method.

(4) Superstructure cost is slightly lower for LRFD due to introduction of new method of moment calculation in the deck slab.

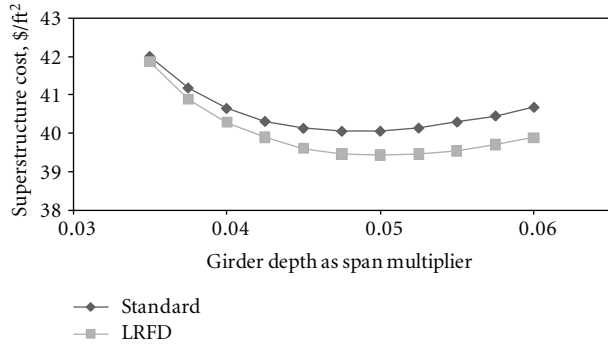


FIGURE 12: Effect of span-to-depth ratio on superstructure cost (150 ft span, eight webs spaced at 10 ft).

Optimum Web (Girder) Spacing. (5) Cost analysis and comparison shows that when changing the girder spacing, there is always a minimum superstructure cost. The girder spacing associated with that minimum cost could be considered as the optimum spacing.

(6) The optimum web spacing can be based on minimum cost. It was found that for box girders with span lengths 46 to 55 m (150 to 180 ft), the optimum web spacing is 3.35 to 3.66 m (11 to 12 ft).

Structural Effect of High-Strength Concrete. (7) Higher concrete strength provides great flexibility for designers to utilize the maximum service load capacity for the specific girder section. This advantage may result in larger span length, smaller number of strands, or wider web spacing for the same section.

(8) Using higher concrete strength will reduce final prestressing loss and the number of strands. Moment capacity is not sensitive to concrete strength, except for lower strengths (less than 31 MPa (4.5 ksi)).

(9) Anticipated cost increase for superstructure is about \$32/m² (\$3/ft²) for each 7 MPa (1 ksi) increase in concrete strength.

Span-to-Depth Ratio. (10) Compared to the LRFD-recommended depth/span ratio of 0.045, it was observed that the slightly higher ratio of 0.05 is more cost effective.

References

- [1] AASHTO, *Standard Specification for Highway Bridges*, AASHTO, Washington, DC, USA, 17th edition, 2002.
- [2] AASHTO, *AASHTO LRFD Bridge Design Specifications*, 2007 Edition and 2008 addendums, AASHTO LRFD, Washington, DC, USA, 2007.
- [3] A. S. Nowak, "Calibration of LRFD bridge code," *ASCE Journal of Structural Engineering*, vol. 121, no. 8, pp. 1245–1251, 1995.
- [4] P. J. Barr, M. O. Eberhard, and J. F. Stanton, "Live-load distribution factors in prestressed concrete girder bridges," *ASCE Journal of Bridge Engineering*, vol. 6, no. 5, pp. 298–306, 2001.
- [5] A. G. Bishara, M. C. Liu, and N. D. El-Ali, "Wheel load distribution on simply supported skew I-beam composite bridges," *ASCE Journal of Structural Engineering*, vol. 119, no. 2, pp. 399–419, 1993.
- [6] R. V. Nutt, T. Zokaie, and R. A. Schamber, "Distribution of wheel loads on highway bridges," NCHRP Project. no. 12–26, National Cooperative Highway Research Program, TRB, Washington, DC, USA, 1987.
- [7] T. Zokaie, "AASHTO-LRFD live load distribution specifications," *ASCE Journal of Bridge Engineering*, vol. 5, no. 2, pp. 131–138, 2000.
- [8] T. Zokaie, T. A. Osterkamp, and R. A. Imbsen, "Distribution of wheel loads on highway bridges," Transportation Research Record 1290, Washington DC, USA, 1991.
- [9] Bridge Tech, Inc., "NCHRP report 592: simplified live load distribution factor equations," Transportation Research Board, National Research Council, Washington, DC, USA, 2007.
- [10] Bridge Tech, Inc., "NCHRP report 12–26: simplified live load distribution factor equations," Transportation Research Board, National Research Council, Washington, DC, USA, 2006.
- [11] Z. P. Bazant and L. Panula, "Creep and shrinkage characterization for analyzing prestressed concrete structures," *Journal—Prestressed Concrete Institute*, vol. 25, no. 3, pp. 86–122, 1980.
- [12] S. H. Ahmad and S. P. Shah, "Structural properties of high strength concrete and its implication for precast prestressed concrete," *Journal—Prestressed Concrete Institute*, vol. 30, no. 6, pp. 92–119, 1985.
- [13] J. J. Myers and Y. Yang, "Practical issues for the application of high-performance concrete to highway structures," *ASCE Journal of Bridge Engineering*, vol. 6, no. 6, pp. 613–627, 2001.

Research Article

Structural Behavior and Design of Barrier-Overhang Connection in Concrete Bridge Superstructures Using AASHTO LRFD Method

Byungik Chang,¹ Kamal Mirtalaei,² Seungyeol Lee,³ and Kenneth Leitch¹

¹Department of Engineering and Computer Science, West Texas A&M University, 2403 Russell Long Boulevard, WTAMU Box 60767, Canyon, TX 79016, USA

²Engineering Technical Group, Arizona Department of Transportation, 205 South 17th Avenue, MD 618E, Phoenix, AZ 85007, USA

³Nfra Inc., 77 E. Thomas Road, Suite 200, Phoenix, AZ 85012, USA

Correspondence should be addressed to Byungik Chang, bchang@wtamu.edu

Received 9 January 2012; Revised 25 April 2012; Accepted 1 May 2012

Academic Editor: Sami W. Tabsh

Copyright © 2012 Byungik Chang et al. This is an open access article distributed under the Creative Commons Attribution License, which permits unrestricted use, distribution, and reproduction in any medium, provided the original work is properly cited.

The U.S. Departments of Transportation adopted the AASHTO LRFD Bridge Design Specifications during the year 2007, which is mandated by AASHTO and FHWA. The application of LRFD specification initiated numerous research works in this field. This investigation addresses the LRFD and Standard design methodologies of concrete deck slab, deck overhang, barrier and combined barrier-bridge overhang. The purpose of this study is to propose a simplified manual design approach for the barrier-deck overhang in concrete bridges. For concrete deck slab overhang and barrier, application of *National Cooperative Highway Research Program* crash test is reviewed. The failure mechanism, design philosophy and load cases including extreme event limit states for barrier and overhang are discussed. The overhang design for the combined effect of bending moment and axial tension is probably the most important part of the design process. The overhang might be a critical design point of the deck with significantly higher amount of reinforcement. The design process becomes complicated due to combined force effect, LRFD crash test level requirement and the existence of several load combinations. Using this program, different LRFD load combinations are plotted together with the interaction diagram and the design is validated.

1. Introduction and Background

For several years American Association of State Highway and Transportation Officials (AASHTO) standard specification [1] has been the main well-recognized bridge design tool in the United States. During the past 25 years, there have been significant developments in the concrete bridge design methods as well as utilization of new concrete materials. Many of the U.S. Departments of Transportation (USDOT) have already started the implementation of the AASHTO Load and Resistance Factor Design (LRFD) Bridge Design Specification [2]. The LRFD is based on the latest developments in structural analysis and materials to assure desired serviceability and ultimate behavior, safety, aesthetics, and economy. It benefits the valuable experiences of the AASHTO Allowable Stress Design (ASD) and Load Factor Design (LFD) methods, which have been in use for more than 70 years.

These changes resulted in design procedures significantly different compared to the earlier methods. The new LRFD specification has been calibrated to produce design results not very different with AASHTO standard specification [3]. The changes in the new LRFD design methods are significant and challenge the bridge engineers working with standard specification for so many years.

For federal funded highway projects, the USDOT have to adopt and implement the LRFD Bridge Design Specifications in 2007, which is mandated by AASHTO and Federal Highway Administration (FHWA). The task preparation of such enormous undertaking has initiated a number of research investigations of different aspects of the LRFD Specifications.

In the present work, a detailed investigation was performed to compare the difference between the Standard and the LRFD methods for interior concrete deck slab design. The purpose of this study is to propose a simplified

manual design approach for the barrier-deck overhang in concrete bridges. For the barrier and deck overhang design, a new philosophy based on yield line theory and the actual behavior in a real crash test has been used by the AASHTO LRFD specification [2]. This methodology is significantly different and more complicated comparing to the conventional methods.

2. Interior Deck Panels

A computer program (spreadsheet) was developed for interior deck panel design. The current AASHTO LRFD Bridge Design specification introduces three different deck slab design methods for its analysis. LRFD traditional methods, which are Approximate methods (LRFD Article 4.6.2) or refined methods (LRFD Article 4.6.3), and LRFD empirical design methods for concrete slabs (LRFD Article 9.7.2) are the examples [2]. The approximate method is considered acceptable for decks other than fully filled and partially filled grids, which refer to concrete slab on the top of girder, partially embedding the girder or fully embedding the girders. The refined method is typically used in modeling with finite element analysis that would affect the accuracy of the analytical solution. Empirical design method is for concrete deck slabs supported by longitudinal components and applied not to overhangs but only to the primary slab.

The LRFD traditional method using approximate methods or the refined methods is based on an elastic analysis for which the design moments have been tabulated in the specification. An LRFD empirical method is also recommended with a limitation, which is the girder spacing that must be less than 4 m (13 ft). The deck slab reinforcement given by the empirical method is a value which is dependent neither on the girder/web spacing nor on the applied dead and live load. The amount of deck reinforcement given by this method is significantly less than those given by the LRFD traditional method or Standard LFD methods, and Figure 1 compares the deck reinforcement designed by three methods.

As shown in the figure, the required amount of reinforcement is dependent on girder spacing for LFD and LRFD traditional methods while the amount of reinforcement for LRFD empirical method is constant. By adopting the empirical design method for 2.74-m (9-ft) girder spacing, the required deck steel reinforcement is about 75% and 50% of those given by LFD and LRFD traditional methods, respectively. Because of the significant difference, most of the designers probably hesitate to use the LRFD empirical method.

3. Concrete Barrier Design

A federal standard, National Cooperative Highway Research Program (NCHRP) Report 350 [4], for the safety performance evaluation of highway features has been published, and extensive experimental investigation [5–8] for the study of barrier behavior has been conducted based on the standard. The NCHRP Report covered crash tests including proposed six test levels for the bridge railing design. Based

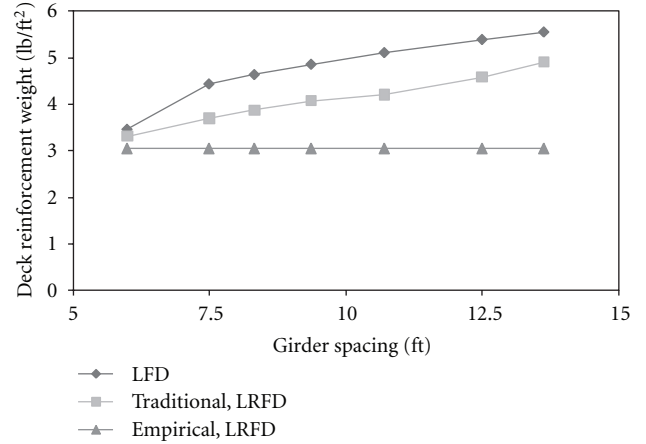


FIGURE 1: Comparison of deck reinforcement designed with different methods.

on the report, the LRFD specifies new bridge railing and concrete barrier performance level with respect to dynamic impact loads, vehicle speed, and others.

Table 1 [2] shows the minimum required design forces and dimension for traffic railing in current AASHTO LRFD Specification. In this table, the design transverse load (F_t), longitudinal load (F_L), vertical load (F_v), and other geometrical design parameters (L_t , L_L , L_v , H_e , and minimum height of rail) are given. With selecting the required crash test level, the overall barrier dimension and reinforcement will be designed using the parameters in the table. This would involve some iterative process because the magnitude and distribution of collision force depends on design capacity of the barrier.

4. Design Procedure for Concrete Railing

Yield line analysis and strength design for reinforced concrete barrier are typically used [2], and the nominal railing resistance to transverse load, R_w , can be determined using the yield line approach as shown (1) for impact within a wall (barrier) segment and for impact at end of wall (barrier) or joint, respectively. One has

$$R_w = \left(\frac{2}{2L_c - L_t} \right) \cdot \left(8M_b + 8M_w \cdot H + \frac{M_c \cdot L_c^2}{H} \right), \quad (1)$$

$$R_w = \left(\frac{2}{2L_c - L_t} \right) \cdot \left(M_b + M_w \cdot H + \frac{M_c \cdot L_c^2}{H} \right),$$

where R_w is total transverse resistance of the barrier (kip), L_c is critical length of yield line pattern (ft) = $L_t/2 + \sqrt{(L_t/2)^2 + 8 \cdot H \cdot (M_b + M_w \cdot H)/M_c}$ for impact within a wall segment = $L_t/2 + \sqrt{(L_t/2)^2 + H \cdot (M_b + M_w \cdot H/M_c)}$ for impact at end of wall or at joints, L_t is longitudinal distribution length (ft), M_b is additional flexural resistance (in addition to M_w , if any), not applicable here, M_w is flexural

TABLE 1: Minimum required design forces and dimension for traffic railing (1 kip = 4.45 kN, 1 ft = 0.31 m).

Design forces and designations	Railing test levels						
	TL-1	TL-2	TL-3	TL-4	TL-5A	TL-5	TL-6
F_t transverse (kip)	13.5	27.0	54.0	54.0	116.0	124.0	175.0
F_L longitudinal (kip)	4.5	9.0	18.0	18.0	39.0	41.0	58.0
F_v vertical (kip) down	4.5	4.5	4.5	18.0	50.0	80.0	80.0
L_t and L_L (ft)	4.0	4.0	4.0	3.5	8.0	8.0	8.0
L_v (ft)	18.0	18.0	18.0	18.0	40.0	40.0	40.0
H_e (min) (in.)	18.0	20.0	24.0	32.0	40.0	42.0	56.0
Min. H height of rail (in.)	27.0	27.0	27.0	32.0	40.0	54.0	90.0

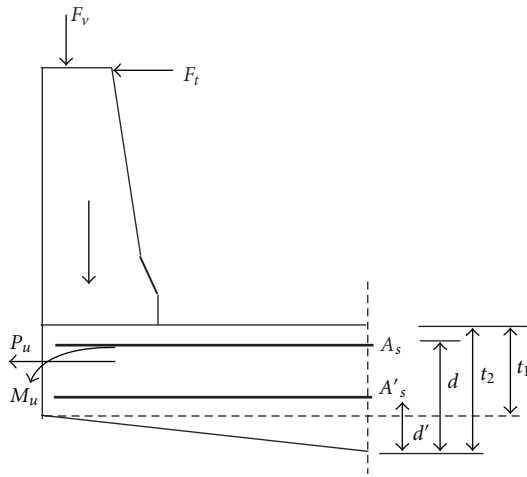


FIGURE 2: Deck overhang forces and dimensions.

resistance of the barrier about its vertical axis (k-ft/ft), M_c is flexural resistance of the barrier about its longitudinal axis (kip-ft/ft), and H is barrier height (ft).

5. Deck Overhang Behavior

LRFD specification requires that deck overhang should have sufficient strength to withstand the loads received from a vehicle crash to barrier and resistance to force the yield line failure pattern to remain within the barrier. Figure 2 shows the transverse and vertical loads (F_v and F_t) applied to the top of barrier in a crash event.

It is suggested by AASHTO LRFD specification that the concrete deck overhang should not fail in a crash event before barrier. This means that overhang also should be capable to resist the reaction forces received from the barrier during a crash [2]. The extreme event tensile force, P_u in (2), and flexural bending moment per linear foot, M_u in (3), of the deck at the barrier-overhang connection will be as follows:

$$P_u = \frac{R_w}{L_c + 2H}, \quad (2)$$

$$M_u = \frac{R_w \cdot H}{L_c + 2H}, \quad (3)$$

where R_w is total transverse resistance of the barrier (kip), L_c is critical length of yield line pattern (ft), and H is barrier height (ft).

The deck overhangs should be designed in accordance with AASHTO LRFD Section 13 (Appendix A, Article A13.4), for the following design cases considered separately.

Design Case 1. This combination is Extreme Event II which includes transverse force (F_t), longitudinal force (F_L), and other dead loads. The distributed (per foot) transverse design tensile force and its associated bending moment are P_u and M_u as calculated by (2) and (3).

Design Case 2. This combination is Extreme Event II which includes vertical force (F_v) and other dead loads.

Design Case 3. This combination is Strength I with the application of dead loads and normal vehicular live load. One wheel load will be placed at 30.5 cm (1 ft) from the face of barrier to calculate the distributed (per foot) bending moment in the overhang. An alternative equivalent continuous live load of 1 k/ft placed at 1 ft (30.5 cm) from the interior face of barrier is suggested by LRFD 3.6.1.3.4.

Note that Design Cases 1 and 2 may be considered either for continuous or joint locations at the barrier-overhang connection. Also dead load factor for Cases 1 and 2 may be assumed to be 1.0 according to LRFD Specification. Figures 3 and 4 show the bending moments along the overhang for all applicable load combinations.

6. Load Combination Comparison

The overhang length assumed to vary from 0.76 to 2.44 m (2.5 to 8 ft) in Figures 3 and 4. As it is seen, the magnitude of bending moment for Extreme Event II, with F_v application and Service I, is proportionally dependent on the overhang length. This means that by increasing the overhang length, the bending moment produced by F_v or wheel load will proportionally increase. On the other hand, for Extreme Event II, with F_t (which produces P_u and M_u), moment is almost unchanged along the overhang (except that for the effect of dead loads which is insignificant). The reason is that in these combinations a large portion of the moment on the entire length of overhang is the crash bending reaction

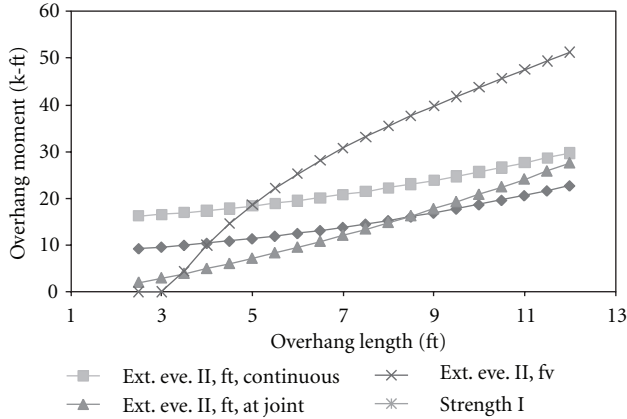


FIGURE 3: Overhang design moments for TL-4 and 32 in. barrier. Note: load combinations are the same as described in Section 6.

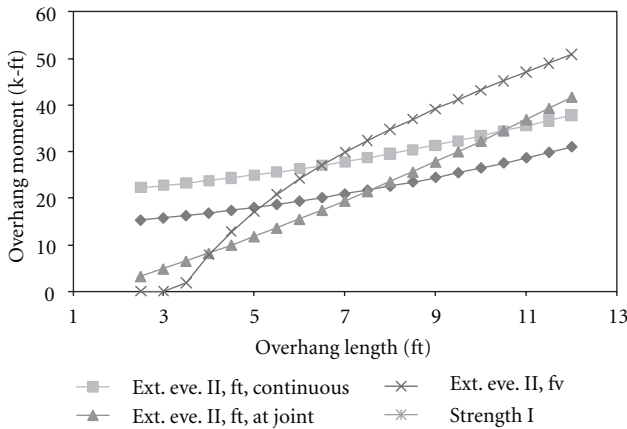


FIGURE 4: Overhang design moments for TL-5 and 42 in. barrier. Note: load combinations are the same as described in Section 6.

received from the barrier. In other words, for Extreme Event II, only two forces are considered at the tip of overhang: a tensile force (P_u) and a moment (M_u). The effect of P_u and M_u will be constant along the whole length of overhang. It is seen in Figures 3 and 4 that extreme event II load combinations are almost constant and governing the design up to an overhang length of about 1.52 to 1.98 m (5 to 6.5 ft) (which might be the maximum practical length).

For a constant force effect along the overhang length, a variable overhang thickness cannot optimize the design. If a variable thickness is used, the minimum thickness (at the tip of overhang) will govern the design. Traditionally, designers consider a variable (haunch shaped) section for the overhang with minimum thickness at its tip. It is very interesting that a variable (haunch) overhang section cannot optimize the design for Extreme Event II load combinations. Table 2 shows the axial tension and associated moment for a 1.52 m (5 ft) overhang over I girders with 81.3 cm (32 in.) barrier using AASHTO LRFD test level 4 (TL-4).

TABLE 2: Load combinations for a 5-ft overhang over I Girders and TL-4 crash loads (1 kip = 4.45 kN, 1 ft = 0.31 m).

Load combination	Tensile force, P_u kip (per foot)	Bending moment, M_u k-ft (per foot)
Extreme Event II, F_t , continuous	3.2	11.1
Extreme Event II, F_t , joint	5.2	18.1
Extreme Event II, F_v , continuous	0	8
Strength I	0	12.2

7. Axial Tension-Bending Moment Interaction

The first two load combinations in Table 2 require a design process for the rectangular concrete section under combined effect of axial force (tension) and bending moment. The manual application of classical column analysis will be time consuming and tedious. Furthermore, most of the existing column design charts are good only for axial compression which does not include the tensile portion of the column interaction curve.

It was decided in this investigation to develop a computer program in a "Spreadsheet Form" to perform this process. The program takes the initial information such as supporting elements (beams) width, overhang length and thickness (min and max in haunch shape), and material properties. The program then establishes all the load combinations (as in Table 2). It then initiates an approximate design based only on the maximum bending moment among all four load combinations (and ignoring the axial tension) to calculate the required amount of top reinforcements (A_s in Figure 2). The bottom bars (A'_s) are assumed to be similar (the continuation) to bottom bars designed for the interior panels within the same program. In the next step, a detailed section analysis is performed to construct the axial force-bending moment interaction diagram. This involves the assumptions for all possible failure modes (tensile, compression, and balance modes) to establish the failure surface. The analysis was extended for negative (tensile) axial force which is required for an overhang design.

8. Overhang Design

The calculated design combination forces (as in Table 2) are for unit width of overhang. The overhang length and material properties are also given. The program calculates the required area of top bars based only on the maximum bending from those four combinations. For initial approximation, the effect of tensile force is ignored. The overhang bottom bars are assumed to be the continuation of interior deck panel reinforcement. The interaction diagram (failure surface) can be constructed for the section. Each load combination can be plotted as a point on the same interaction diagram. The design is acceptable if all four points are inside the curve, otherwise either the slab thickness

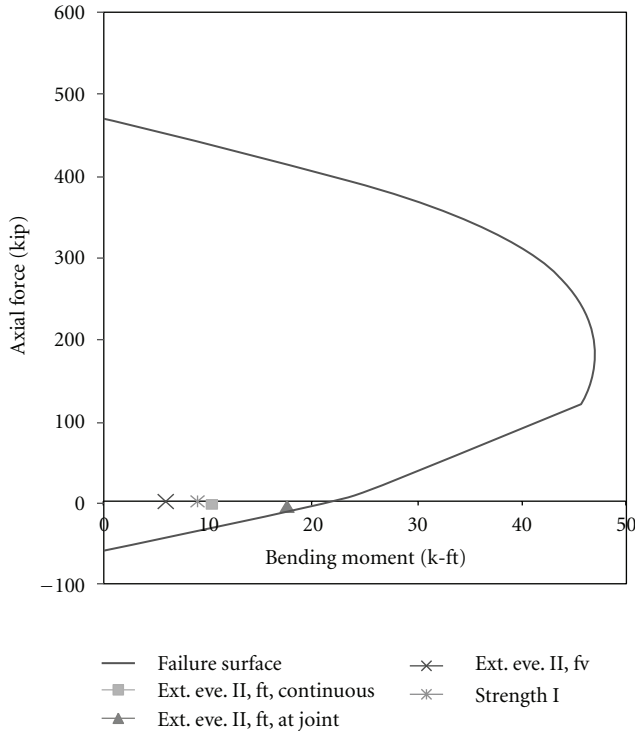


FIGURE 5: Generated interaction diagram for deck overhang.

or deck reinforcement should be revised to locate the loading points inside the curve. It should be noted that only the negative portion of diagram will be used for overhang design. Note that Load factors are according to AASHTO LRFD extreme event combination and a strength reduction factor of 0.9 applied to moments for design of steel reinforcement.

Figure 5 shows the interaction diagram with load combination plot points for a concrete overhang on AASHTO Type IV prestressed I-Girders with the following information:

Design Input. The design input includes the following:

- girder spacing = 2.44 m (8 ft),
- interior deck thickness = 20 cm (8 in.),
- overhang length from CL of girders = 2.22 m (4 ft),
- test level = TL-4,
- barrier size = 81.3 cm (32 in.),
- min. overhang thickness, $t_1 = 8$ in, and
- max. overhang thickness, $t_2 = 30.5$ cm (12 in.) (haunch).

Design Output (first run). The design output includes the following:

- overhang top transverse bars (No. 5@6 in.),
- overhang bottom transverse bars (No. 5@12 in.),
- interior panel top transverse bars (No. 5@10.3 in.),

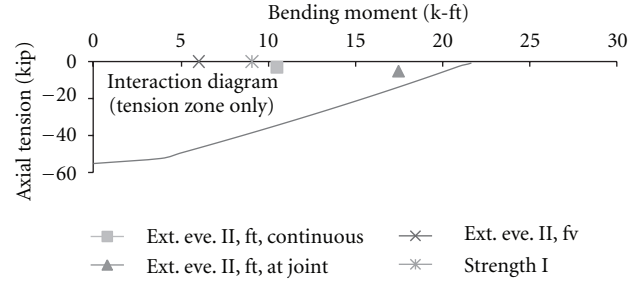


FIGURE 6: Interaction diagram for deck overhang (magnified tension part of the curve).

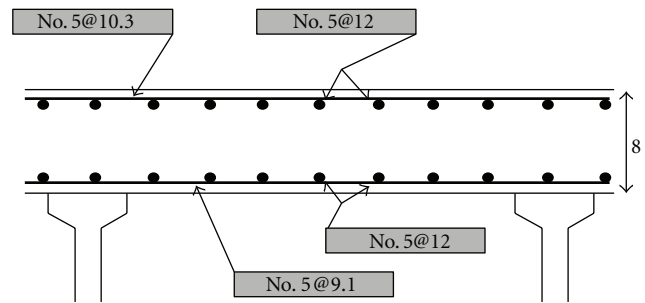


FIGURE 7: Interior deck panel LRF design output for a girder-slab bridge (unit in inch).

interior panel top transverse bars (No. 5@10.3 in.), and

interior panel bottom transverse bars (No. 5@9.1 in.).

Figure 6 is an exploded view of tensile portion of the interaction diagram. It is seen that all the load combination points are inside the curve, and the design requirements are satisfied.

Computer output for the design of interior panels and overhang portion of concrete deck slab are shown in Figures 7 and 8.

9. Significance of Design Variables

Several deck overhangs with different geometries were designed to observe the significance of each design variable.

9.1. Load Combinations. It is important that the extreme event load case with transverse crash force transfers a constant bending moment and tensile force along the entire length of deck overhang. This is unlike the effect of wheel live load which produces variable moment (zero to maximum). It is seen in Figures 3 or 4 if the first and second load cases (which are almost flat) are compared with third and fourth cases (which are approx. linear). For this reason, the conventional common practice to use variable (haunch) overhang thickness will not help if one of the first two cases is governing the design. It was observed that the first two extreme event load combinations will govern the overhang

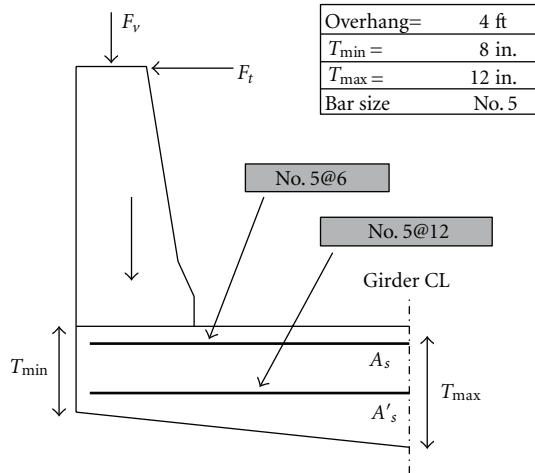


FIGURE 8: Deck overhang LRFD design output for a girder-slab bridge.

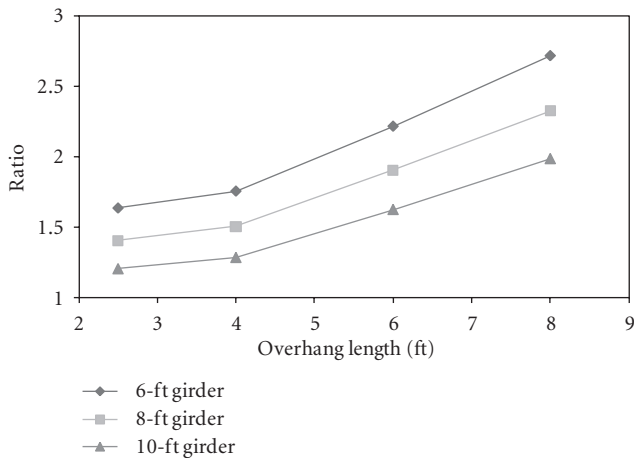


FIGURE 9: Significance of overhang top bars.

design up to lengths of 5 ft and 6.5 ft for test levels of TL-4 and TL-5, respectively. These lengths are probably the maximum practical limits. If a variable thickness is used, the deck section and reinforcements at the barrier location must be used for design. Deck overhang section at a point under the interior face of barrier was used in this program.

9.2. Barrier Ends or Joints. The ends or joint locations create a more critical failure in the barrier (and hence the deck) compared to continuous points. Compare joint and continuous cases (the first two load combinations) in Figures 2 and 3. At joints or barrier ends, the crash bending moment is about 60% to 75% higher than continuous locations. The barrier and deck overhang should be designed properly at these points.

9.3. Significance of Overhang Reinforcement. A comparison was performed between required overhang top reinforcement with the adjacent interior panel top bars, and Figure 9 shows the ratio of required overhang to interior panels'

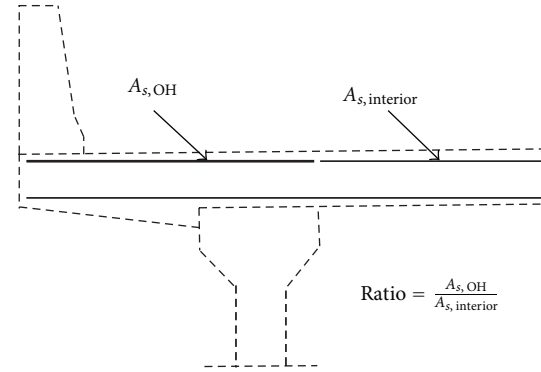


FIGURE 10: Overhang and interior top bar comparison.

top reinforcement. The vertical axis shows the ratio (see Figure 10) of top bars of overhang to top bars of adjacent interior panel. It was shown that this ratio will significantly increase with overhang length.

9.4. Overhang Design. Direct manual design of reinforced concrete section under combined tension and bending seems to be time consuming and tedious. Numerous examples were solved with this automated computer method. It was observed that, for overhang length limits mentioned before, a simplified manual design can be established as follows.

- (i) The top bars in the overhang may be designed based on maximum bending moment (and ignoring the associated tensile force) among the four load combinations (most of the time the first or second case, the extreme event for F_t is critical). For simplicity, the effect of bottom bars can be ignored in this process. In case of variable (haunch) thickness, the design should be based on the deck section properties at the location of barrier-to-deck connection (which has the least thickness).
- (ii) The bottom bars in the overhang may be assumed to be similar to bottom bars of the adjacent interior deck panel. This means that we can simply continue the bottom bars from the interior panel into the overhang.

10. Conclusion and Suggested Simplified Design Method

Detailed investigation was performed for the concrete deck slabs by developing a spreadsheet computer program. Different design methods for the interior deck panels were compared. By adopting the empirical design method for 2.74-m (9-ft) girder spacing, the required deck steel reinforcement is about 75% and 50% of those given by LFD and LRFD traditional methods, respectively. Because of the significant difference, most of the designers probably hesitate to use the LRFD empirical method.

For barrier-overhang interaction and their design, NCHRP crash test data were incorporated into the program to check the barrier adequacy. For most practical cases,

the overhang design is governed by extreme event limit state load data given by crash test results. This requires the concrete section to be designed for combined effect of bending moment and axial tension. The program is capable to construct the axial load and bending moment interaction diagram and check the design adequacy for crash extreme events and strength limit states. A simplified manual design approach was also proposed.

The following shows the simplified design method suggested based on this study. This design method will pass the LRFD crash forces for most practical cases. It was shown that this simplified method is acceptable for overhangs up to 7 ft for a crash level of TL-4.

- (1) Design the top bars for Extreme Event crushing moment caused by F_t only (ignoring the axial tension).
- (2) Provide nominal bottom bars (or continuation of designed adjacent internal panel bottom bars).

References

- [1] AASHTO, *Standard Specification for Highway Bridges*, AASHTO, Washington, DC, USA, 17th edition, 2002.
- [2] AASHTO, *AASHTO LRFD Bridge Design Specifications*, AASHTO LRFD, Washington, DC, USA, 2008.
- [3] A. S. Nowak, "Calibration of LRFD bridge code," *ASCE Journal of Structural Engineering*, vol. 121, no. 8, pp. 1240–1251, 1995.
- [4] H. E. Ross Jr., D. L. Sicking, and R. A. Zimmer, "National Cooperative Highway Research Program (NCHRP), Report 350: Recommended Procedures for the Safety Performance Evaluation of Highway Features," Tech. Rep., Transportation Research Board, National Research Council, Washington, DC, USA, 1993.
- [5] E. C. Lohrey, "Three (3)-Year Field Evaluation of the Narrow Connecticut Impact-Attenuation System (NCIAS)," Tech. Rep. 1221-F-94-3, Research Project HPR-1221, 1994.
- [6] J. F. Carney III, C. E. Dougan, and E. C. Lohrey, "Summary of the NCHRP Report 350 Crash Test Results for the Connecticut Truck Mounted Attenuator," Tech. Rep. 2216-1-95-2, 1995.
- [7] W. L. Menges and C. E. Buth, "NCHRP Report 350 Testing of the Narrow Connecticut Impact Attenuation System (NCIAS)," Tech. Rep. TTI: 404231-1-6, 1999.
- [8] E. Smith, "Summary of the NCHRP Report 350 Crash Test Results for the narrow Connecticut Impact Attenuation System," Tech. Rep. 2216-2-02-5, 2003.

Research Article

Behavior of FRP Link Slabs in Jointless Bridge Decks

Aziz Saber and Ashok Reddy Aleti

Department of Civil Engineering, Louisiana Tech University, 600 West Arizona Avenue, Ruston, LA 71272, USA

Correspondence should be addressed to Aziz Saber, saber@latech.edu

Received 4 January 2012; Revised 23 March 2012; Accepted 24 March 2012

Academic Editor: Sami W. Tabsh

Copyright © 2012 A. Saber and A. R. Aleti. This is an open access article distributed under the Creative Commons Attribution License, which permits unrestricted use, distribution, and reproduction in any medium, provided the original work is properly cited.

The paper investigated the use of fiberglass-reinforced plastic (FRP) grid for reinforcement in link slabs for jointless bridge decks. The design concept of link slab was examined based on the ductility of the fiberglass-reinforced plastic grid to accommodate bridge deck deformations. The implementation of hybrid simulation assisted in combining the experimental results and the theoretical work. The numerical analyses and the experimental work investigated the behavior of the link slab and confirmed its feasibility. The results indicated that the technique would allow simultaneous achievement of structural need, lower flexural stiffness of the link slab approaching the behavior of a hinge, and sustainability need of the link slab. The outcome of the study supports the contention that jointless concrete bridge decks may be designed and constructed with fiberglass-reinforced plastic grid link slabs. This concept would also provide a solution to a number of deterioration problems associated with bridge deck joints and can be used during new construction of bridge decks. The federal highway administration provided funds to Louisiana Department of Transportation through the innovative bridge research and development program to implement the use of FRP grid as link slab.

1. Introduction

Thousands of bridges in the United States are constructed as simple spans. The bridges require the use of expansion joints over piers. The joints create short-term and long-term problems. Some examples of these problems are leaks through the joints deteriorating the supporting girders and the piers and debris accumulating in the joints which prevents them from functioning properly. These problems lead to massive direct and indirect costs (Saber et al. [1, 2]). Therefore there is a need for reducing or eliminating expansion joints in bridge decks. The objectives of this study are to develop and evaluate a new technique using advancement in materials and current technology. An innovative system is proposed for this study. The new system replaces expansion joints with a link slab. The link slab joins decks of adjacent spans without imposing any continuity in the bridge girders. The link slab is subjected to tensile forces and stresses due to the negative moment developed at the joint. Fiberglass-reinforced plastic (FRP) reinforcement is used to carry the tension forces (Saber [3]) and its corrosion resistance.

The most common type of reinforcement used in bridge construction is steel rods. The deterioration of steel caused

by corrosion has been plaguing these structures across the nation, decreasing their service life, and increasing the cost of repair and maintenance. Many investigations were conducted to resolve the problems associated with corrosion by such methods as decreasing the porosity of concrete, coating steel bars with a protective outer layer, and increasing the reinforcement cover. But these methods only extend the time it takes for corrosion to take place.

For more than three decades, researchers have investigated the use of FRP (fiberglass reinforced polymers) as an alternate to steel reinforcement in concrete structures. In recent years, the use of FRP rods for structural applications has been gaining acceptance around the world. Recently FRP grids have been used for reinforcement of concrete beams and slabs (Dutta et al. [4]). A grid is a latticework of rigid, interconnecting ribs in two, three, or four groups and directions. Such grid reinforcement enhances the energy absorption capability and the overall ductility of the structure is improved. This leads to an increase in the ultimate load carrying capacity of concrete beams and slabs. When the opening of grids is filled with concrete, the combined structure derives its shear rigidity from the concrete filler and the concrete prevents the ribs from buckling. FRP composite

grids provide a mechanical anchorage within the concrete due to the interlocking elements (cross-ribs), and therefore no bond is necessary for proper load transfer.

Although there have been a number of studies on the use of FRP-grid-reinforced concrete beams or slabs, there is currently a lack of information on the use of FRP-grid-reinforced concrete link slabs for the replacement of expansion joint. Because the link slab will be subjected to a negative bending moment and thermal stress, it is expected that the design and performance will be different from conventional beams or slabs, which is primarily subjected to a positive bending moment and transverse shear force. Therefore, there is a need to conduct experimental testing and theoretical modeling analysis of FRP-grid-reinforced concrete link slabs for the replacement of expansion joints.

2. Experimental Work

A test program was conducted to determine the behavior and strength of jointless bridge decks under static loading. The jointless decks could be achieved by replacing expansion joints with a link slab that could join bridge decks of adjacent spans without imposing any continuity in the bridge girders. The link slab would be subjected to tensile forces due to negative moment developed at the location of the joint. The link slab panel was cut into beam specimens to determine the strength of the link slab against tensile forces. The test program included specimens with two layers of FRP grids. The specimens were tested under the same support conditions. Loads, deflections, strains, and load carrying capacity were measured for each test specimen.

2.1. Test Specimens. The specimens were designed as per ASTM C 78, ACI 318, and ACI 440 guidelines, [5, 6]. Since there was no design code for FRP-grid-reinforced concrete beams, the existing design equations in ACI 440 for FRP rebar-reinforced concrete beams were modified and used. The cross section of the specimens was rectangular in shape with a width of 300 mm (1 ft), 200 mm (8 in) deep, and 2.4 m (8 ft) long. The FRP grids were placed in the center 1.2 m (4 ft) of the beams. The first specimen, beam 1, contained two layers of FRP grid; each is 25 mm (1 in) deep, 1.2 m (4 ft) long, and 225 mm (9 in) wide. The clear spacing between the two FRP grids was 25 mm (1 in). Shear reinforcement was not provided to the beams since the depth of the beam did not exceed the requirements of ACI 318 [5]. Also, three number 13 (number 4) rebars were placed in the specimens for handling. The dimensions and cross-section details of the beam 1 were shown in Figures 1 and 2, respectively.

The second beam, beam 2, contained two layers of 31 mm (1.25 in) deep FRP grids, 1200 mm (4 ft) long, and 225 mm (9 in) wide. The dimensions and cross-section details of beam 2 were similar to beam 1, as shown in Figure 3. The two rectangular beams were cast from the batch delivered by a ready mix truck to the Structural and Materials Laboratory at Louisiana Tech University. To simulate field conditions, the beams were cured in dry air conditions for 28 days before they were tested.

The specimens were tested under the same set-up as shown in Figure 1. The applied loads and reactions were symmetrical with respect to the center of the beam. The specimen was placed on a high reaction stand of a stiffened steel section. At each reaction point, a roller support was placed between the specimen and the steel section. Load was applied by an MTS hydraulic jack at load points. A steel section was used between the hydraulic jack and the beam specimen to apply the load equally at the load locations. At the load points, roller supports were provided to disperse the load from the steel section to the specimen. The jack was activated by a single automatic MTS electric pump.

2.2. Instrumentation Plan. The instrumentation used for the testing of each beam included a deflectometer, a twenty-four channel data acquisition system, and 50 mm (2 in) long strain gages installed at locations on the FRP grids where the shear forces and bending moments were high. The strain gages were installed on the outer surface along the longitudinal direction. The top grid was designated as layer 1 and the bottom grid was designated as layer 2. Layer 1 strain gages were designated as L1G1 through L1G8 from left end to the right end of the grid. Similarly, layer 2 strain gages were designated as L2G1 through L2G8 from left end to the right end of the grid. The deflection of each beam was measured during the test by a deflectometer placed at the midspan of the beam.

2.3. Test Procedure. A four-point bending test was conducted, and the test load was applied in such a way that a negative bending moment was produced in the beam at the FRP grid locations. The beams were loaded continuously at a constant rate of 8.9 kN/min (2 kip/min) until failure. The four-point bending tests were conducted using the MTS machine. The data collection system stored the strain and load data for every quarter second. For each load increment, data for the FRP strains and loads were collected. The applied loads and corresponding deflections at midspan for each beam were measured during the tests.

2.4. Material Characteristics. The concrete mix constituents were shown in Table 4. The concrete cylinders were cast from the same batch delivered by a local ready mix truck to the Structural and Materials Laboratory at Louisiana Tech University.

The concrete cylinders 100 × 200 mm (4 × 8 in) were cured in accordance with ASTM C511, and the compressive strength was determined in accordance with ASTM C39. The average compressive strength of three cylinders was recorded for each test day and the strength development over time is shown in Figure 4. When the beam specimens were tested at 28 days, the compressive strength of the concrete was 36.4 MPa (5277 psi).

The material properties of FRP grid were obtained from the manufacturer (Fibergrate, Composite Structures) and were listed in Table 1.

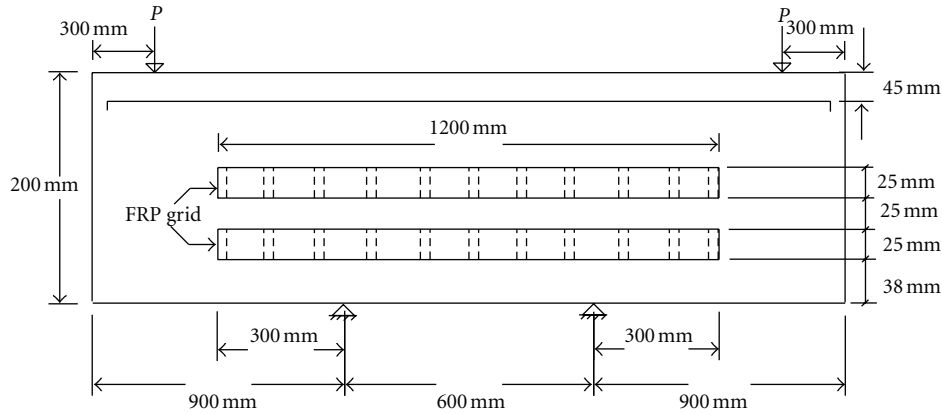


FIGURE 1: Beam 1 dimensions (not to scale).

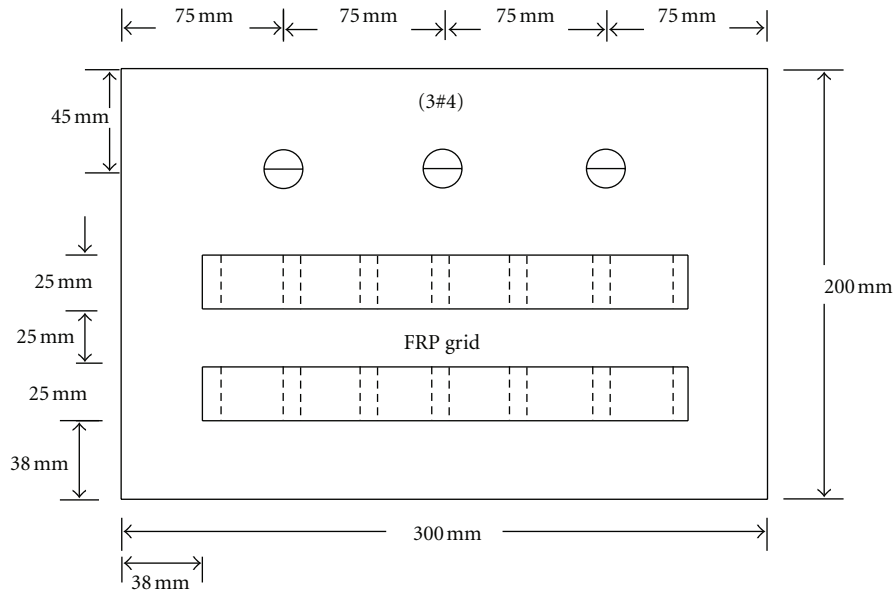


FIGURE 2: Beam 1 cross-section details.

TABLE 1: Concrete mix proportions.

Cement	222 kg/m ³ (489 lb/yd ³)
Fly Ash	55 kg/m ³ (122 lb/yd ³)
Coarse aggregate pea gravel	849 kg/m ³ (1870 lb/yd ³)
Natural Sand	602 kg/m ³ (1325 lb/yd ³)
Admixture (900 P0Y-5)	0.53 liter/m ³ (18 Oz/yd ³)
Air content	0.05
Slump	125 mm (5 inch)
Water	112 liter/m ³ (29.5 gal/yd ³)

2.5. *Experimental Results.* The specimens were designed to be underreinforced so that large strains in FRP grids preceded the crushing of the concrete in compression. The discussion will be given on strain responses up to failure, the overall load/deflection, and the mode of failure of the

specimens. The beams were designed to have ductile failure at the ultimate load, as would be the case for existing bridge decks in service. The flexural cracks formed in the constant moment region extended vertically and became wider and then progressed towards the load points in a diagonal fashion. The beam then collapsed as shown in Figure 5.

2.6. *Beam 1 Failure.* The longitudinal strains in the FRP grids due to the applied loads were recorded. The strain data in the cantilever section indicated that the longitudinal strain distribution followed the bending moment diagram. In Figures 6 and 7, the data obtained from the strain gages indicated that at higher loads the longitudinal strains in the shear spans increased above those of a linear variation. This showed that strains were not proportional to the applied moment at these locations. At ultimate conditions, the axial

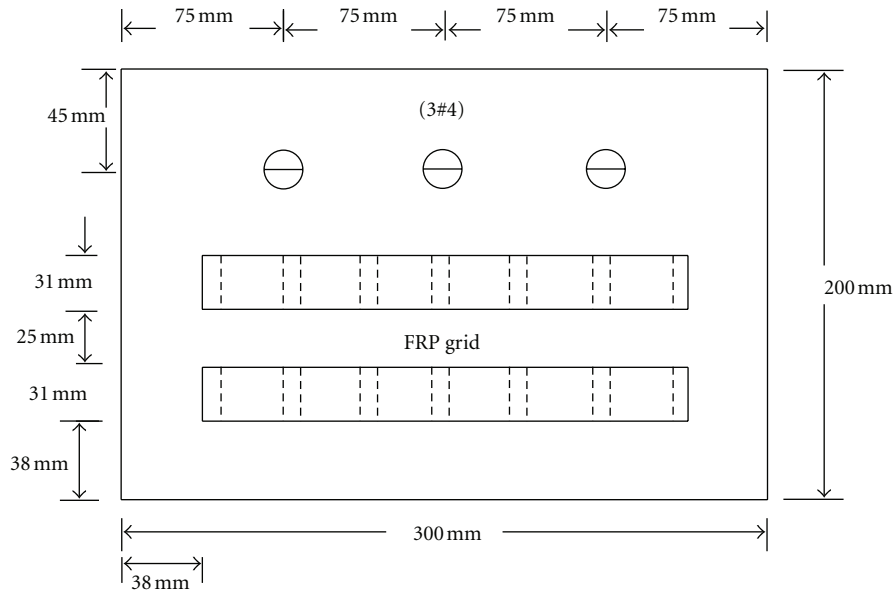


FIGURE 3: Beam 2 cross-section details.

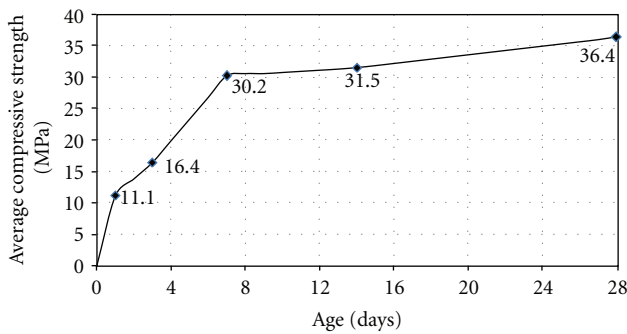


FIGURE 4: Concrete average compressive strength.



FIGURE 5: Beam 2 at collapse.

strain in the FRP grid varied linearly along the end of the FRP grid and at the point of load. Based on the previous discussion, it was concluded that the bond between the FRP grid and concrete is uniform. Moreover, the data in Figures

TABLE 2: FRP grid material properties provided by manufacturer.

Material characteristics	Value
Tensile stress, LW	207 MPa (30,000 psi)
Tensile modulus, LW	17.2 GPa (2.5×10^6 psi)
Compressive stress, LW	207 MPa (30,000 psi)
Compressive modulus, LW	17.2 GPa (2.5×10^6 psi)
Flexural stress, LW	207 MPa (30,000 psi)
Flexural modulus, LW	12.4 GPa (1.8×10^6 psi)
Shear modulus	3.1 GPa (0.45×10^6 psi)
Short beam shear	31 MPa (4,500 psi)
Punch shear	68.9 MPa (10,000 psi)
Bearing stress, LW	207 MPa (30,000 psi)
Area of 1 inch deep FRP per 9 inch width per layer	894 mm ² (1.43 in ²)
Area of 1.25 inch deep FRP per 9 inch width per layer	1112 mm ² (1.78 in ²)

6 and 7 indicated that the variations in the strain with the load at the beam center were slightly higher than those close to the load point, but the two curves were of similar form. As the applied load increased, the rate of change in the strains in the shear span was higher than that in the constant moment region. The higher rates demonstrated the initiation and progress of cracking in the region close to the support. The high level of strains in the shear span explained the flexural/shear cracking in the collapse mechanism for the beam.

2.7. *Strains in Beam 1 Layer 1.* A total of eight strain gages were installed to monitor the strain distribution. The strains measured were tensile strains in all of the gages

TABLE 3: Maximum flexural stresses for bottom elements for bridge girders.

Girder number	Open joint bridge (OBJ) maximum flexural stress (MPa)	Link slab bridge (LSB) maximum flexural stress (MPa)	Percentage of decrease in girder stresses due to link slab
S1G1	2.13	1.75	18%
S1G2	2.55	2.07	19%
S1G3	2.53	2.12	16%
S1G4	2.16	1.69	22%
S2G1	0.82	0.54	34%
S2G2	0.82	0.55	33%
S2G3	0.83	0.57	32%
S2G4	0.80	0.54	32%
S3G1	0.63	0.56	12%
S3G2	0.65	0.59	10%
S3G3	0.65	0.59	9%
S3G4	0.65	0.56	14%

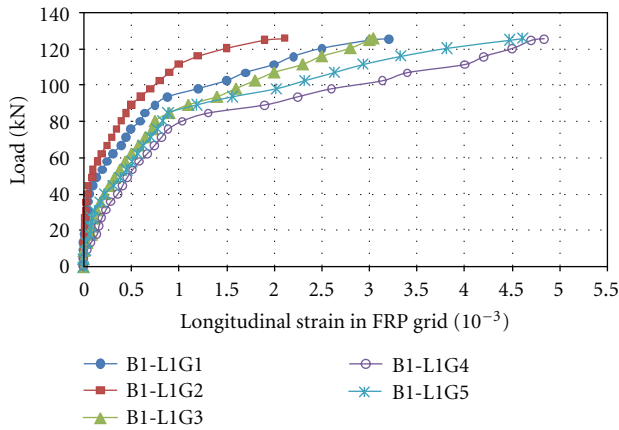


FIGURE 6: Load/strain along FRP grid for layer 1 in beam 1.

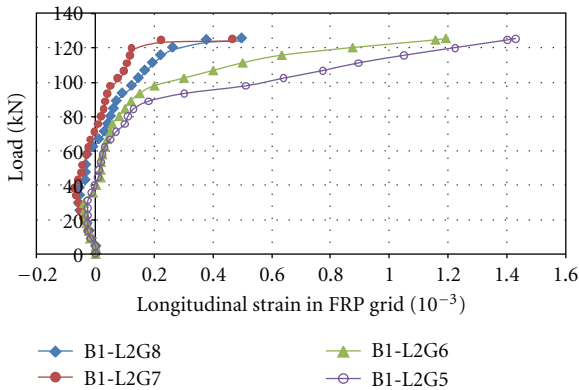


FIGURE 7: Load/strain along FRP grid for layer 2 in beam 1.

at different applied loads for the ultimate load test. These measurements indicated that the grid was in tension. Among all the gages, maximum tensile strain was found in gage 4 (B1-L1G4), which was located just right of the left support.

The maximum strain was 4.8 milli strains at the ultimate load of 125.5 kN (28.2 kips). The tensile modulus of the grid was 17.2 GPa (2.5×10^3 ksi). Therefore, the tensile stress corresponding to maximum tensile strain was 82.7 MPa (12.0 ksi) which is 40% of the maximum tensile stress recommended by the manufacturer, as shown in Table 1. The load-strain relationship was linear up to the load level of 75.6 kN (17 kip) when the beam began to yield. The load-strain distribution of gage 5 in layer 1 (B1-L1G5) located at the center of grid and beam indicated that the changes in the strains were low up to the load level of 84.6 kN (19 kip), and after that, change in strains were higher until the ultimate load was reached. The strain distribution for layer 1 of beam 1 indicated that as the applied load increases towards its maximum value, the distribution of strain in the FRP grid became unsymmetrical.

2.8. *Strains in Beam 1 Layer 2.* The strains measured were compressive strains in all the gages up to an applied load of 40 kN (9 kips). Then the measured strains were changed to tensile strains for the ultimate load test. These measurements indicated that the grid was in compression until the applied load reached a value of 40 kN (9 kip); then the grid was in tension. Among all the gages, the maximum compressive strain was found in gage 7 (B1-L2G7) located at 1.65 m (66 in) from the left end of the beam at an applied load of 40 kN (9 kips). The load-strain distribution of gage 7 in layer 2 (B1-L2G7) indicated that the maximum compressive strain was -0.074 millistrains. The compressive modulus of the grid was 17.2 GPa (2.5×10^3 ksi). Therefore, the compressive stress corresponding to maximum compressive strain was 1.24 MPa (0.18 ksi) which is 0.6% of the maximum compressive stress recommended by the manufacturer. The maximum tensile strain was found in gage 4 (B1-L2G4) which was located at just right to the left support. The maximum strain was 1.6 millistrains at the ultimate load 125.5 kN (28.2 kips). The tensile modulus of the grid was 17.2 GPa (2.5×10^3 ksi). Therefore, the

tensile stress corresponding to maximum tensile strain was 27.4 MPa (3.98 ksi) which is 13.3% of the maximum tensile stress. The strain distribution for layer 1 of beam 2 indicated that as the applied load increased towards its maximum value, the distribution of strain in the FRP grid became unsymmetrical.

2.9. Beam 2 Failure. The same discussion presented previously applies to the behavior for beam 2 with two 31 mm (1.25 in) FRP grids. The strain distribution in the FRP grid in layer 1 of the specimen beam 2 is shown in Figure 8.

2.10. Strains in Beam 2 Layer 1. A total of eight strain gages were installed to monitor the strain distribution. The strains measured were tensile strains in all the gages at different applied loads for the ultimate load test. These measurements indicated that the grid was in tension. Among all the gages, maximum tensile strain was found in gage 4 (B2-L1G4), which was located at just right to the left support. The maximum strain was 4.0 millistrains at the ultimate load of 113.9 kN (25.6 kips). The tensile modulus of the grid was 17.2 GPa (2.5×10^3 ksi). Therefore, the tensile stress corresponding to maximum tensile strain was 69.6 MPa (10.1 ksi) which is 34% of the maximum tensile stress recommended by the manufacturer. The load-strain distribution of gage 5 in layer 1 (B2-L1G5) located at the center of grid and beam indicated that at higher loads, strain varied linearly with the applied loads.

2.11. Strains in Beam 2 Layer 2. The strains measured were compressive strains in all eight gages up to an applied load of 62.3 kN (14 kips); after that, the measured strains were changed to tensile strains for the ultimate load test. These measurements indicated that the grid was in compression till the applied load reached a value of 62.3 kN (14 kips); then the grid was in tension. Among all the gages, the maximum compressive strain was found in gage 7 (B2-L2G7) located at right end of the grid at an applied load of 31.2 kN (7 kips). The load-strain distribution of gage 7 in layer 2 (B2-L2G7) indicated that the maximum compressive strain was -0.058 millistrains. The compressive modulus of the grid was 17.2 GPa (2.5×10^3 ksi). Therefore, the compressive stress corresponding to maximum compressive strain was 1 MPa (0.15 ksi) which is 0.5% of the maximum compressive stress recommended by the manufacturer. The maximum tensile strain was also found in gage 7 (B2-L2G7). The maximum strain was 0.21 millistrains at the ultimate load 114 kN (25.6 kips). The tensile modulus of the grid was 2.5×10^3 ksi. Therefore, the tensile stress corresponding to maximum tensile strain was 3.7 MPa (0.53 ksi) which is 1.8% of the maximum tensile stress.

2.12. Load-Deflection Behavior. All specimens were tested in a four-point bending configuration. The ultimate loads and corresponding deflections for both beams were measured during the tests. The load carrying capacity of the beam 1 was 125.5 kN (28.2 kips) and that for beam 2 was 114 kN (25.6 kips). The deflection of each beam at collapse was

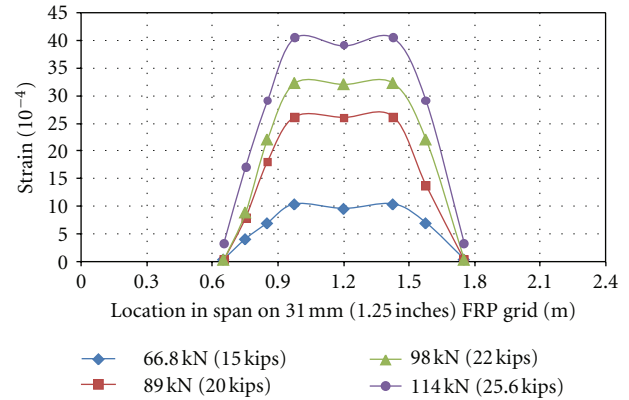


FIGURE 8: Longitudinal strain along FRP grid for layer 1 in beam 2.

substantial ($L/240$) accompanied by excessive cracking. The load deflection response of the specimens exhibited three regions of behavior. At low applied loads the stiffness of the reinforced concrete beam was relatively high, indicating that the concrete behaved in a linear elastic manner. As the load increased, the bending stress in the extreme fibers increased until the tensile strength at the top of the section of the concrete was reached. This caused flexural cracks to form, first in the constant moment region, then through the beam cantilever section. As the flexural cracks developed in the span, the member stiffness was reduced and the response after the cracking load was approximately linear due to the postcracking stiffness. After the concrete in the tension zone cracked, the FRP grid carried the tensile forces due to applied loads. As the applied load increased, the tensile stress increased the, beam stiffness was decreasing due to the loss of material stiffness, and the ability of the section to support the tensile stress was reduced. The yield plateau in the slope-deflection curve for beam 2 was longer than that of beam 1, which indicated that beam 2 was more ductile than beam 1, even though the areas of the FRP grids in beam 2 were greater than beam 1.

3. Theoretical Work

In this study, finite element models are developed to investigate the behavior of the bridge with link slabs. Two models are considered, one with open joints and another with the joints closed over the supports. The results of the models are compared and used to evaluate the structural behavior of the FRP-grid-reinforced link slab.

3.1. Bridge Model Description. The bridge models were developed using the software ANSYS. A typical three-span bridge was considered. In each span, four AASHTO Type III girders, end and intermediate diaphragms were modeled. The dimensions of the deck in the z -axis were 18 m (60 ft) long, 9 m (30 ft) wide in the x -axis, and 200 mm (8 in) thick in the y -axis. A gap of 25 mm (1 in) and 150 mm (6 in) was considered between two adjacent decks (open joint) and

two girders in adjacent spans, respectively. The center-to-center distance between adjacent girders in a span was 2.6 m (104 in). The end diaphragms were provided between two adjacent girders, from the middepth of girder to the bottom of the top flange. The intermediate diaphragms were placed from the top of bottom flange to the bottom of the top flange (Saber et al. [7]) The thickness of the intermediate and end diaphragms was 175 mm (7 in). The link slab was modeled for a distance of 600 mm (2 ft) at both adjacent ends of the open joint. The link slab length was based on the theoretical studies which showed that the load-deflection behavior of the structure would not be affected by a debonding length of up to 5% of the girder span length (Zia et al. [8]). The girders were restrained at supports and both extreme ends of the decks were restrained in x , y , and z directions (translations). The HL-93 loads were applied to the bridge models in such a way that they produced maximum negative moment and tensile force in the link slab.

3.2. Elements Used in Modeling. The FRP layers were meshed using SOLID46 element and material properties (Modulus of elasticity, Poisson's ratio, and density) were assigned during the process. The element edge length was 150 mm (6 in). A small size element was chosen because the depth of FRP was just 25 mm (1 in). The bridge decks and diaphragms were meshed using SOLID65 element and material properties (Modulus of elasticity, Poisson's ratio, and density) were assigned during the process. The element edge length of concrete element was 600 mm (24 in). The mesh was refined twice at the girder supports to restrain the girders properly over the piers (Saber et al. [9]).

3.3. Boundary Conditions and Loading System. In the model, the interface area between girders and substructure was restrained in the x and y directions (translations). Both extreme ends of the decks (area along the depth) were restrained in the x , y , and z directions (translations). LRFD Bridge Design [10] load combinations were considered, and the corresponding load factors were applied to the model. The vehicular live load and the live load surcharge were applied on the bridge. The truck load was applied to produce maximum negative moments in the link slab.

3.4. Comparison between Open Joint Bridge and Link Slab Bridge. The details for the finite element models are shown in Figure 9. The four girders in the first span of the bridge were designated as S1G1, S1G2, S1G3, and S1G4. Similarly, girders in the second span of the bridge were designated as S2G1, S2G2, S2G3, and S2G4 and girders in the third span of the bridge were designated as S3G1, S3G2, S3G3, and S3G4. Among all the girders, the maximum flexural stresses (tensile) were found in the second girder of the first span.

3.5. Girder Stresses

3.5.1. Span 1. The flexural stresses (tensile) for the bottom elements along the length of the second girder in the first span for the two bridge models were shown in Figure 10.

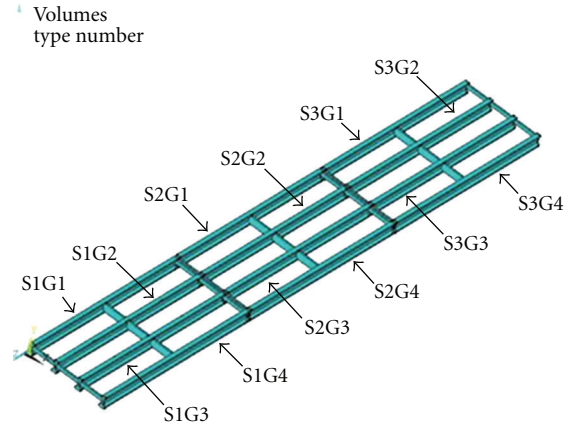


FIGURE 9: Model with the girders.

The flexural stresses were higher in the open joint bridge than those in the link slab bridge at most of the locations. A maximum flexural stress difference of 1 MPa (150 psi) was observed between the two girders, at a distance of 14.9 m (49 ft-8 in) from the left support. The flexural stresses were almost the same for a length of 6 m (20 ft) from the left support for both cases, but after that, the stresses in the open joint bridge were much higher. It can be inferred from the figure that the continuity in the decks reduces the flexural stresses in the girders.

3.5.2. Span 2. The flexural stresses (tensile) for the bottom elements along the length of the second girder in the second span for two bridge models were shown in Figure 11. The flexural stresses were higher in the open joint bridge than those in the link slab bridge at all locations. A maximum flexural stress difference of 0.28 MPa (40 psi) was observed between two girders, at a distance of 13.1 m (43 ft-9 in) from the left support.

3.5.3. Span 3. The flexural stresses (tensile) for the bottom elements along the length of the second girder in the third span for two bridge models were shown in Figure 12. A maximum flexural stress difference of 0.21 MPa (31 psi) was observed between two girders, at a distance of 3.7 m (12 ft-4 in) from the left support. The flexural stresses were higher in the open joint bridge up to 12 m (40 ft) from the left support and after that the flexural stresses were high in the link slab bridge.

3.6. Maximum Flexural Stresses in Girders. The maximum flexural stresses in the twelve girders of the open joint bridge, the link slab bridge, and the percentage change in stresses of the open joint bridge compared with link slab bridge were shown in Table 2. The stresses were higher in girders of the open joint bridge. The maximum decrease was 34% found in the girders of span 2 of the bridge, and the minimum decrease was 9% found in span 3. The maximum effects in span 1 where truck load was applied were in the range of 16% to 22%.

TABLE 4: Stresses in link slabs at the top and the bottom of bridge deck.

Results	Link slab 1 stress (MPa)		link slab 2 stress (MPa)	
	Max.	Min.	Max.	Min.
Transverse stress (S_x)	0.53	-0.09	0.23	-0.04
Longitudinal stress (S_z)	2.29	-1.01	1.05	-0.20
Shear stress (S_{yz})	0.05	-0.03	0.07	-0.01

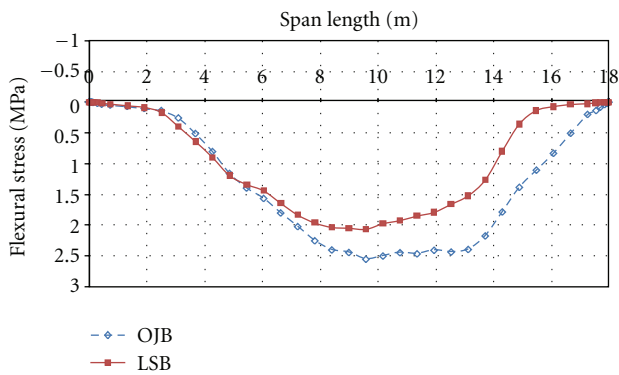


FIGURE 10: Flexural stresses for bottom elements of 2nd girder in 1st span (S1G2).

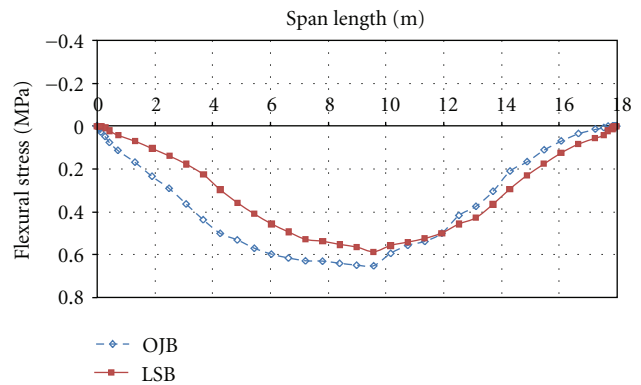


FIGURE 12: Flexural stresses for bottom elements of 2nd girder in 3rd span (S3G2).

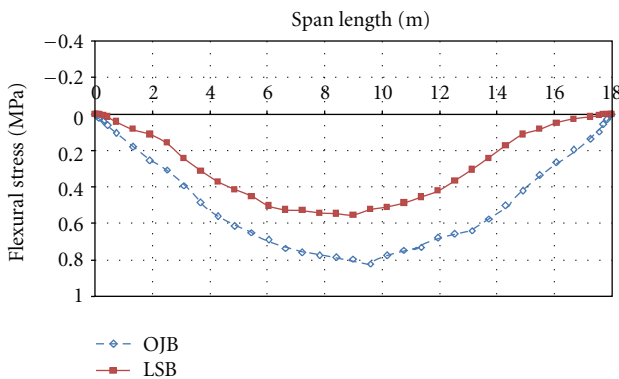


FIGURE 11: Flexural stresses for bottom elements of 2nd girder in 2nd span (S2G2).

3.7. *Stresses in Bridge Decks.* In bridge decks, the maximum and minimum transverse, longitudinal, and shear stresses were found in the first deck of the open joint bridge or the link slab bridge, since the load was applied on the first span of the bridge. The use of link slab reduced the bridge deck stresses. The transverse stresses were reduced by more than 13%, the longitudinal stresses were reduced by more than 36%, and the shear stresses were reduced by more than 43%. Based on these results, the use of the link slab will improve the performance of the bridge decks.

3.8. *Stresses in Link Slabs.* The maximum and minimum transverse, longitudinal, and shear stresses in two link slabs were shown in Table 3. Slabs 1 and 2 were joined by link slab 1, and slabs 2 and 3 were joined by link slab 2. The stresses were higher in link slab 1 than those in the link slab 2 because the truck was placed on the first span of the bridge. Maximum and minimum stresses were either at the top surface or at the bottom surface of the link slab.

The longitudinal stresses along the depth or thickness of the link slab 1 for the bottom element and at the top element were -1.01 MPa (-146.7 psi) and 2.29 MPa (332.8 psi), respectively. The longitudinal stresses along the depth for the bottom element and at the top element of the link slab 2 were -0.20 MPa (-28.4 psi) and 1.05 MPa (151.9 psi), respectively. The longitudinal stresses varied from compression to tension from the bottom to the top elements of both link slabs. The maximum longitudinal stresses along the length of the link slabs for the top elements were 1.21 MPa (176.1 psi) and 0.62 MPa (89.6 psi) for link slabs 1 and 2, respectively. Along the length of the link slab, all top elements for both link slabs were in tension. The maximum and minimum longitudinal stresses were higher in the link slab 1 than those in the link slab 2 because the truck load was placed in the first span of the bridge and the link slab 1 was connecting the span 1 and the span 2 decks of the bridge. The maximum longitudinal stresses along the length of the link slabs for the bottom elements were 0.29 MPa (-42.1 psi) and 0.02 MPa (2.6 psi) for link slabs 1 and 2,

respectively. Along the length of the link slab, the bottom elements of link slab 2 were in tension.

4. Conclusions

The ductility of the FRP grid material was utilized to accommodate bridge deck deformations imposed by girder deflection, concrete shrinkage, and temperature variations. It would also provide a cost-effective solution to a number of deterioration problems associated with bridge deck joints.

The structural behavior of two types of FRP-grid-reinforced concrete slabs was investigated. Scaled-up beam specimens simulating the actual deck joint were prepared and tested. The design concept of link slabs was then examined to form the basis of design for FRP grid link slabs. Improved design of FRP grid link slab/concrete deck slab interface was confirmed in the numerical analysis.

The results indicated that the technique would allow simultaneous achievement of structural need, lower flexural stiffness of the link slab approaching the behavior of a hinge, and durability need of the link slab. The overall investigation supports the contention that durable jointless concrete bridge decks may be designed and constructed with FRP grid link slabs. It is recommended that the link slab technique be used during new construction of bridge decks. Also, it is recommended that the advantages of using the FRP grid link slab technique in repair and retrofit of bridge decks are considered along with the amount of intrusive field work required to develop the required mechanical properties at the bridge deck joints. The Louisiana Transportation Research Center received funds from the federal highway administration through the Innovative Bridge Research and Development program to support the implementation of the use of FRP grid as link slab.

Acknowledgments

Support of this work was provided by Louisiana Transportation Research Center under research Project no. 06-2ST and State Project no. 736-99-1391. Also, the fiberglass grid used in this study was provided by the Fibergrate Composite Structures (<http://www.fibergrate.com/>). The contents of this study reflect the views of the authors who are responsible for the facts and the accuracy of the data presented herein. The contents do not necessarily reflect the official views or policies of the Louisiana Department of Transportation, or the Louisiana Transportation Research Center, or the Fibergrate Composite Structures. This paper does not constitute a standard, specification, or regulation.

References

- [1] A. Saber, F. Roberts, J. Toups, and W. Alaywan, "Effects of continuity diaphragm for skewed continuous span precast prestressed concrete girder bridges," *The Precast/Prestressed Concrete Institute Journal*, vol. 52, no. 2, pp. 108–114, 2007.
- [2] A. Saber, J. Toups, and W. Alaywan, "Effects of continuity on load transfer in prestressed concrete skewed bridges," in *Proceedings of the 3rd International Structural Engineering and Construction*, 2005.
- [3] A. Saber, "Failure Behavior of RC T-Beams retrofitted with Carbon FRP Sheets,' Creative Systems in Structural and Construction Engineering," in *Proceeding of the 1st International Structural Engineering and Construction*, Honolulu, Hawaii, USA, 2001.
- [4] K. P. Dutta, M. D. Bailey, R. J. Hayes, W. D. Jensen, and W. S. Tsai, "Composite grids for reinforcement of concrete structures," *Construction Productivity Advancement Research Program*, Final report, 1998.
- [5] American Concrete Institute, "Building Code Requirements for Structural Concrete," ACI 318-05.
- [6] American Concrete Institute, "Report on fiber reinforced plastic, reinforcement for concrete structure," ACI 440R, 2002.
- [7] A. Saber, J. Toups, and A. Tayebi, "Continuity diaphragms for aashto type II girders," in *Proceedings of the 2nd International Structural Engineering and Construction*, Rome, Italy, August 2003.
- [8] P. Zia, C. Alp., and K. E. S. Adel, *Jointless Bridge Decks*, North Carolina Department of Transportation, 1995.
- [9] A. Saber, F. Roberts, X. Zhou, and W. R. Alaywan, "Impact of higher truck loads on remaining safe life of Louisiana bridge decks," in *Proceedings of the 9th International Conference, Applications of Advanced Technology in Transportation*, Chicago, Ill, USA, August 2006.
- [10] American Association of State and Highway Transportation Officials, *LRFD Bridge Design Specifications*, U.S. Customary Units, 3rd edition, 2004.

Research Article

Pounding Effects in Simply Supported Bridges Accounting for Spatial Variability of Ground Motion: A Case Study

G. Tecchio, M. Grendene, and C. Modena

Department of Structural and Transportation Engineering, University of Padova, Via Marzolo 9, 35131 Padova, Italy

Correspondence should be addressed to G. Tecchio, teccio@dic.unipd.it

Received 2 January 2012; Accepted 24 March 2012

Academic Editor: Sami W. Tabsh

Copyright © 2012 G. Tecchio et al. This is an open access article distributed under the Creative Commons Attribution License, which permits unrestricted use, distribution, and reproduction in any medium, provided the original work is properly cited.

This study carries out a parametrical analysis of the seismic response to asynchronous earthquake ground motion of a long multispan rc bridge, the Fener bridge, located on a high seismicity area in the north-east of Italy. A parametrical analysis has been performed investigating the influence of the seismic input correlation level on the structural response: a series of nonlinear time history analyses have been executed, in which the variation of the frequency content in the accelerograms at the pier bases has been described by considering the power spectral density function (PSD) and the coherency function (CF). In order to include the effects due to the main nonlinear behaviours of the bridge components, a 3D finite element model has been developed, in which the pounding of decks at cap-beams, the friction of beams at bearings, and the hysteretic behaviour of piers have been accounted for. The sensitivity analysis has shown that the asynchronism of ground motion greatly influences pounding forces and deck-pier differential displacements, and these effects have to be accurately taken into account for the design and the vulnerability assessment of long multispan simply supported bridges.

1. Introduction

Earthquake ground motion is usually assumed as a spatially uniform dynamic input in seismic analysis; this assumption is correct for structures standing on a reasonably restricted area, in which the soil characteristics are presumed to be homogeneous and the seismic wave propagating velocity can be neglected, but becomes inadequate for spatial structures standing on large sites such as extended foundations or dams, and long-estending structures such as bridges, viaducts, tunnels, and pipelines. In these cases the spatial variability of ground motion should be considered to avoid gross evaluation errors or at least underestimation of the dynamic response, since the phenomenon affects the response considerably and, hence, the level of protection of these structures (Lupoi et al. [1]). In particular for long multispan simply supported bridges, a spatial variation in the input acting at supports (pier and abutment foundations) should be considered since it can induce pounding effects and deck unseating. It has been observed during the recent major seismic events that this kind of bridge structure very often experiences pounding phenomena between adjacent structural segments (between neighbouring decks or cap-beams and decks, with

a component of impact force transferred to the piers), which can amplify differential movements between adjacent spans and determine cracks or brittle fractures at beam endings. These amplified differential displacements can induce pull-off and drop collapses of spans when the displacement capacity of the bearing devices is exceeded or the seating length of girders is not sufficient for them to rest on their supports during strong ground motions.

For this type of bridges are required quite complex numerical models to represent with acceptable approximation the global structural response taking into account the incoherency of the seismic excitation at the supports, the impact phenomena between neighbouring structural segments, and the nonlinear behaviour of the substructural components (piers and decks).

In the present study, the acceleration and displacement time histories at the several prescribed locations on the ground surface corresponding to the bridge supports, are generated using the spectral representation method [2–4]. In order to generate the stochastic field, three basic components are required: (i) power spectral density (PSD) which gives the frequency content of the random process, (ii) coherency function (CF) which gives an analytical representation of

spatial variation of the ground motion in the frequency domain, and (iii) shape function (SF) for determining a nonstationary random process in the time domain. Some expressions have been proposed for the target spectral density (i.e., the Clough-Penzien form [5], and the expressions given by seismic codes [6]), for the coherency function [7–10] for the shape function [9]. The generated time histories are compatible with prescribed response spectra and duration of strong ground motions for the considered seismic area and reflect the wave passage and loss of coherence effects.

As regards evaluation of the pounding effects, it has to be said that the interest of researchers is quite recent; the problem was first investigated by [11] who studied the pounding phenomenon between two adjacent buildings, modelling the collision through impact elements which connected simple single-degree of freedom structures. In 1992 the same problem was examined also by [12]; in 1998 the study made by [11] was taken up again and applied to bridge structures in [13]. Further investigations were developed in [14] on the numerical simulation of the pounding process with the aim of calibrating the impact element between neighbouring structures by comparing the numerical results with the exact solution based on the wave propagation theory. In recent years more complex finite elements models have been developed: a numerical 3D simulation applied to a multispan simply supported bridge is described in [15].

From the aforementioned studies interesting conclusions can be drawn for an improved modelling of the pounding effect:

- (1) pounding between adjacent segments can be described with fair accuracy through an impact element characterised by stiffness and damping (which accounts for energy dissipation);
- (2) it has been noted in [13] that there is no need of modelling the entire structure for long bridges in order to assess the middle span response with fair accuracy; it is enough to study the seven central spans since there are no relevant differences in the numerical results between a model with an infinite number of span and a seven-span model;
- (3) in the finite element model the stiffness k_1 of the impact element should be calibrated considering the number n of finite elements which compose the deck ([14]);
- (4) it is important to define opportunely the time step used for the integration in the time-domain to avoid that colliding adjacent segments of neighbouring decks may behave like rigid bodies, since they influence the dynamic response with their axial deformation.

In the present study state-of-the-art models have been used to simulate the asynchronous ground motion as a multisupport seismic excitation and describe the pounding effects, as described in Section 2.



FIGURE 1: Fener bridge: (a) lateral view of the bridge on the Piave river.

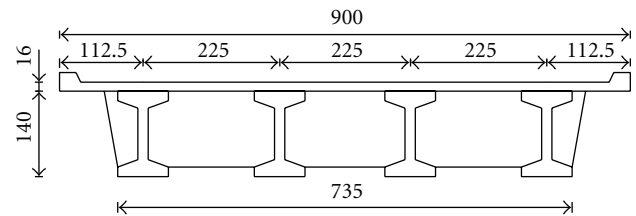


FIGURE 2: Typical transverse section of the superstructure.

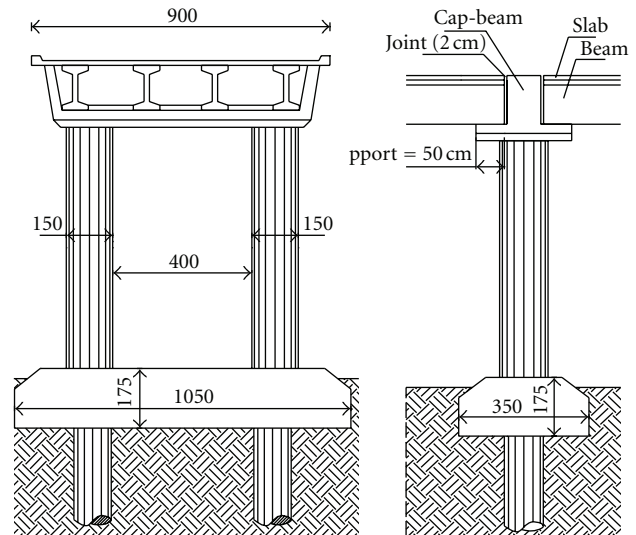


FIGURE 3: Pier elevation and longitudinal section.

2. Seismic Response Accounting for Spatial Variability of Ground Motion: A Sensitivity Analysis

2.1. The Fener Bridge. This study carries out a parametrical analysis of the seismic response to asynchronous earthquake ground motion of a long multispan rc bridge, the Fener bridge (see Figures 1, 2, 3 and 4), located in the Veneto region, in the Treviso province.

It represents an important overcrossing of the Piave river for the region road network. It was built in the mid nineteen seventies, and it consists of 24 regular spans having the same length of 24.75 m, except for the lateral spans near abutments, which are shorter (in particular at one end there

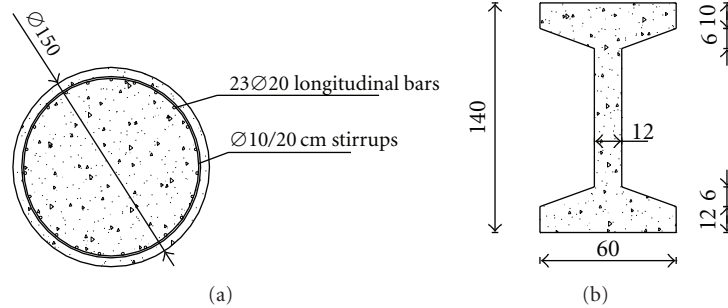


FIGURE 4: Cross sections of (a) typical column with reinforcement and (b) typical longitudinal precast concrete beam.

are two spans with reduced lengths of 18 m and 17.5 m, respectively, whilst at the other end only the last span has a slightly shorter length of 23.75 m). The overall structure is about 579 m long.

The deck lodging two lanes has an overall width of 9 metres; the deck structure is made up by four I-shaped precast beams with a constant height of 1.4 m and by a 16 cm high rc slab. The transverse distribution of traffic loads is obtained through 3 orthogonal rc girders positioned in the middle and at both ends of each span. Piers have a portal-shaped structure with circular rc columns, whose height varies gradually along the plan from a minimum of 5 to 8 m roughly, since the deck slope in the longitudinal direction is about 2%, while the extrados levels of plinths at the base remain constant. Piers raise on deep foundations as illustrated in Figure 3.

The pier section is shown in Figure 4(a): reinforcement for each of the two columns is provided by 23 longitudinal bars of 20 mm diameter and transverse stirrups of 10 mm diameter (pitch = 20 cm).

The materials used for piers can be classified as follows:

- (i) concrete: grade C25/30;
- (ii) reinforcing steel: smooth bars, characteristic yield stress $f_{yk} = 315$ MPa.

According to the national seismic zonation map, Fener bridge is located in an area characterised by $PGA = 0.25$ g, on a soil of medium stiffness (type B soil, according to the national zonation map [16]).

2.2. FE Model of the Multisupported Structure. In the numerical model of the bridge elements with linear and nonlinear behaviour have been adopted in order to represent effectively the global structural response: main beams, cap-beams, and transverse girders have been modelled with linear beam elements, the rc slab has been modelled with plate elements, whilst a nonlinear behaviour has been adopted for columns to simulate their hysteretic behaviour (using the Takeda-model [17] see Figure 5), for gap elements simulating impact between adjacent structural segments, and for frictional connections between longitudinal beams and cap-beams.

For the pier-element it has been necessary to assign in input a nonlinear force-displacement law, which has been

obtained through a push-over analysis both in the longitudinal direction, where the column has a cantilever deflection, and in the transverse direction where the piers behaviour is that of a portal frame. A lumped plasticity element has been employed for modelling the piers; the derived force-displacement curves are plotted below (see Figures 7 and 8).

Girders sit on cap-beams without any bearing devices therefore restraint of superstructure segments from longitudinal displacement is given only by friction; the force-displacement law for frictional bearings is assumed as an idealized rigid-plastic behaviour, with a friction coefficient taken as $\mu = 0.60$ in the analysis (see Figure 6). In the transverse direction a rigid restraint between deck and cap beam is assumed: the cap-beam lateral sides, being in direct contact with beams and acting as shear keys, do not allow any differential displacement.

Pier-deck pounding has been modelled through nonlinear gap elements which react only under compression, after the initial gap closure corresponding to the joint width (2 cm).

The gap element stiffness k_1 has been determined normalising to 1 parameter γ in the following expression [14]:

$$\gamma = \frac{k_1 L}{nEA}, \quad (1)$$

where A is the deck cross section, E its elastic modulus, L the span length, and n the number of finite elements into which the span length has been divided, taken as $n = 10$ in this study. In particular for the impact element a damping equivalent to energy dissipation has not been considered and a perfectly elastic collision has been modelled since impact energy dissipation does not influence the global structure response significantly [13].

As to external restraints, they have been considered fixed both in translation and rotation, because foundations are plinths on piles and in a first approximation the soil-structure interaction can be neglected. The superstructure segments not considered in the model (which represent a boundary condition to it) have been substituted with gap elements as illustrated in [13].

The FE model of the bridge and the related nonlinear dynamic analyses have been performed using *CSI SAP2000 release 9* software [18]. The model represents only the 7 central spans of the bridge (see Figure 9), with adequate

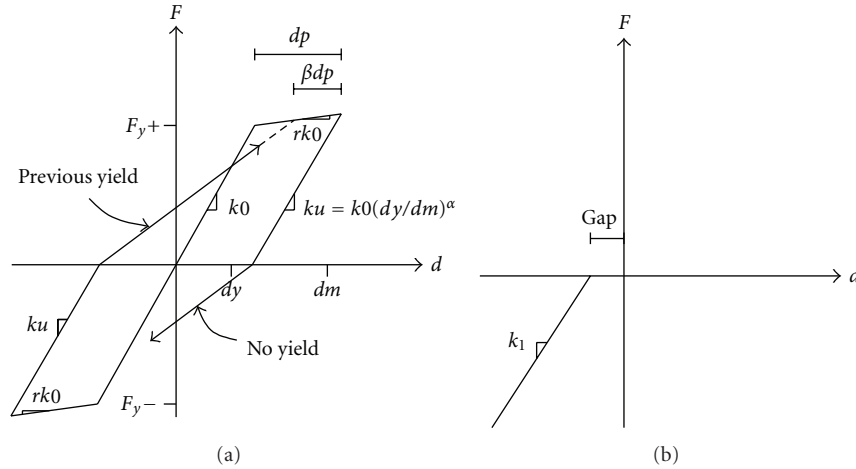


FIGURE 5: Models for (a) hysteretic behaviour of piers (Takeda model) and (b) gap element between adjacent structural segments.

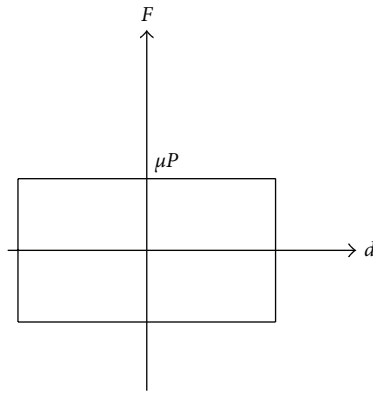


FIGURE 6: Connection between girder and cap-beam (frictional behaviour).

boundary conditions, instead of all the 24 spans; this has allowed to reduce substantially the computational effort due to the nonlinear effects included, without influencing the numerical accuracy of results because, as reported in [13], the seismic response of the central span in a model with a number of spans not less than five is a good approximation of the response obtained modelling the complete structure.

2.3. Characterisation of Spatial Variability. In the present study, the acceleration and displacement time histories at several prescribed locations on the ground surface corresponding to the bridge supports are generated using the spectral representation method. A uniform soil type is considered. As mentioned before, in order to generate the stochastic field, three basic components are required: (i) power spectral density function, (ii) coherency function, and (iii) shape function.

2.3.1. Power Spectral Density Function. Different analytical models for PSD are advanced by some authors; in this study the expressions given in EC8 [6] have been used, which are

approximate relations for power spectra corresponding to the site-dependent response spectrum proposed in the code. The expressions are derived as follows:

$$\begin{aligned} S_a &= 0.2\xi' A^2 T^{1.4} & \text{for } T < T_B, \\ S_a &= 6\xi' V^2 T^{-0.74} & \text{for } T_B < T < T_C, \\ S_a &= 300\xi' D^2 T^{-3.1} & \text{for } T > T_C, \end{aligned} \quad (2)$$

where S_a is the acceleration power spectrum, ξ' is the value of the damping ratio, A , V , and D are the values of spectral acceleration, velocity and displacement, and T_B and T_C are the response spectrum parameters.

2.3.2. Coherency Function. Assuming that the seismic wave field can be completely described by a single plane wave, its spatial variation can be quantified by means of the coherency function, which expresses the dependence in the frequency domain between the PSD of time histories ground motions occurring at two different stations k and l (with relative distance given by d_{kl}) [15]. It is generally defined as follows:

$$\gamma_{kl}(\omega) = \begin{cases} \frac{S_{kl}(\omega)}{\sqrt{S_{kk}(\omega) \cdot S_{ll}(\omega)}} & \text{for } S_{kk} \neq S_{ll}, \\ 0 & \text{for } S_{kk} \cdot S_{ll} = 0, \end{cases} \quad (3)$$

where ω is the circular frequency, $S_{kk}(\omega)$ and $S_{ll}(\omega)$ denote the autopower spectral density of the time histories at the stations k and l and $S_{kl}(\omega)$ is the cross-spectral density function of the considered pair of processes.

In general $\gamma_{kl}(\omega)$ is complex valued; its bounded modulus $0 \leq |\gamma_{kl}(\omega)| \leq 1$ measures the linear statistical dependence between the two time-histories: in particular $\gamma_{kl} = 1$ represents perfect correlation between the two motions, whereas $\gamma_{kl} = 0$ denotes complete lack of linear dependence, which means totally uncorrelated signals.

There are several models available in literature for the coherency function; in the present study the formulation

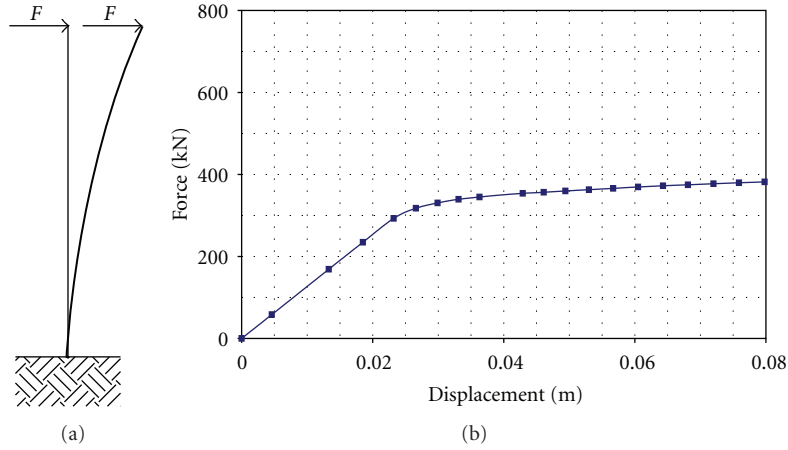


FIGURE 7: Piers behaviour in the longitudinal direction: (a) deflection shape; (b) force-displacement curve.

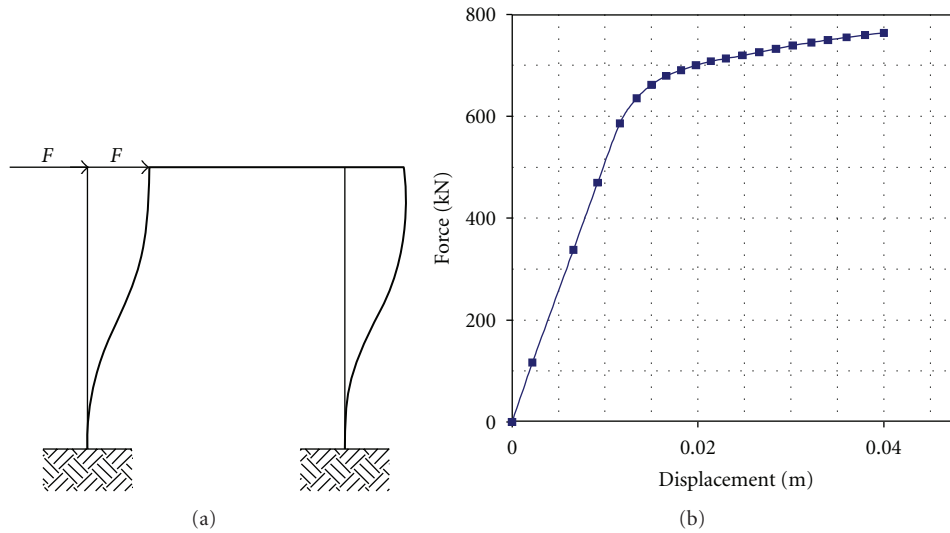


FIGURE 8: (a) Piers behaviour in the transverse direction: deflection shape; (b) force-displacement curve.

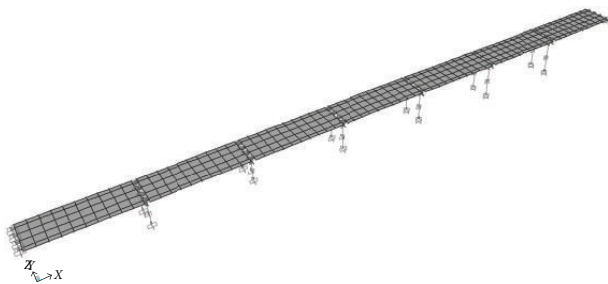


FIGURE 9: Three-dimensional FE model of the seven central spans.

given in [10] has been adopted (see Figure 10), and its general expression is

$$\gamma_{kl}(d_{kl}, \omega) = \exp\left\{-\left(\frac{\alpha \cdot \omega \cdot d_{kl}}{v_s}\right)^2\right\} \cdot \exp\left\{i\frac{\omega \cdot d_{kl}}{v_{app}}\right\}, \quad (4)$$

where the first term represents the geometrical incoherence, which arises from the scattering of waves in the heterogeneous soil medium, while the second term accounts for the

velocity of seismic waves and the difference in the times of arrival at different stations (wave-passage effect). The parameters describing these phenomena are, respectively (v_s/α) , in which v_s is the shear wave velocity in the medium, α a measure of loss of the coherency rate with distance and frequency, v_{app} , is the value of the apparent horizontal velocity of the surface wave. The relative distance between the two different stations k and l is given by the span length d_{kl} , while ω is the circular frequency. Both parameters (v_s/α) and v_{app} usually vary in the range $[300 \text{ m/s}, \infty]$; if $(v_s/\alpha) \rightarrow \infty$ and $v_{app} \rightarrow \infty$, the modulus of coherency function tends to be 1: the two signals are then totally correlated (identical and in-phase ground motions).

2.3.3. *Shape Function.* The shape function of the oscillatory process is defined in a general exponential form as suggested in [15]; it is the normalised envelope function of the time history and is governed by the parameters t_1 and t_2 which define the ramp duration and the decay starting time; t_{max}

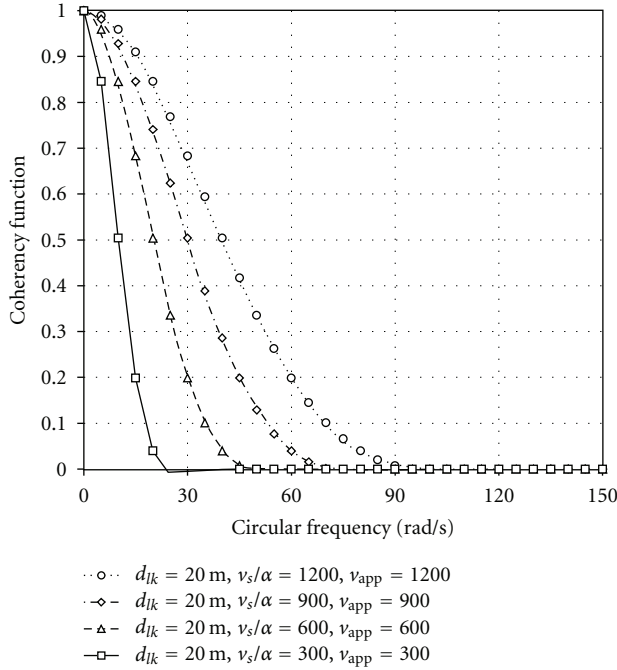


FIGURE 10: Coherency function modulus obtained for different correlation levels corresponding to a set of 4 values of parameters v_s/α e v_{app} (formulation by Luco and Wong).

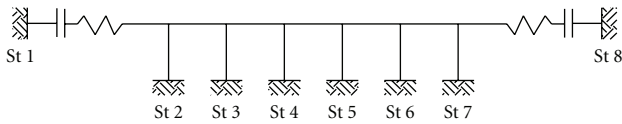


FIGURE 11: Ray of the 8 stations implemented in the FE model of the structure.

is the time history duration and $\nu = 0.2$ is the ratio of the amplitude envelope. The analytical formulation is as follows:

$$\xi(t) = \begin{cases} (t/t_1)^\eta, & t \leq t_1, \\ 1, & t_1 \leq t \leq t_2, \\ \exp\left\{\frac{t-t_2}{t_{\max}-t_2} \ln \nu\right\}, & t_2 \leq t \leq t_{\max}. \end{cases} \quad (5)$$

The parameters values in this work are taken as follows: $t_1 = 6$ sec, $t_2 = 16$ sec, $t_{\max} = 40$ sec, $\eta = 2.0$, and $\nu = 0.02$.

2.4. Generation of Compatible Time History Sets. In this study the formulation proposed in [6] for target spectral density function has been used to generate time history sets compatible with the response spectrum given by the code for a soil of medium stiffness with $PGA = 0,25$ g. The accelerograms, based on the coherency function previously described, have been generated trough the implementation of opportune algoritms [2]; the nonstationarity has been impressed to the stationary simulated motions by means of the shape function. In order to use the generated sets of response spectrum and coherency compatible time histories

as multisupport seismic inputs at the stations numbered from 1 to 8 (see Figure 11), the acceleration time histories have been doubly integrated to obtain the corresponding displacement time histories [15].

Different patterns of coherency have been selected in the parametric study, in order to represent the intermediate levels between the full correlation and the total uncorrelation of the time histories: 16 combinations of parameters v_s/α and v_{app} varying in the interval 300–1200 m/s have been considered (see Table 1), and for each combination five sets of generated time histories associated with a linear array of 8 stations (corresponding to locations of piers in the 7 central modelled spans of the bridge) have been applied, for a total of 80 sets examined.

A superimposition of the displacement time-histories generated in the simulation is reported as an example in Figure 12; the two extreme cases of strongly correlated ground motions ($v_s/\alpha = 1200$ m/s, $v_{app} = 1200$ m/s) and weakly correlated motions at supports ($v_s/\alpha = 300$ m/s, $v_{app} = 300$ m/s) are presented for the 8 stations considered in the analysis.

2.5. Analysis in the Time Domain. In order to determine the nonlinear response of the structure to a large set of earthquake ground excitations, it is necessary to use an efficient and not much time-consuming time-integration algorithm; in the present study the mode superimposition procedure based on load-dependent Ritz vectors [19] has been employed instead of direct integration methods in the time domain to reduce the computational effort and maintain an accurate solution. Further, the duration of the time step used for the integration has been limited by the follows condition:

$$\Delta t < T_1, \quad (6)$$

where T_1 is the expected impact duration. Thus it has been possible to capture in the model the effect that colliding adjacent segments of neighbouring decks produce by behaving not like rigid bodies, but influencing the dynamic response with their axial deformation [20]. The impact duration is calculated as follows:

$$T_1 = \frac{2L}{C_0}, \quad (7)$$

where L is the span length of the deck subjected to the pounding effect and C_0 is the propagation velocity of the impact wave travelling in a continuous medium, defined as follows:

$$C_0 = \sqrt{\frac{E}{\rho}}, \quad (8)$$

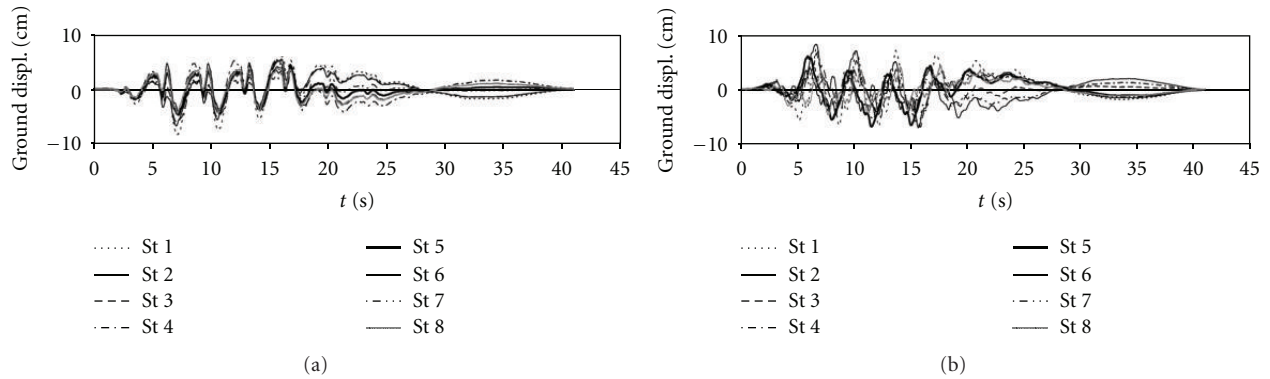
with E representing the elastic modulus of the superstructure and ρ its density

The values calculated for T_1 and the corresponding Δt adopted in this study are listed in Table 2.

It should be noticed that in fact a superstructure segment does not hit the neighbouring deck directly, due to the

TABLE 1: Combinations of v_s/α and v_{app} values considered in the parametric study.

Wave-passage effect	Geometrical incoherence			
	v_s/α (m/s)			
v_{app} (m/s)	300	600	900	1200
300	x	x	X	x
600	x	x	X	x
900	x	x	X	x
1200	x	x	X	x

FIGURE 12: Displacement time histories for stations 1 to 8: (a) highly correlated time-histories (set 1/5 $v_s/\alpha = 1200$ m/s).TABLE 2: Integration time step adopted Δt .

Elastic modulus E (MPa)	24821
Density ρ (Kg/m ³)	2500
Deck span length L (m)	24.75
Impact duration T_1 (s)	0.016
Integration time step Δt (s)	0.01
$\Delta t/T_1$	0.625

presence of the cap beam, but this element has been assumed as transmitting the impact rigidly and not influencing the wave propagation.

3. Results of the Numerical Analyses

A sensitivity analysis of the structure dynamic behaviour due to different spatially varying ground motion sets has been carried out, evaluating the influence of the seismic input correlation on the structural response, in terms of the following:

- (i) differential displacement between piers and deck segments;
- (ii) pounding forces between cap-beams and decks;
- (iii) effects on piers: shear forces at the bases and maximum displacements at the tops.

The response analysis focuses on the central span of the FE model, in order to provide results unaffected by the boundary conditions; as previously said, for each prefixed level of ground motion correlation (16 in total, each one determined by a couple of the parameters v_s/α and v_{app}) 5 nonlinear dynamic analyses have been performed, using

compatible time history sets. The mean value of the five results has been adopted.

3.1. Differential Displacements. Differential displacements between piers and decks are represented in Figure 13: it can be observed that in all cases the calculated values are relatively small and remain under the threshold of 5 cm; the maximum differential displacement ($d_d = 4.4$ cm) is obtained, as expected, for the extreme case of maximum coherency loss ($v_s/\alpha = 300$ m/s, $v_{app} = 300$ m/s).

The limited amplitude of differential displacements prevents pull-off-and-drop collapse of deck segments and can be explained considering that joint gaps at span ends are small (2 cm) and do not allow the development of high inertia forces at the deck level; consequently the displacements cannot be considerably amplified. These results are in accordance with the observations reported in [20].

3.2. Pounding Forces. Impact forces between cap beams and decks are highly influenced by the correlation level of ground motions at the structural supports: as Figure 14(a) shows, there is a trend in pounding forces, which rapidly increase with the loss of coherency of seismic inputs: the magnitude of impact force F_I , obtained in the extreme case of weakly correlated time histories ($v_s/\alpha = 300$ m/s, $v_{app} = 300$ m/s), assumes a value 3 times larger ($F_I = 1293$ kN) than that derived by analysis with uniform inputs, $F_I = 428$ kN (represented by the case $v_s/\alpha = 1200$ m/s, $v_{app} = 1200$ m/s). Consequently, even though in the case of uniform seismic excitation no damage should occur to the cap beams and decks, with weakly correlated input time histories, the pounding effects could determine considerable damage to the local area of bridge decks.

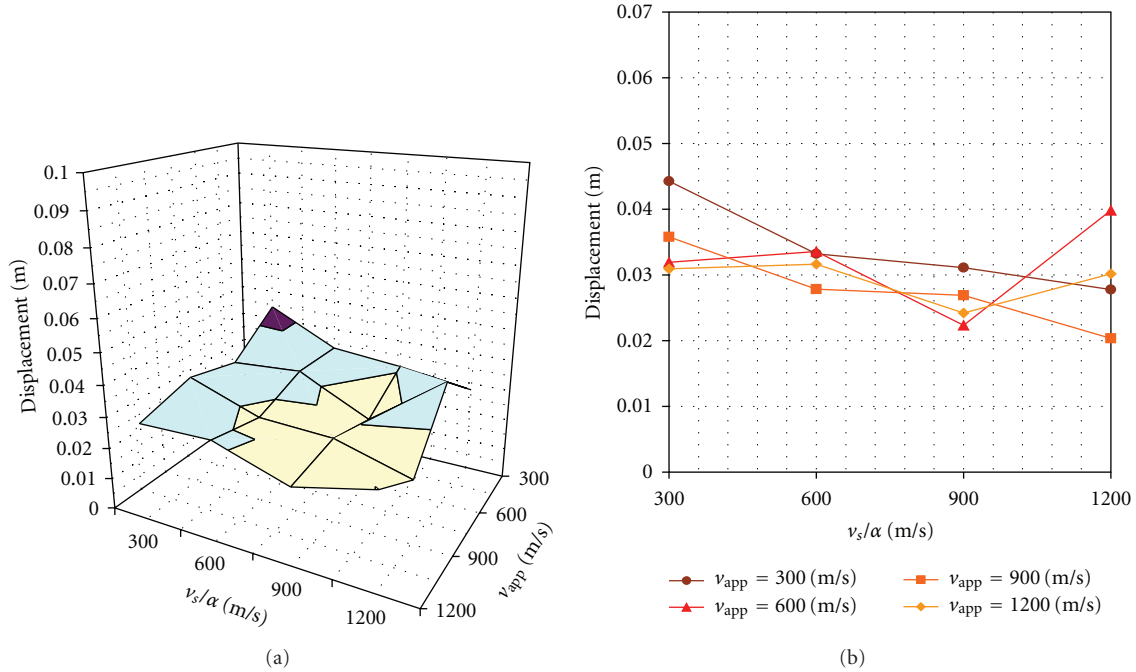


FIGURE 13: Pier-deck differential displacement varying with seismic input correlation level (represented by parameters v_s/α and v_{app}): (a) 3D view and (b) 2D view.

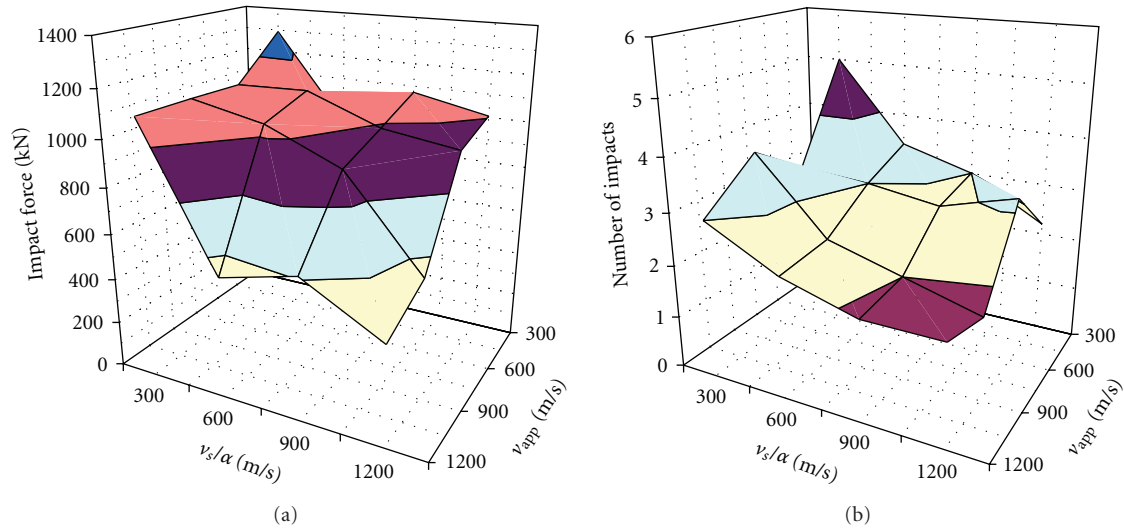


FIGURE 14: (a) Pounding forces varying with correlation level of input ground motions; (b) Total number of registered impacts (mean value).

Registered impacts follow a similar tendency (see Figure 14(b)): the numerical results show that collisions occur more frequently as the correlation level of time history inputs decreases. However in all cases, the total number of impacts (mean value of the 5 non linear dynamic analysis performed) is found to be relatively small (less than 5).

3.3. *Effects on Piers.* As regards the effects on piers in the longitudinal direction, they are represented in Figure 15 in terms of shear forces and displacements (maximum values at the top of the pier) obtained as functions of the correlation

level between the time histories. It can be observed that the maximum value of shear force $V = 346$ kN is obtained in the case of highly correlated time histories, and the minimum $V = 274$ kN is derived using inputs with the weakest correlation ($v_s/\alpha = 300$ m/s, $v_{app} = 300$ m/s). Similarly it can be said that there is a general trend for displacements at the pier top (see Figure 15(b)) that become larger as the correlation increases, with the maximum value $D = 3,7$ cm calculated in the case of the highest correlation level of input ground motions.

These effects can be explained considering that when ground excitations are weakly correlated or uncorrelated, the movement of deck segments can be in opposite direction

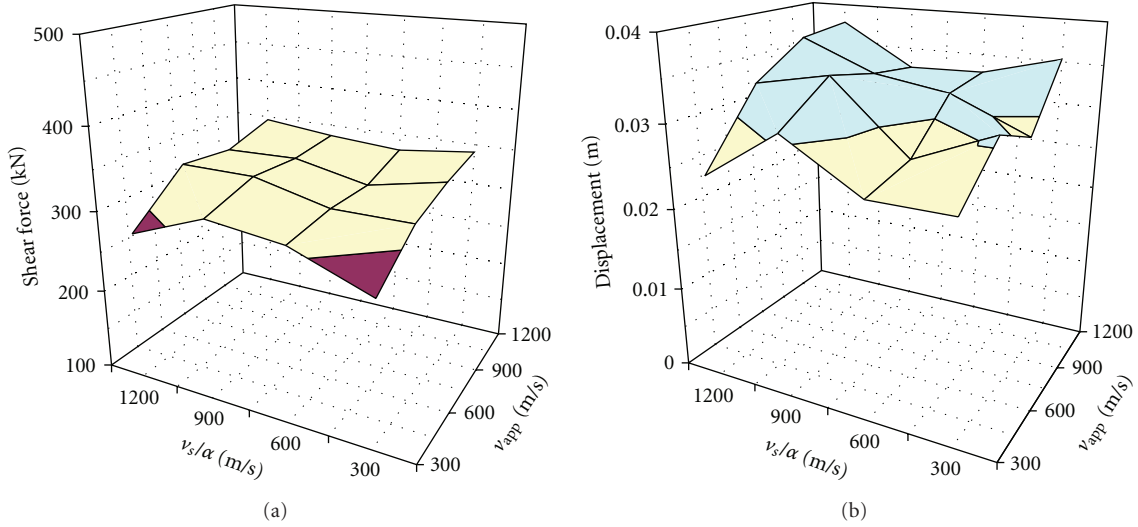


FIGURE 15: Longitudinal direction: (a) shear forces at the pier base: maximum values obtained for each correlation level of input ground motions; (b) maxima values of displacement at pier top.

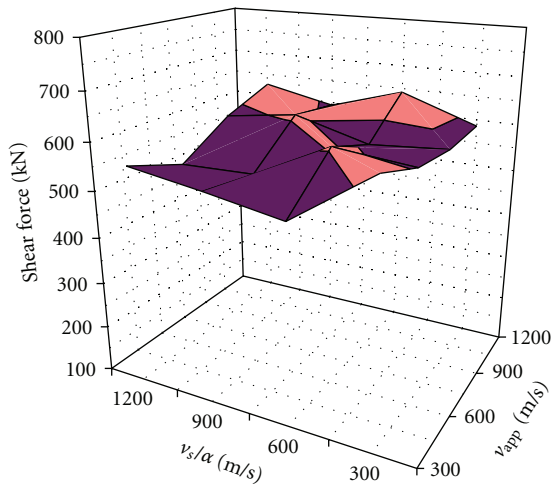


FIGURE 16: Transverse direction: maximum shear forces.

due to out-of-phase vibrations, and this fact determines collisions that reduce displacements at the top of the pier (and consequently the shear and bending moment at the base induced by the deformation of the pier itself). When the ground excitation is highly correlated, the responses of the bridge spans are in phase, the inertial forces at the pier tops are maximised, and in consequence displacements at the top and shear forces increase.

Regarding the response in the transverse direction, it should be noted that structural behaviour is not clearly affected by seismic input correlation (see Figure 16); one can observe that there is a slight tendency for shear forces at the pier base to increase with higher correlation levels, but the values are weakly affected by impacts between deck segments. This is consistent with the results presented in [19].

4. Conclusions

A parametrical analysis has been performed with the aim of investigating the influence of the seismic input correlation level on the structural response of a long multispan girder bridge. A series of nonlinear time history analyses have been performed, in which the main nonlinear behaviours of the bridge components, have been included: (i) the pounding of decks at cap-beams, (ii) the friction of beams at bearings, and (iii) the hysteretic behaviour of piers. The following conclusions can be drawn:

- (i) differential displacements between decks and pier-tops are affected by input correlation level but remain within a limited range (under the threshold of 5 cm) with the maximum value obtained for the extreme case of maximum coherency loss. The fact that they are relatively small prevents decks from unseating and can be explained by the limited width of the bridge joints;
- (ii) asynchronous ground motion influences greatly the pounding forces between decks and pier-tops, which can assume values 3 times larger than those calculated by an analysis with uniform input (represented by the case with the highest correlation level between the time-histories). The amplified pounding effects might determine considerable damage to the local area of bridge decks;
- (iii) as regards the effects on piers, it can be observed that in the longitudinal direction there is a general trend for displacements and shear forces, which increase with higher correlation levels of input ground motions. In the transverse direction the seismic response is not clearly influenced by the correlation level of ground excitations.

The results highlight that the spatial variation properties of the earthquake ground motion can significantly change the structural response especially in terms of pounding forces and deck unseating, and consequently these effects have to be taken into account for the design or the vulnerability assessment of long multispan simply supported bridges.

References

- [1] A. Lupoi, P. Franchin, P. E. Pinto, and G. Monti, "Seismic design of bridges accounting for spatial variability of ground motion," *Earthquake Engineering and Structural Dynamics*, vol. 34, no. 4-5, pp. 327–348, 2005.
- [2] G. Deodatis, "Non-stationary stochastic vector processes: seismic ground motion applications," *Probabilistic Engineering Mechanics*, vol. 11, no. 3, pp. 149–167, 1996.
- [3] M. Shinozuka and G. I. Schueller, "Stochastic fields and their digital simulation," in *Stochastic Methods in Structural Dynamics*, G. I. Schueller and M. Shinozuka, Eds., pp. 93–133, Martinus Nijhoff, Dordrecht, The Netherlands, 1987.
- [4] M. Shinozuka and G. Deodatis, "Simulation of multi-dimensional Gaussian stochastic fields by spectral representation," *Applied Mechanics Reviews*, vol. 44, no. 4, pp. 191–204, 1991.
- [5] R. W. Clough and J. Penzien, *Dynamics of Structures*, McGraw Hill, New York, NY, USA, 1993, International Edition.
- [6] UNI ENV 1998-2, "Eurocode 8—design provisions for earthquake resistance of structures—part 2," Bridges, 1998.
- [7] A. Der Kiureghian, "A coherency model for spatially varying ground motions," *Earthquake Engineering and Structural Dynamics*, vol. 25, no. 1, pp. 99–111, 1996.
- [8] H. Hao, C. S. Oliveira, and J. Penzien, "Multiple-station ground motion processing and simulation based on smart-1 array data," *Nuclear Engineering and Design*, vol. 111, no. 3, pp. 293–310, 1989.
- [9] R. S. Harichandran and E. H. Vanmarcke, "Stochastic variation of earthquake ground motion in space and time," *ASCE Journal of Engineering Mechanics*, vol. 112, no. 2, pp. 154–174, 1986.
- [10] J. E. Luco and H. L. Wong, "Response of a rigid foundation to a spatially random ground motion," *Earthquake Engineering and Structural Dynamics*, vol. 14, no. 6, pp. 891–908, 1986.
- [11] S. A. Anagnostopoulos, "Pounding of buildings in series during earthquakes," *Earthquake Engineering and Structural Dynamics*, vol. 16, no. 3, pp. 443–456, 1988.
- [12] B. F. Maison and K. Kasai, "Dynamics of pounding when two buildings collide," *Earthquake Engineering and Structural Dynamics*, vol. 21, no. 9, pp. 771–786, 1992.
- [13] R. Jankowski, K. Wilde, and Y. Fujino, "Pounding of superstructure segments in isolated elevated bridge during earthquakes," *Earthquake Engineering and Structural Dynamics*, vol. 27, no. 5, pp. 487–502, 1998.
- [14] K. Kawashima and Watanabe G., "Numerical simulation of pounding of bridge decks," in *Proceedings of the 13th World Conference on Earthquake Engineering Vancouver*, British Columbia, Canada, August 2004, Paper no.884.
- [15] G. Zanardo, H. Hao, and C. Modena, "Seismic response of multi-span simply supported bridges to a spatially varying earthquake ground motion," *Earthquake Engineering and Structural Dynamics*, vol. 31, no. 6, pp. 1325–1345, 2002.
- [16] Ordinance of the Presidency of the Council of Ministers 3431, "Initial elements on the general criteria for classifying national seismic zones and technical standards for construction," *Official Gazette of the Italian Republic*, 2003.
- [17] T. Takeda, A. M. Sozen, and N. N. Nielsen, "Reinforced concrete response to simulate earthquakes," *ASCE Journal of Structural Engineering Division*, vol. 96, no. 12, pp. 2257–2273, 1970.
- [18] Computers & Structures Inc., "CSI SAP2000 release 9," Berkeley Calif, USA, 2004.
- [19] E. L. Wilson, M. W. Yuan, and J. M. Dickens, "Dynamic Analysis by direct superposition of Ritz vectors," *Earthquake Engineering and Structural Dynamics*, vol. 10, no. 6, pp. 813–821, 1982.
- [20] R. Jankowski, K. Wilde, and Y. Fujino, "Reduction of effects in elevated bridges during earthquakes," *Earthquake Engineering & Structural Dynamics*, vol. 29, pp. 195–212, 2000.

Research Article

Simple Program to Investigate Hysteresis Damping Effect of Cross-Ties on Cables Vibration of Cable-Stayed Bridges

Panagis G. Papadopoulos, Andreas Diamantopoulos, Haris Xenidis, and Panos Lazaridis

Department of Civil Engineering, Aristotle University of Thessaloniki, 54124 Thessaloniki, Greece

Correspondence should be addressed to Panagis G. Papadopoulos, panaggpapad@yahoo.gr

Received 11 October 2011; Revised 21 March 2012; Accepted 24 March 2012

Academic Editor: Husam Najm

Copyright © 2012 Panagis G. Papadopoulos et al. This is an open access article distributed under the Creative Commons Attribution License, which permits unrestricted use, distribution, and reproduction in any medium, provided the original work is properly cited.

A short computer program, fully documented, is presented, for the step-by-step dynamic analysis of isolated cables or couples of parallel cables of a cable-stayed bridge, connected to each other and possibly with the deck of the bridge, by very thin pretensioned wires (cross-ties) and subjected to variation of their axial forces due to traffic or to successive pulses of a wind drag force. A simplified SDOF model, approximating the fundamental vibration mode, is adopted for every individual cable. The geometric nonlinearity of the cables is taken into account by their geometric stiffness, whereas the material nonlinearities of the cross-ties include compressive loosening, tensile yielding, and hysteresis stress-strain loops. Seven numerical experiments are performed. Based on them, it is observed that if two interconnected parallel cables have different dynamic characteristics, for example different lengths, thus different masses, weights, and geometric stiffnesses, too, or if one of them has a small additional mass, then a single pretensioned very thin wire, connecting them to each other and possibly with the deck of the bridge, proves effective in suppressing, by its hysteresis damping, the vibrations of the cables.

1. Introduction

The pretensioned cables in a typical cable-stayed bridge of medium size [1], as they are very long with a length of magnitude order 100 m, and a pretension axial force of magnitude order 1000 kN, exhibit, perpendicularly to their axis, a very small geometric stiffness, corresponding to their fundamental vibration mode, of a magnitude order only 50 kN/m. Also perpendicularly to their axis, they exhibit a very small intrinsic damping, due to their material internal friction. For the previous reasons, they are often subjected to large amplitude vibrations. And, if the external excitation is approximately periodic, with a period close to a natural period of the cable, for example, the fundamental one, then resonance may happen, and vibration amplitudes increase excessively and are maintained, with no significant reduction for a long time, unless special measures are taken.

Two usual reasons for the previous cable vibrations of cable-stayed bridges are the following.

- (1) A pretensioned cable exhibits a sag under its self-weight. Because of traffic, the ends of the cable,

on pylon and deck, are subject to a variation of their displacements; thus the elongation and axial force of the cable vary, which implies variation of its geometric stiffness, too, as well as variation of the sag of the cable. This vibration, due to variation of geometric stiffness, is called parametric excitation.

- (2) The successive pulses of a wind pressure exert a drag force, perpendicularly to the vertical plane of cables, at one side of the bridge. The variation of this drag force causes vibration of the cables.

In [2], a complete description of the problem of cable vibrations of cable-stayed bridges is presented, as well as a state of the art of various types of dampers for cable vibrations (viscous dampers, cross-ties, and others), along with case studies of dampers on real bridges.

The viscous dampers, although widely mentioned in literature, present some problems: usually, they are installed at the ends of a cable, where they are not very helpful; it seems that their main role is a slight reduction of cable's length, thus a slight increase of its geometric stiffness. Rarely, they

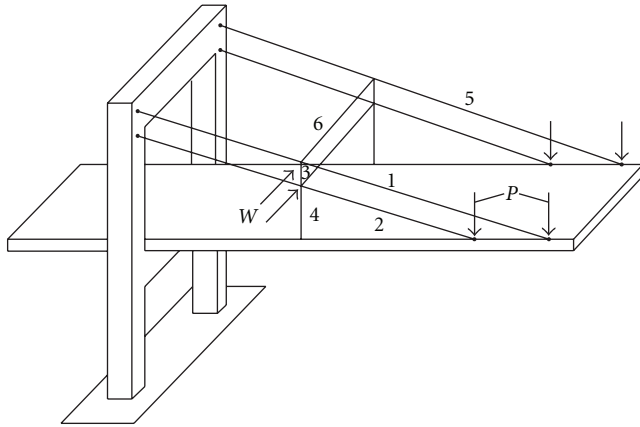


FIGURE 1: Part of a typical cable-stayed bridge [1].

are installed at intermediate points of a cable, where they are more helpful; however, this installation is difficult.

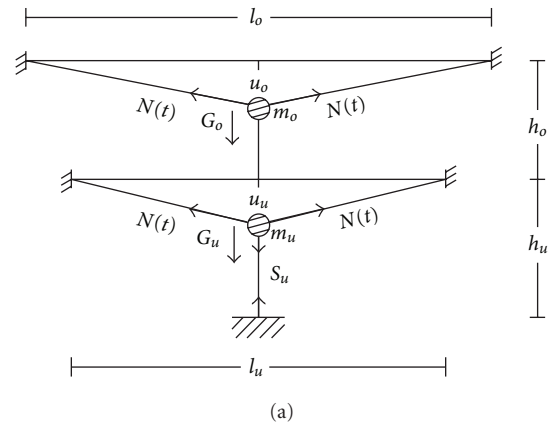
On the other hand, the cross-ties are preferable, for the following reasons: they are light and cheap, they are easily installed and pretensioned, and they easily replaced when damaged. And a great advantage of them is that although they are very thin, with a ratio of cross-section area of the cable to that of the cross-tie of a magnitude order 1000, however, the axial elastic stiffness, of a single pretensioned cross-tie, is comparable in magnitude with the geometric stiffness of a cable, that is of magnitude order 50 kN/m, along the same direction, perpendicularly to cable axis. Also, as the cross-ties are very thin, they are almost invisible, so they do not harm the aesthetics of the bridge.

For the previous reasons, recently many researchers recommend the use of cross-ties to suppress large amplitude cable variations of cable-stayed bridges. In [3–6], analytical studies are performed on cross-ties or hybrid systems consisting of viscous dampers and cross-ties.

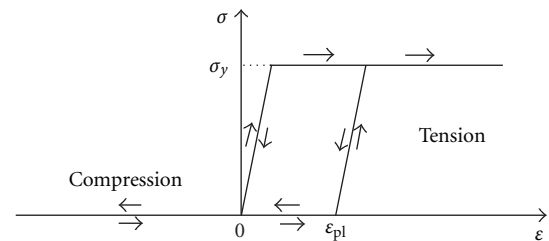
Here, a simplified analytical method is proposed [7], in order to investigate the hysteresis damping effect of cross-ties, where, for every individual cable, an SDOF model is adopted, approximating its fundamental vibration mode. The geometric nonlinearity of the cables is taken into account by their geometric stiffness. At same time, the proposed method is accurate, as it includes the material nonlinearities of the cross-ties, by their compressive loosening, tensile yielding, as well as hysteresis stress-strain loops.

A short computer program (only about 120 Fortran instructions), fully documented, is presented for the step-by-step dynamic analysis [9] of isolated cables or couples of parallel cables, connected to each other and possibly with the deck of the bridge, by very thin pretensioned wires (cross-ties) and subjected to variation of the axial forces of cables due to traffic [8] or to successive pulses of wind drag force.

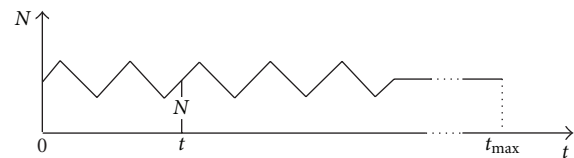
Seven numerical experiments are performed. And, based on them, observations are made on the effectiveness of a single pretensioned very thin wire, connecting a couple of cables of a cable-stayed bridge, in suppressing, by its hysteresis damping, their large amplitude vibrations.



(a)



(b)



(c)

FIGURE 2: (a) Geometric, static, and dynamic parameters of a cable structure. (b) Primary σ - ϵ diagram describing the nonlinear axial stress-strain law of a cross-tie. (c) Given time-history of axial forces of cables.

2. Equations of the Problem

Figure 1 shows a part of a typical cable-stayed bridge [1], with a pylon consisting of two vertical legs, which are connected by two transverse beams, a part of the deck with a slender rectangular plate section, two couples of pretensioned parallel inclined cables at each side of the bridge, connected by their ends to the pylon and the deck and two pretensioned very thin vertical in-plane cross-ties, at two sides of bridge, which intend to suppress parametric vibration of cables due to traffic loads P , as well as two out-of-plane horizontal cross-ties, which intend to suppress cable vibrations due to wind forces W .

In the following, the equations of nonlinear dynamic analysis will be written, for a specific cable structure consisting of two parallel pretensioned cables (1 and 2 in Figure 1), connected by two very thin pretensioned cross-ties (3 and 4 in Figure 1) to each other and with the deck of the bridge and subjected to parametric vibration, due to traffic. In subsequent applications, by simple and obvious modifications of these equations, other cable structures

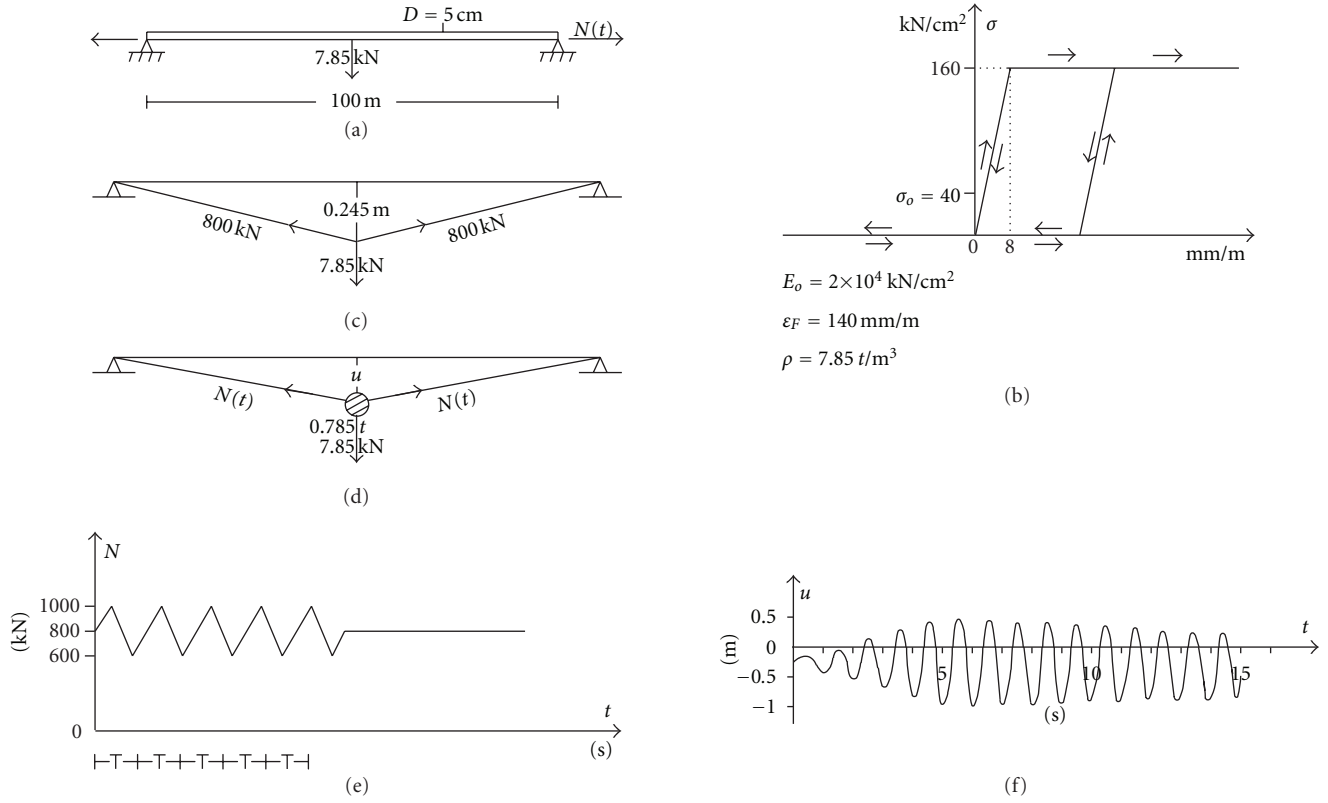


FIGURE 3: First application: isolated cable subject to traffic. (a) Given geometry and loading. (b) Axial stress-strain diagram of high-strength steel. (c) Initial static analysis. (d) Parameters of dynamic analysis. (e) Given time-history $N(t)$ of axial force of cable. (f) Resulting time-history $u(t)$ of vertical displacement at center of cable.

(combinations of main cables and cross-ties) subjected to traffic or wind excitation will be treated, too.

In the following analysis, the inclination of the cables will be ignored for the sake of simplicity. So, in Figure 2(a), the couple of horizontal parallel pretensioned main cables represents the inclined cables 1 and 2 of Figure 1, whereas the very thin pretensioned vertical wires represent the in-plane cross-ties 3 and 4 of Figure 1.

2.1. Geometric Equations. For every individual cable, a simplified SDOF model is adopted, which approximates its fundamental vibration mode. This unique DOF, for every cable, is the displacement of its center perpendicularly to its axis, that is, the vertical displacements downwards u_o and u_u in Figure 2(a), for the upper and lower cables, respectively. The geometric equations, relating the displacements of cables with the elongations and strains of cross-ties, are the following, according to Figure 2(a):

$$\begin{aligned} \Delta h_o &= h_o - u_o + u_u - h_{o\varphi}, \\ \Delta h_u &= h_u - u_u - h_{u\varphi}, \end{aligned} \quad (1)$$

where Δh_o and Δh_u are elongations of upper and lower cross-ties, respectively, h_o and h_u their design (nominal) lengths, and $h_{o\varphi}$ and $h_{u\varphi}$ are their initial undeformed lengths. And the

strains ε_o and ε_u of upper and lower cross-ties, respectively, are

$$\begin{aligned} \varepsilon_o &= \frac{\Delta h_o}{h_{o\varphi}}, \\ \varepsilon_u &= \frac{\Delta h_u}{h_{u\varphi}}. \end{aligned} \quad (2)$$

2.2. Constitutive Equations. Figure 2(b) is the primary stress-strain diagram, which describes the axial nonlinear stress-strain law of a cross-tie, made of the same high-strength steel as the main cables. This σ - ε law includes compressive loosening, tensile yielding, as well as hysteresis stress-strain loops, resulting from the obvious in loading-unloading rule Figure 2(b). There is only one constitutive variable, the plastic strain ε_{pl} of the cross-tie. The present stress σ is an obvious function of present strain ε and present value of plastic strain ε_{pl} :

$$\sigma = \sigma(\varepsilon, \varepsilon_{pl}), \quad (3a)$$

whereas the variation of plastic strain $\Delta\varepsilon_{pl}$ can be expressed as a function of present strain ε , variation of present strain $\Delta\varepsilon$, as well as present value of plastic strain ε_{pl} , in an

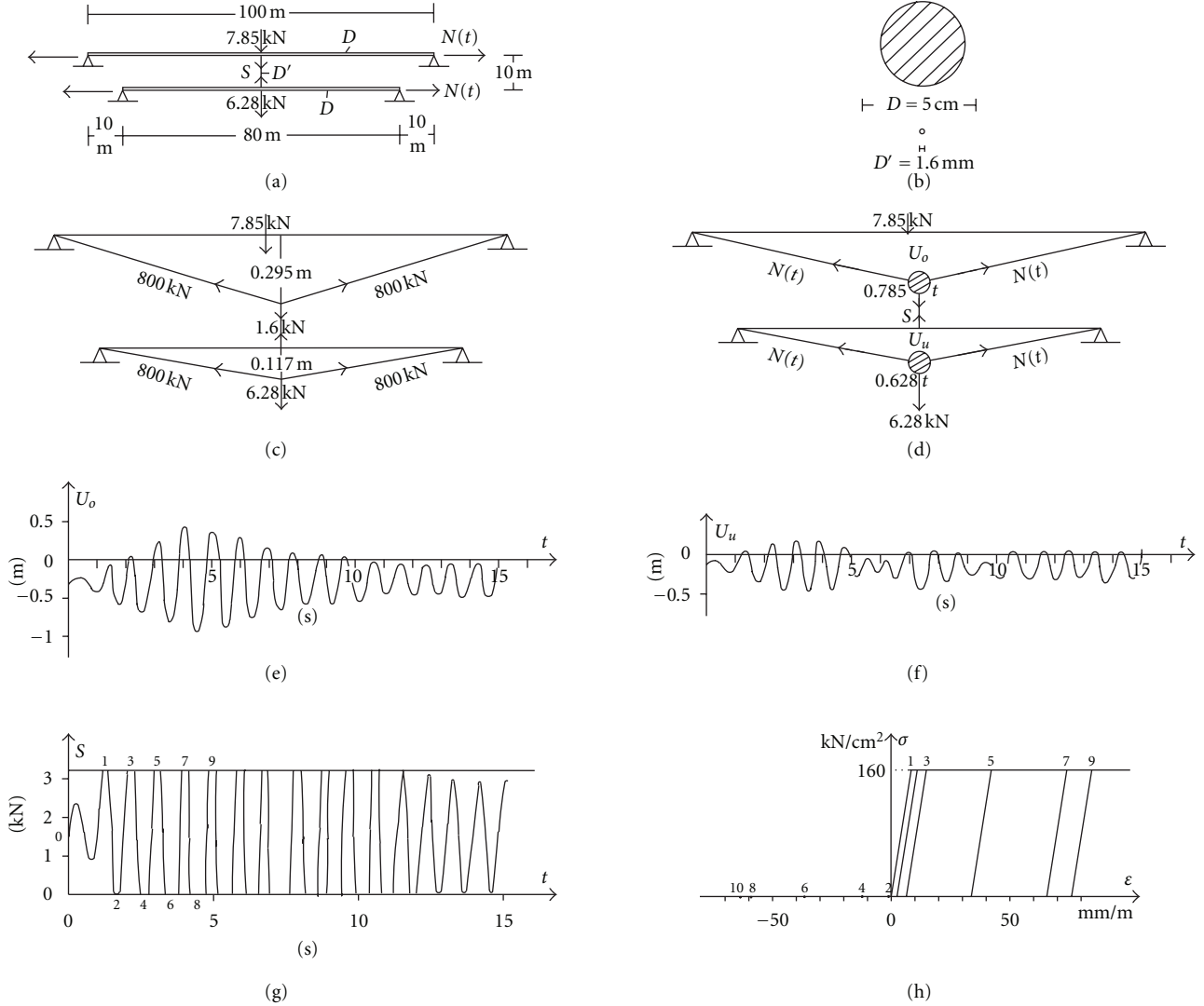


FIGURE 4: Second application: couple of interconnected cables, subject to traffic. (a) Given geometry and loading. (b) Crosssections of main cables and cross-tie. (c) Initial static analysis. (d) Parameters of dynamic analysis. (e), (f) Resulting time-histories of vertical displacements of centers of upper and lower cables. (g) Resulting time-history of axial force of cross-tie. (h) Resulting hysteresis stress-strain loops of the cross-tie.

obvious manner by the loading-unloading-reloading rule of Figure 2(b):

$$\Delta \varepsilon_{pl} = \Delta \varepsilon_{pl}(\varepsilon, \Delta \varepsilon, \varepsilon_{pl}). \quad (3b)$$

2.3. *Static Equations.* The axial forces of the cross-ties are

$$\begin{aligned} S_o &= \sigma_o A_w, \\ S_u &= \sigma_u A_w, \end{aligned} \quad (4)$$

for the upper and lower ties, respectively, where A_w is the cross-section area of the very thin wires (cross-ties), whereas the vertical nodal forces applied at the centers of the

cables, upper and lower one, respectively, are, according to Figure 2(a)

$$\begin{aligned} F_o &= G_o - K_{Go} u_o + S_o, \\ F_u &= G_u - K_{Gu} u_u - S_o + S_u, \end{aligned} \quad (5)$$

where the downwards direction has been taken as positive, G_o and G_u are weights at centers of upper and lower cables, respectively, and

$$\begin{aligned} K_{Go} &= 2 \frac{N(t)}{l_o/2}, \\ K_{Gu} &= 2 \frac{N(t)}{l_u/2} \end{aligned} \quad (6)$$

are their geometric stiffnesses, where $N(t)$ is the given time-history of the axial forces of the cables.

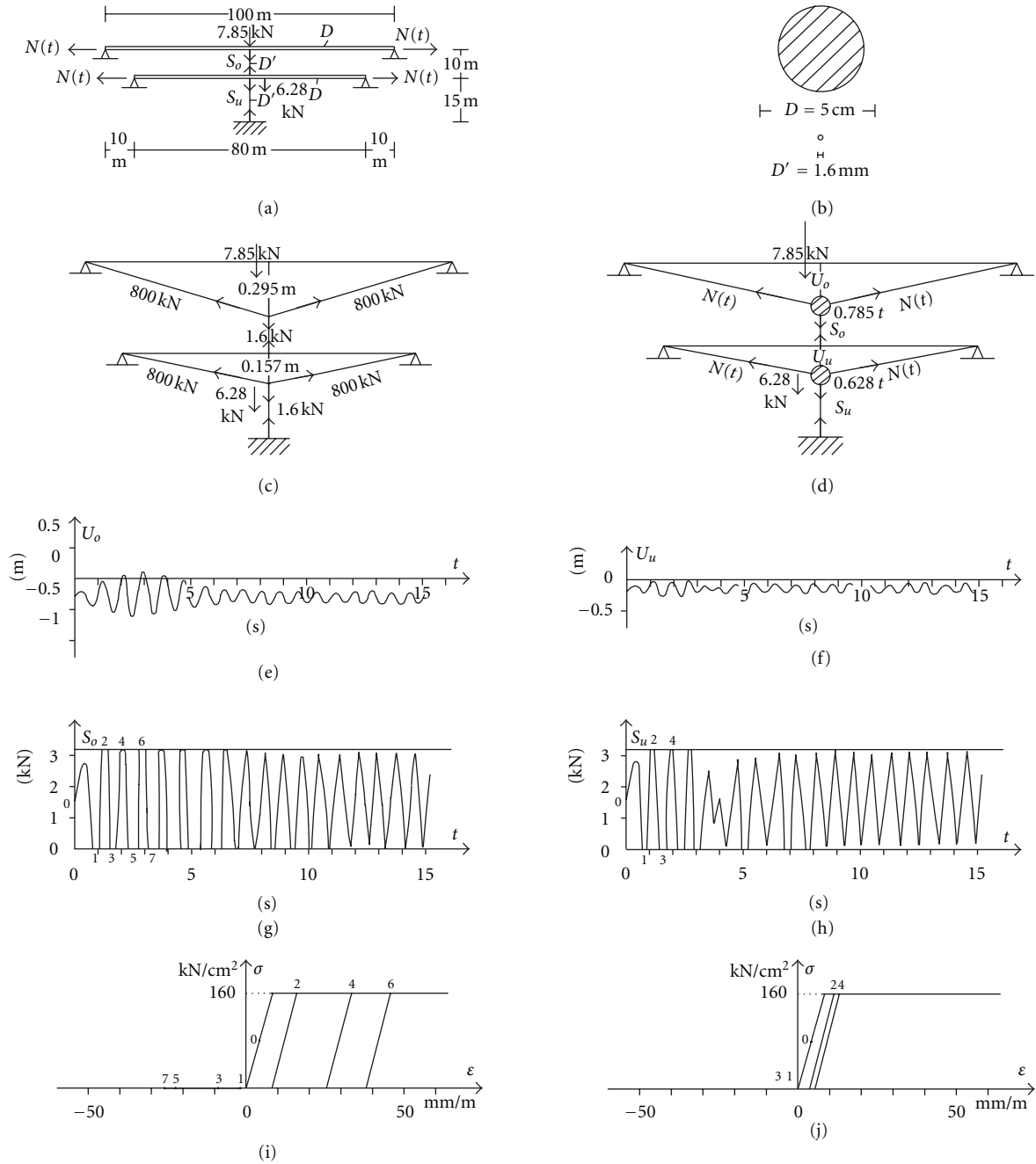


FIGURE 5: Third application: couple of cables, connected to each other and to deck, subject to traffic. (a) Given geometry and loading. (b) Cross sections of main cables and cross-ties. c. Initial static analysis. (d) Parameters of dynamic analysis. (e), (f) Resulting time-histories of displacements of upper and lower cables. (g), (h) Resulting time-histories of axial forces of upper and lower cross-tie. (i), (j) Resulting hysteresis stress-strain loops of upper and lower cross-ties.

2.4. *Dynamic Equations.* Damping is ignored, as the material internal friction of the cables is meaningless. The vertical accelerations at the centers of upper and lower cable are

$$\begin{aligned} \ddot{u}_o &= \frac{F_o}{m_o}, \\ \ddot{u}_u &= \frac{F_u}{m_u}, \end{aligned} \tag{7}$$

where m_o and m_u are lumped masses at centers of cables (Figure 2(a)), whereas the upper dots mean derivation with respect to time.

2.5. *External Excitation.* Within the input data of the problem, the time-history of external excitation is given, which is here the variation of axial forces of cables due to traffic. The function $N(t)$ is assumed to be described by a piecewise

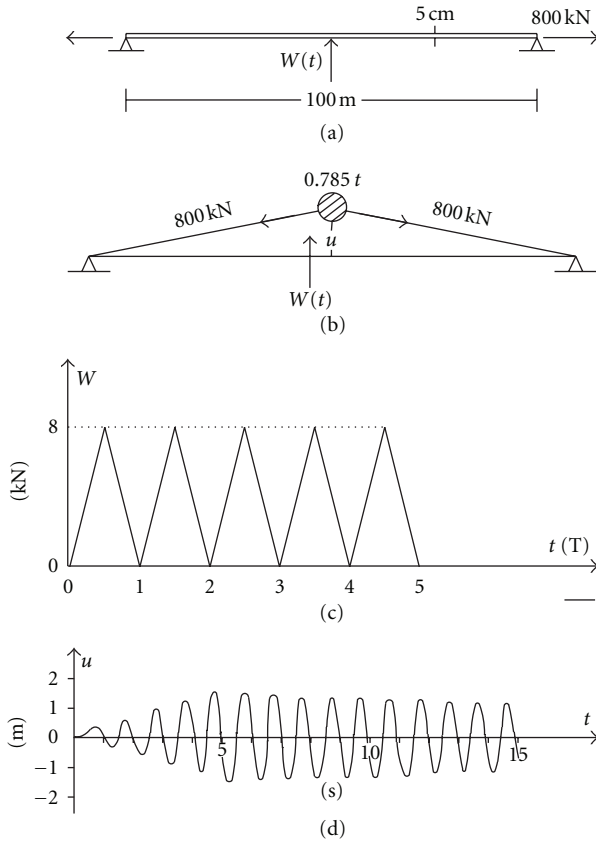


FIGURE 6: Fourth application: isolated cable subject to wind. (a) Given geometry and loading. (b) Parameters of dynamic analysis. (c) Given time-history of wind drag force. (d) Resulting time-history of displacement of center of cable.

linear curve, as shown in Figure 2(c). And within each time interval, between two successive nodes, a linear interpolation is performed, in order to find, from a specific time instant t , the corresponding axial force N of the cables.

2.6. Initial Value Problem. A state vector is introduced:

$$\mathbf{y} = \{\mathbf{u} \mathbf{v} \mathbf{c}\}, \quad (8)$$

consisting of the vertical displacements $\mathbf{u} = \{u_o u_u\}$ (Figure 2(a)) and velocities $\mathbf{v} = \{\dot{u}_o \dot{u}_u\}$ of the centers of upper and lower cables, respectively, as well as of the constitutive variables $\mathbf{c} = \{\epsilon_{opl} \epsilon_{upl}\}$, which are the plastic strains (Figure 2(b)) of upper and lower cross-ties, respectively.

By combining all the previous equations, (1) up to (8), a system of first-order ordinary nonlinear differential equations is obtained:

$$\dot{\mathbf{y}} = \mathbf{q}(t, \mathbf{y}), \quad (9a)$$

which, along with the initial value of the state vector

$$\mathbf{y}(0) = \mathbf{y}_o \quad (9b)$$

for time $t = 0$, and with sought function the time-history of the state vector $\mathbf{y}(t)$, constitutes an initial value problem.

2.7. Proposed Algorithm. For the step-by-step dynamic analysis (direct time integration) of the previous initial value problem of (9a) and (9b), the algorithm of trapezoidal rule is proposed:

$$\mathbf{y}_{n+1} = \mathbf{y}_n + \frac{1}{2} [\mathbf{q}(t_n, \mathbf{y}_n) + \mathbf{q}(t_{n+1}, \mathbf{y}_{n+1})] \Delta t, \quad (10)$$

where n and $n + 1$ are two successive steps of the algorithm. This coincides with the algorithm of constant average acceleration of Newmark's group of algorithms for step-by-step dynamic analysis.

The aforementioned algorithm is combined with a predictor-corrector technique, with two corrections per step, PE(CE)², where, in this symbol, P means prediction and C correction of the state vector \mathbf{y} , whereas E means evaluation of the function $\mathbf{q}(t, \mathbf{y})$ of (9a). In more detail, the proposed predictor-corrector technique can be written, within any n th step of the algorithm, as follows:

Prediction

$$\mathbf{y}_{n+1}^P = \mathbf{y}_n + \mathbf{q}(t_n, \mathbf{y}_n) \Delta t, \quad (11a)$$

First correction

$$\mathbf{y}_{n+1}^1 = \mathbf{y}_n + \frac{1}{2} [\mathbf{q}(t_n, \mathbf{y}_n) + \mathbf{q}(t_{n+1}, \mathbf{y}_{n+1}^P)] \Delta t, \quad (11b)$$

Second and final correction

$$\mathbf{y}_{n+1} = \mathbf{y}_n + \frac{1}{2} [\mathbf{q}(t_n, \mathbf{y}_n) + \mathbf{q}(t_{n+1}, \mathbf{y}_{n+1}^1)] \Delta t. \quad (11c)$$

Thanks to the aforementioned predictor-corrector technique, no solving of algebraic system is needed, within each step of the algorithm.

The stability criterion of the proposed algorithm is [9]

$$\omega_{\max} \Delta t < 2.0 \text{ rad}, \quad (12)$$

that is, $\Delta t < T_{\min}/\pi$; otherwise a divergent solution results, whereas the accuracy criterion is at least

$$\omega_{\max} \Delta t < 0.5 \text{ rad}, \quad (13)$$

that is, $\Delta t < T_{\min}/4\pi = T_{\min}/12.56$; otherwise a significant accumulated truncation error appears, which is expressed as amplitude decay of the vibration, as well as period elongation.

3. Computer Program

Based on the proposed algorithm of previous Section 2.7, a simple and very short computer program has been developed, with only 115 Fortran instructions, consisting of the MAIN program (79 instructions) which performs the algorithm of step-by-step dynamic analysis, and of three subroutines: (1) Subroutine EVAL (17 instructions) which evaluates the present strain and stress state of the cable structure under consideration, (2) subroutine SE (9 instructions)

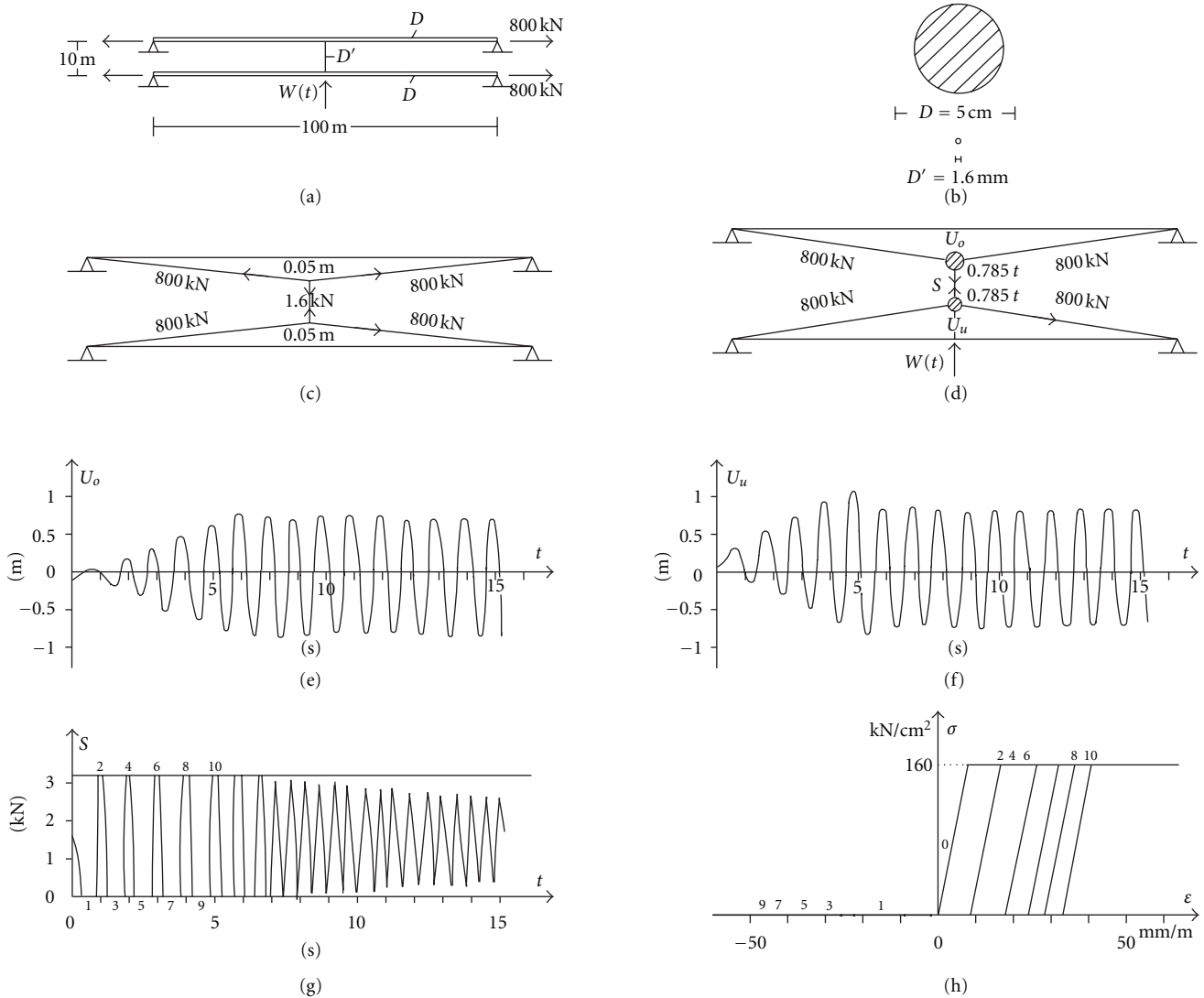


FIGURE 7: Fifth application: couple of interconnected cables subject to wind. (a) Given geometry and loading. (b) Cross sections of main cables and cross-tie. (c) Initial static analysis. (d) Parameters of dynamic analysis. (e), (f) Resulting time-histories of displacements of two main cables. (g) Resulting time-history of axial force of cross-tie. (h) Resulting hysteresis stress-strain loops of the cross-tie.

which describes the nonlinear uniaxial stress-strain law of a cross-tie, and (3) subroutine NHIST (10 instructions) describing the given time-history of the external excitation, which is, here, the variation, with respect to time, of the axial force of cables due to traffic.

A full documentation of the previous computer program is presented as Appendix, consisting of the description of program line by line in Section A.1, of the complete list of Fortran instructions in Section A.2, and the variables explanation in Section A.3. The documentation of the computer program is completed by the series of seven applications in Section 4. The program is particularly oriented to the specific third application of Section 4.3, as already mentioned in the equations of problem in Section 2. However, by simple and obvious modifications of the computer program, all the other numerical experiments, in Section 4, can be treated, too.

4. Applications (Numerical Experiments)

Seven applications (numerical experiments) follow, on the dynamic analysis of isolated pretensioned cables of a cable-stayed bridge or couples of parallel cables connected to each other and possibly with the deck of the bridge by very thin pretensioned single wires (cross-ties). Three of these cable structures are subjected to variation of axial forces of cables due to traffic (parametric excitation) and four of them are subjected to successive pulses of drag force due to a strong wind.

As already mentioned, the previously presented algorithm, in Section 2, is oriented only to the specific third application of Section 4.3. However, by simple and obvious modifications of this algorithm, all the other applications present in Section 4, which are presented herein after, have been analysed, too.

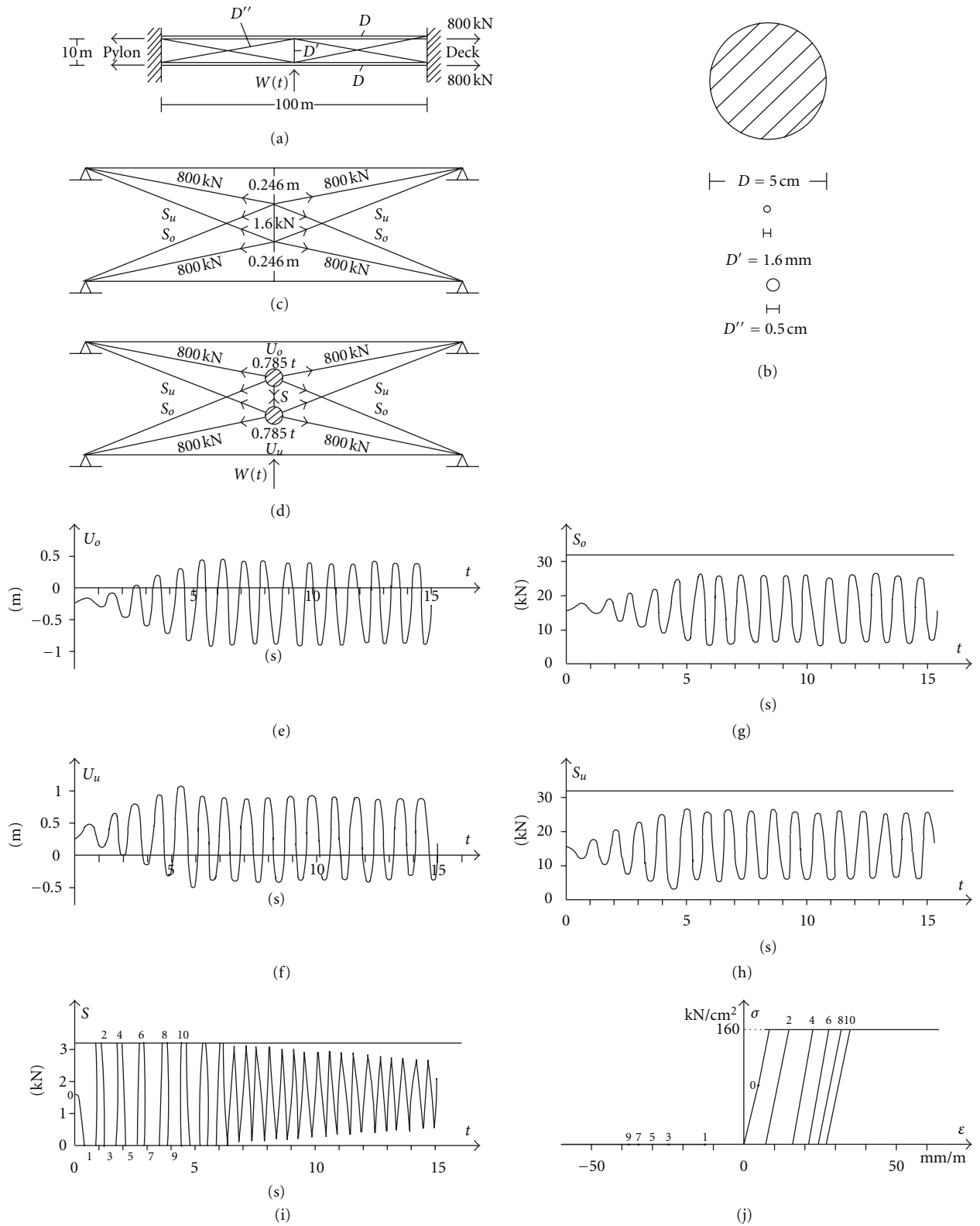


FIGURE 8: Sixth application: couple of cables interconnected by cross-tie, additionally connected by diagonals to pylon and deck, subject to wind. (a) Given geometry and loading. (b) Cross sections of main cables, cross-tie and diagonals. (c) Initial static analysis. (d) Parameters of dynamic analysis. (e), (f) Resulting time-histories of displacements of two main cables. (g), (h) Resulting time-histories of axial forces of diagonal bars. (i) Resulting time-history of axial force of cross-tie. (j) Resulting stress-strain loops of the cross-tie.

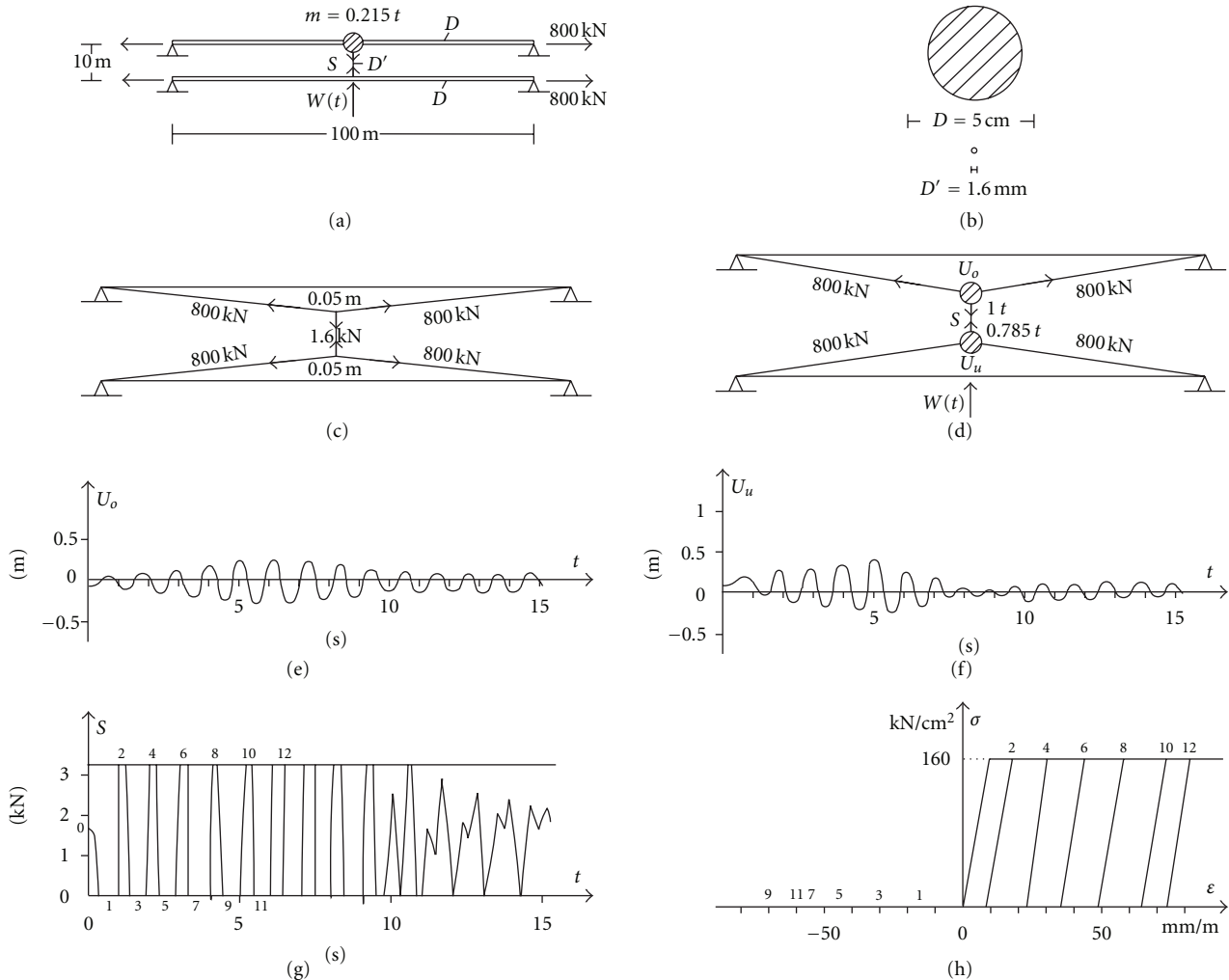


FIGURE 9: (a) Seventh application: Couple of inter-connected cables subject to wind with additional small mass on one cable. (a) Given geometry, loading and additional small mass. (b) Comparison of cross-sections of cables and cross-tie. (c) Initial static analysis. (d) Parameters of dynamic analysis. (e), (f) Resulting time-histories of displacements of two cables. (g) Resulting time-history of axial force of cross-tie. (h) Resulting hysteresis stress-strain loops of the cross-tie.

4.1. *First Application: Isolated Cable Subject to Traffic.* As shown in Figure 3, an isolated cable is subjected to a periodic variation of its axial force with a period equal to its fundamental one. Up to the fifth cycle that the excitation lasts, the vibration amplitude of the cable increases up to about 1.6 m and then remains constant; only a slight algorithmic damping is observed.

4.2. *Second Application: Couple of Interconnected Cables Subject to Traffic.* The cable of first application is, in Figure 4, connected to another shorter parallel cable by a thin cross-tie. Both cables are subjected to a periodic variation of their axial force with a period equal to the fundamental one of the cable system. Up to the fifth cycle that the excitation lasts, the vibration amplitude of the upper cable increases up to 1.4 m and that of the shorter lower cable up to 0.7 m. Then, both amplitudes are gradually reduced, the upper one up to 0.4 m and the lower one up to 0.3, in 10 sec. Because of the different

lengths of the two cables, thus different geometric stiffness, masses, and weights, too, large differences of displacements at the ends of the cross-tie are obtained, thus large stress-strain loops with a total width $\Delta\epsilon \approx 76 mm/m$, which are responsible for the significant hysteresis damping which is achieved.

4.3. *Third Application: Couple of Cables Connected to Each Other and to Deck, Subject to Traffic.* The cable system of the second application is, in Figure 5, supplied by one more thin cross-tie connecting the lower cable with the deck of the bridge. Because of the stiffness of this additional cross-tie, the maximum vibration amplitudes of both cables are significantly reduced, that of the upper cable to 0.7 m and that of the lower cable to 0.3 m. However, at same time, this reduction of displacements has a consequence less wide stress-strain loops in the upper cross-tie with total width $\Delta\epsilon \approx 38 mm/m$ and very thin stress-strain loops in the lower

```

1   COMMON/A/AW, HO, HO0, DHO, EO, SO, TO, HU, HU0, DHU, *EU, SU, TU, WO, WU, N,
    LO, LU, FO, FU, MO, MU
2   COMMON/B/EY, ELAST
3   COMMON/C/NN, TK, NK
4   REAL LO, LU, MO, MU, N, NK
5   DIMENSION TK(20), NK(20)
6   OPEN(5,FILE = "TIEIN.TXT")
7   OPEN(6,FILE="TIEOUT.TXT")
8   READ(5,1)LO,LU,HO,HU,DC,DW,DENS
9   1  FORMAT(7F10.0)
10  AC = 3.14159*DC**2/4.
11  MO = DENS*AC*LO/2./10000.
12  WO = -MO*10.
13  MU = DENS*AC*LU/2./10000.
14  WU = -MU*10.
15  AW = 3.14159*DW**2/4./10000.
16  READ(5,1)SY,ELAST,SC0,SW0
17  EY = SY/ELAST
18  N = SC0*AC
19  TO = SW0*AW
20  TU = SW0*AW
21  READ(5, 2)NN,TMAX
22  2  FORMAT(15, F10.0)
23  READ(5,3)(TK(I), NK(I), I = 1,NN)
24  3  FORMAT(40F5.2)
25  STIF1 = 2. *N/(LO/2.) + ELAST*AW/HO
26  STIF2 = 2. *N/(LU/2.) + ELAST*AW/HO+ELAST*AW/HU
27  STIF12 = -ELAST*AW/HO
28  A = MO*MU
29  B = -(STIF1*MU + STIF2*MO)
30  C = STIF1*STIF2-STIF12**2
31  D = SQRT(B* * 2 - 4. *A*C)
32  W1=SQRT((-B + D)/(2. *A))
33  W2 = SQRT((-B + D)/(2. * A))
34  T1 = 2. * 3.14159/W1
35  T2 = 2. * 3.14159/W2
36  DO 4 I = 1, NN
37  4  TK(1) = TK(1) * T2
38  DT=T2/(4. * 3.14159)
39  T = 0.
40  UO = (WO-TO)/(2. *N/(LO/2.))
41  UU = (WU + TO - TU)/(2. *N/(LU/2.))
42  VO = 0.
43  VU = 0.
44  EOPL = 0.
45  EUPL = 0.
46  EW0 = SW0/ELAST
47  HO0 = (HO + UO - UU)/(1. + EW0)
48  HU0 = (HU + UU)/(1. + EW0)
49  CALL EVAL(UO,UU,EOPL,EUPL,GO,GU)
50  5  T = T + DT
51  CALL NHIST(T, N)
52  UOP = UO + VO*DT
53  UUP = UU + VU*DT
54  VOP = VO + GO*DT
55  VUP = VU + GU*DT
56  EOPLP = EOPL
57  EUPLP = EUPL
58  CALL EVAL (UOP, UUP, EOPLP, EUPLP, GOP, GUP)
59  UO1 = UO + (VO + VOP)/2. *DT
60  UU1= UU + (VU + VUP)/2. *DT

```

```

61      VO1 = VO + (GO + GOP)/2. * DT
62      VU1 = VU + (GU + GUP)/2. *DT
63      EOPL1 = EOPL
64      EUPL1 = EUPL
65      CALLEVAL (UO1, UU1, EOPL1, EUPL1, GO1, GU1)
66      UO =UO + (VO+VO1)/2. *DT
67      UU = UU + (VU + VU1)/2. *DT
68      VO = VO + (GO+GO1)/2. *DT
69      VU = VU + (GU + GU1)/2. *DT
70      CALL EVAL (UO, UU, EOPL, EUPL, GO, GU)
71      WRITE (6,6)T,N,UO,UU,TO,TU
72      WRITE (6,6)EO,SO,EU,SU
73      6   FORMAT(1X,5(E10.4,1X))
74      IF(T.GT.TMAX) GO TO 7
75      GO TO 5
76      7   CLOSE(5)
77      CLOSE(6)
78      STOP
79      END

```

ALGORITHM 1: MAIN program.

```

1      SUBROUTINE EVAL(UO,UU,EOPL,EUPL,GO,GU)
2      COMMON/A/AW,HO,HO0,DHO,EO,SO,TO,HU,HU0,DHU,EU, *SU,TU, WO, WU,
      N, LO, LU, FO, FU, MO, MU
3      REAL LO, LU, MO, MU, N
4      DHO = HO + UO - UU - HO0
5      EO = DHO/HO0
6      CALL SE(EO,EOPL,SO)
7      TO = SO*AW
8      DHU = HU + UU - HU0
9      EU = DHU/HU0
10     CALL SE(EU,EUPL,SU)
11     TU = SU*AW
12     FO = WO - 2. *N/(LO/2.)*UO - TO
13     FU = WU - 2. *N/(LU/2.)*UU + TO - TU
14     GO = FO/MO
15     GU = FU/MU
16     RETURN
17     END

```

ALGORITHM 2: Subroutine EVAL.

```

1      SUBROUTINE SE(E, EPL, S)
2      COMMON/B/EY, ELAST
3      IF(E.GT.EPL + EY)EPL=E-EY
4      IF(E.LT.EPL)EPL=E
5      IF(EPL.LT.0.)EPL=0.
6      S = ELAST*(E - EPL)
7      IF(S.LT.0.)S = 0.
8      RETURN
9      END

```

ALGORITHM 3: Subroutine SE.

```

1   SUBROUTINE NHIST(T,N)
2   COMMON/C/NN, TK, NK
3   DIMENSION TK(20), NK(20)
4   REAL N, NK
5   DO 1 I = 1, NN-1
6   IF((T- TK(1))*(T- TK(I + 1)).GT.0.) GO TO 1
7   N = NK(I) + (NK(I + 1)-NK(I))/(TK(I + 1)-TK(I))*(T-TK(I))
8   RETURN
9   1  CONTINUE
10  END

```

ALGORITHM 4: Subroutine NHIST.

cross-tie with only $\Delta\epsilon \approx 6$ mm/m, resulting in low values of hysteretic damping.

4.4. Fourth Application: Isolated Cable Subject to Wind. As shown in Figure 6, an isolated cable is subjected to a resonant periodic wind drag force. Up to the fifth cycle that the excitation lasts, the vibration amplitude increases up to about 3.0 m and then remains constant; only a slight algorithmic damping is observed.

4.5. Fifth Application: Couple of Interconnected Cables Subject to Wind. Two identical parallel cables are, in Figure 7, interconnected by a thin cross-tie. A wind drag force acts on one cable only; initially, this cable exhibits larger displacements, but gradually the movement is transferred to the other cable, too. So, the displacements are divided by two, compared with those of previous fourth application. During the initial stage of displacements transfer from one cable to the other, stress-strain loops of the cross-tie with a total width of medium size $\Delta\epsilon \approx 33$ mm/m appear. From this point on, as the two cables are identical and perform similar movements, no more yielding of the cross-tie appears, as shown in Figure 7(g), thus no more stress-strain loops and hysteretic damping, too.

4.6. Sixth Application: Couple of Interconnected Cables, Additionally Connected by Diagonals to Pylon and Deck, Subject to Wind. The cable system of the fifth application is, in Figure 8, supplied with diagonal ties connected with the pylon and the deck of the bridge. These diagonal ties offer a small additional stiffness, perpendicularly to the cables, which slightly reduces their displacements. However, at same time, this restriction of displacements further reduces the total width of stress-strain loops of the cross-tie to $\Delta\epsilon \approx 27$ mm/m, thus reducing the hysteretic damping.

4.7. Seventh Application: Couple of Interconnected Cables Subject to Wind, with Small Additional Mass on One Cable. The cable system of fifth application is in Figure 9, supplied by a small additional mass to the one of the two cables. So, the two cables have now different dynamic characteristics and they perform significantly different movements. As a consequence, large differences of displacements at the ends of the cross-tie result, thus wide stress-strain loops with a total

width $\Delta\epsilon \approx 73$ mm/m, which implies significant hysteretic damping. The displacement amplitudes of the cables are now only about one-fourth of those of the fifth application.

5. Conclusions

Cable vibrations of cable-stayed bridges have been examined. Either isolated cables or couples of parallel cables, connected to each other and possibly with the deck of the bridge, by a very thin pretensioned wire (cross-tie), have been considered. External excitation is either traffic, which causes displacements of cable ends on deck and pylon, thus variation of axial forces, geometric stiffnesses and sags of cables, too (parametric excitation), or successive pulses of drag force due to a strong wind, perpendicularly to a vertical cables' plane at one side of the bridge.

The proposed analytical model is on the one hand simplified, as an SDOF oscillator is adopted for every individual cable, approximating its fundamental vibration mode. However, on the other hand, the proposed analytical model is accurate, as it takes into account the geometric nonlinearity of the cables by their geometric stiffness; also it includes the material nonlinearity of the cross-ties by their compressive loosening, tensile yielding, and hysteretic stress-strain loops.

The equations of the problem of dynamic analysis, oriented to a specific cable structure, have been written, consisting of the geometric, constitutive, static, and dynamic ones, as well as of the given time-history of the external excitation. By combining these equations, an initial value problem is obtained. For the step-by-step dynamic analysis of this problem, the algorithm of trapezoidal rule is proposed, combined with a predictor-corrector technique, with two corrections per step. So, no solving of algebraic system is required within each step of the algorithm.

Based on the proposed algorithm, a short computer program has been developed, with only 115 Fortran instructions, consisting of the main program and three subroutines. A full documentation is given for this program, which means transparency of computation.

Seven numerical experiments have been performed by the aforementioned program, three with variation of axial forces of cables due to traffic (parametric excitation) and four with successive pulses of drag force due to a strong wind.

On the basis of previous series of numerical experiments some observations with practical usefulness are made. (These are not strict theoretical conclusions, but simple observations based on the results of numerical experiments.)

It is confirmed by the series of numerical experiments, the great advantage of pretensioned cross-ties, that although they are very thin, with ratio of cross-section area of a cable to that of a cross-tie of magnitude order 1000, however, they possess an axial elastic stiffness comparable in magnitude to the geometric stiffness of cables, with magnitude order 50 kN/m, along the same direction, that is perpendicularly to cables axes.

The in-plane cross-ties (within a vertical cables plane) are intended to suppress cables' variations from parametric excitation due to traffic, whereas the out-of-plane cross-ties (transverse ones connecting cables at two sides of bridge) are intended to suppress cables vibrations from successive pulses of drag force due to a strong wind.

General observation from all numerical experiments: in a couple of parallel cables connected to each other and possibly with the deck of bridge by cross-ties, even a single cross-tie proves effective by its hysteresis damping (due to stress-strain loops) in suppressing large amplitude cable vibrations under the following circumstances: if the two cables have different dynamic characteristics, for example, different lengths which imply different masses, weights, and geometric stiffnesses, too, or if one of them has a small additional mass.

Appendices

A. Documentation of the Proposed Computer Program

In this appendix, documentation is given for the proposed computer program, for the step-by-step dynamic analysis of the third application, that of a couple of parallel cables connected to each other and to the deck of bridge by a thin cross-tie and subject to a variation of their axial forces.

A.1. Description of Program Line by Line. The description refers to the complete numbered list of Fortran instructions of Algorithms 1, 2, 3, 4.

MAIN Program. The first seven lines include nonexecutable statements. Particularly, in the three first lines, the COMMON instructions connect the MAIN program with the three subroutines, by their common variables.

In the next 17 lines, 8 up to 24, the input data are read: geometric data and density of steel in lines 8-9, the parameters of σ - ϵ law of steel along with the pretension stresses of cables and cross-ties in line 16, and the time-history of axial forces of cables given by the coordinates of nodes of piecewise linear curve N - t in lines 21-24. In lines 10-15 and 17-20, some simple preliminary calculations are performed to determine cross-section areas and pretension forces of cables and cross-ties, as well as masses and weights of cables and yield strain of steel. In lines 25-35, the initial characteristic equation of the cable structure is solved, so

that to find its natural frequencies and periods. In lines 36-37, the time scale of the given time history of external excitation is expanded so that to obtain a period equal to the fundamental one T_{\max} of the structure, in order to cause resonance, whereas in line 38, the minimum natural period T_{\min} of the structure dictates the time-step length Δt of the algorithm, so that to assure accuracy of computation.

In lines 39-49, the initial conditions are established: time $t = 0$ in line 39, determination of initial static displacements of cables in lines 40-41, evaluation of undeformed lengths of cross-ties in lines 42-44, zero initial velocities of cables in lines 45-46, zero initial plastic strains of cross-ties in lines 47-48, and evaluation of initial strain and stress state of structure by calling subroutine EVAL in line 49.

In line 50, any step of algorithm begins by increasing time t by Δt . In line 51, by calling subroutine NHIST, the present value of axial force of cables is determined. In lines 52-55, the prediction of values of displacements and velocities is performed, and in lines 56-58 by calling subroutine EVAL the corresponding plastic strains and accelerations are found. So in lines 52-58 the prediction of state vector within a step of algorithm is performed. In lines 59-65 the first correction of value of state vector is made by use of trapezoidal rule. And in lines 66-70, the second and final correction. In lines 71-73, the output data of present step of algorithm are written (time t , axial force N of cables, displacements u_o and u_u of cables, axial forces S_o and S_u of cross-ties, strains and stresses ϵ_o - σ_o and ϵ_u - σ_u of cross-ties).

In lines 74-79 if a maximum time has been exhausted, the algorithm is interrupted. Otherwise, we continue to the next step of the algorithm.

Subroutine EVAL. Lines 1-3 are nonexecutable statements. In lines 4-7, from the displacements of cables, the elongation, strain, stress by calling subroutine SE, and axial force of upper cross-tie are determined. In lines 8-11, the corresponding quantities are found for the lower cross-tie. In lines 12-13, the vertical nodal forces on centers of upper and lower cables are determined and in lines 14-15 the corresponding accelerations.

Subroutine SE. In lines 3-5, the new plastic strain of the cross-tie is found. In lines 6-7, the stress of the cross-tie is determined.

Subroutine NHIST. In line 5 is found the time interval where present time t is included. In line 6, a linear interpolation is performed between the two end-nodes of the previous time interval, in order to find the axial force N of cables corresponding to present time t .

A.2. List of Fortran Instructions

MAIN Program.

See Algorithms 1, 2, 3, and 4.

A.3. Variables Explanation

MAIN Program.

$A = m_o \times m_u$ coefficient of characteristic equation
 AC: cross-section area of a cable
 AW: cross-section area of a wire (cross-tie)
 $B = -(K_{11}m_u + K_{22}m_o)$ coefficient of characteristic equation
 $C = K_{11} \times K_{22} - K_{12}^2$ coefficient of characteristic equation
 $D = (b^2 - 4ac)^{1/2}$ coefficient of characteristic equation
 DC: cross-section diameter of a cable
 DENS: density of steel
 DHO: elongation of upper tie
 DHU: elongation of lower tie
 DW: cross-section diameter of wire (cross-tie)
 $DT = \Delta t$, time steplength of algorithm
 ELAST: initial elasticity (Young) modulus
 EO: strain of upper tie
 EOPL: plastic strain of upper tie
 EOPLP: prediction of EOPL
 EOPL1: first correction of EOPL
 EU: strain of lower tie
 EUPL: plastic strain of lower tie
 EUPLP: prediction of EUPL
 EUPL1: first correction of EUPL
 EVAL: subroutine for evaluation of strain and stress state of the structure
 EW0: pretension strain of wires (cross-ties)
 EY: yield strain of steel
 FO: vertical nodal force at center of upper cable
 FU: vertical nodal force at center of lower cable
 GO: vertical acceleration at center of upper cable
 GOP: prediction of GO
 GO1: first correction of GO
 GU: vertical acceleration at center of lower cable
 GUP: prediction of GU
 GU1: first correction of GU
 HO: design (nominal) length (height) of upper cross-tie
 HO0: undeformed length (height) of upper cross-tie
 HU: design (nominal) length (height) of lower cross-tie
 HU0: undeformed length (height) of lower cross-tie
 LO: length of upper cable

LU: length of lower cable
 MO: mass of upper cable
 MU: mass of lower cable
 N: axial force of a cable
 NHIST: subroutine for given time-history of N
 NK: ordinate of a node of piecewise linear curve $N-T$
 NN: number of nodes of piecewise linear curve $N-T$
 SO: stress of upper cross-tie
 STIF1: K_{11} elements of stiffness matrix
 STIF2: K_{22} elements of stiffness matrix
 STIF12: K_{12} elements of stiffness matrix
 SU: stress of lower cross-tie
 SW0: pretension stress of wires (cross-ties)
 SY: yield stress of steel
 T: time
 TIEIN: input file
 TIEOUT: output file
 TK: abscissa of a node of piecewise linear curve $N-T$
 TMAX: t_{\max} , maximum time of observation
 TO: axial force of upper cross-tie
 TU: axial force of lower cross-tie
 $T1: T_{\min}$ extreme natural periods of structure {list-item};label/; }
 $T2: T_{\max}$ extreme natural periods of structure
 UO: vertical displacement of center of upper cable
 UOP: prediction of UO
 UO1: first correction of UO
 UU: vertical displacement of center of lower cable
 UUP: prediction of UU
 UU1: first correction of UU
 VO: vertical velocity of center of upper cable
 VOP: prediction of VO
 VO1: first correction of VO
 VU: vertical displacement of center of lower cable
 VUP: prediction of VU
 VU1: first correction of VU
 WO: weight at center of upper cable
 WU: weight at center of lower cable
 $W1: \omega_{\max}$ extreme natural frequencies of the structure
 $W2: \omega_{\min}$ extreme natural frequencies of the structure.

Subroutine EVAL. Only the following variable is different from those of MAIN program:

SE: subroutine for stress-strain law of a cross-tie.

Subroutine SE. Only the following variables are different from those of MAIN program:

- E: strain of a cross-tie
- EPL: plastic strain of a cross-tie
- S: stress of a cross-tie.

Subroutine NHIST. All the variables are the same as in MAIN program.

References

- [1] R. Walther, B. Houriet, W. Isler, P. Moia, and J. F. Klein, *Cable-Stayed Bridges*, Th. Telford, London, UK, 2nd edition, 1999.
- [2] E. Caetano, "Cable vibrations in cable-stayed bridges," IABSE-Structural Engineering Documents, 2007.
- [3] L. Caracoglia and D. Zuo, "Effectiveness of cable networks of various configurations in suppressing stay-cable vibration," *Engineering Structures*, vol. 31, no. 12, pp. 2851–2864, 2009.
- [4] L. Caracoglia and N. P. Jones, "Passive hybrid technique for the vibration mitigation of systems of interconnected stays," *Journal of Sound and Vibration*, vol. 307, no. 3–5, pp. 849–864, 2007.
- [5] L. Caracoglia and N. P. Jones, "In-plane dynamic behavior of cable networks. Part 1: formulation and basic solutions," *Journal of Sound and Vibration*, vol. 279, no. 3–5, pp. 969–991, 2005.
- [6] L. Caracoglia and N. P. Jones, "In-plane dynamic behavior of cable networks. Part 2: prototype prediction and validation," *Journal of Sound and Vibration*, vol. 279, no. 3–5, pp. 993–1014, 2005.
- [7] P. G. Papadopoulos, A. Diamantopoulos, P. Lazaridis, H. Xenidis, and C. Karayiannis, "Simplified numerical experiments on the effect of hysteretic damping of cross-ties on cable oscillations," in *9th International Conference on Computational Structures Technology*, Athens, Greece, September 2008.
- [8] P. G. Papadopoulos, J. Arethas, P. Lazaridis, E. Mitsopoulou, and J. Tegos, "A simple method using a truss model for in-plane nonlinear static analysis of a cable-stayed bridge with a plate deck section," *Engineering Structures*, vol. 30, no. 1, pp. 42–53, 2008.
- [9] P. G. Papadopoulos, "A simple algorithm for the nonlinear dynamic analysis of networks," *Computers and Structures*, vol. 18, no. 1, pp. 1–8, 1984.

Research Article

Pile Group Protection with Riprap Mattress

Christian Chreties,¹ Luis Teixeira,¹ and Gonzalo Simarro²

¹Facultad de Ingeniería, Universidad de la República, Julio Herrera y Reissig 565, 11300 Montevideo, Uruguay

²Instituto de Ciencias del Mar, Consejo Superior de Investigación Científica (CSIC), Paseo Marítimo de la Barceloneta 37-49, 08003 Barcelona, Spain

Correspondence should be addressed to Christian Chreties, chreties@fing.edu.uy

Received 18 November 2011; Accepted 8 February 2012

Academic Editor: Sami W. Tabsh

Copyright © 2012 Christian Chreties et al. This is an open access article distributed under the Creative Commons Attribution License, which permits unrestricted use, distribution, and reproduction in any medium, provided the original work is properly cited.

New experimental data on plan dimensions for riprap mattresses used in pile group protection against edge failure are analyzed. The influence of flow conditions and the distance between piles in plan dimensions of riprap mattresses are addressed. An alternative methodology for the experimental study of edge failure in pile groups is proposed and verified, significantly reducing the duration of tests (from several days to a few hours) and yielding similar results. For the pile group configuration tested, a design expression for minimum riprap width is obtained. The influence of the distance between the piles on the width of riprap dimensions is shown to be small, and the proposed expression compares well with some of the expressions for single piers found in the literature.

1. Introduction

There are basically two different ways of actively protecting alluvial bridges against the local scour that develops at their foundations. First, armouring devices (e.g., riprap mattresses or cable-tied blocks) that *strengthen* the bed against scour and secondly, flow-altering devices (e.g., slots or sacrificial piers) that weaken the flow capacity to remove sediment around the bridge foundation. Riprap mattresses are probably the most frequently used of all methods and, because riprap elements are expensive, a proper knowledge of the problem is required in order to obtain an economical and safe design [1]. Due to the complexity of the physical mechanisms related to turbulent three-dimensional flow involving sediment transport, the experimental approach is a usual practice to analyze this problem.

While in the last twenty years, intensive work has been done to improve knowledge of riprap design as a countermeasure against local scour both for bridge abutments [2–7] and for single piers [8–11], little work has addressed the case of pile groups. Although pile groups are frequent structures for bridge foundations, to the author's knowledge, the only works devoted to the protection of pile groups are those by Vittal et al. [12], Zarrati et al. [13],

and Simarro et al. [14]. Furthermore, Vittal et al. [12] and Zarrati et al. [13] consider flow altering devices (collars), while Simarro et al. [14], who does analyze riprap mattresses, only addresses the problem of riprap block sizing.

There are basically four different failure mechanisms for riprap mattresses, namely, shear failure, edge failure, winnowing failure, and bed-form undermining [8]. A fifth mechanism involving bed degradation could be added. Although these four mechanisms are not entirely independent, there is common agreement on how each mechanism can be avoided. For instance, shear failure—which occurs when riprap blocks are mobilized due to shear stress transmitted by flow—can be avoided if the riprap blocks are sufficiently large. Winnowing failure, in which the underlying finer bed material escapes through the voids of the riprap, is due to the differences between bed and block sizes and can be avoided using a gravel or synthetic filter. Bed-form undermining is riprap instability due to sand dunes passing through riprap elements and can be avoided by placing the riprap mattress below the trough of the expected bed-forms. Finally, edge failure, the mechanism this work is focused on, occurs when the local scour hole that develops at the river bed beyond the riprap mattress, affects riprap protection by causing its blocks to fall (as shown



FIGURE 1: Edge failure mechanism in pile group model. Water flowing leftwards.

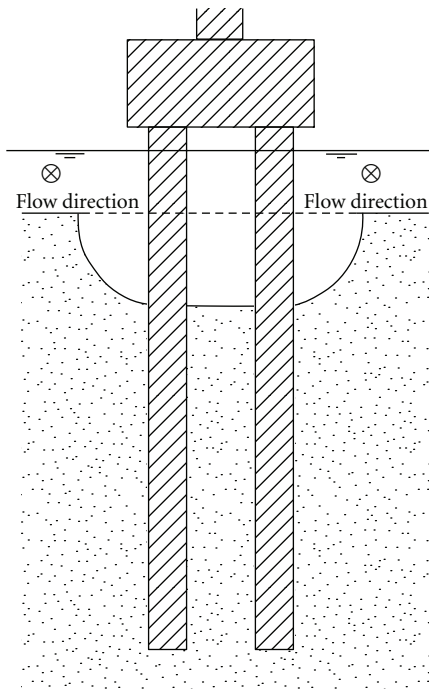


FIGURE 2: Pile group configuration used in experimental campaign.

in Figure 1). Edge failure is avoided by making the riprap mattress sufficiently wide.

The mechanisms are usually analyzed separately, and the worst conditions are considered in each case. For edge failure, the flow conditions are such that the river bed material (finer than the riprap blocks) is close to the entrainment condition, that is, $u \approx u_c$, where u is the mean velocity of the approaching flow, and u_c is the critical mean velocity for bed material entrainment. Because the local scour process occurring by the riprap mattress can develop slowly over time, long experiments (lasting more than 1 week) are usually required to assess whether a given mattress width is sufficient or not [5].

Recently, Ballio et al. [15] have presented an experimental investigation on temporal scales for live-bed scour at abutments, finding that the time taken to reach equilibrium scour depth rapidly decreases as the flow intensity increases.

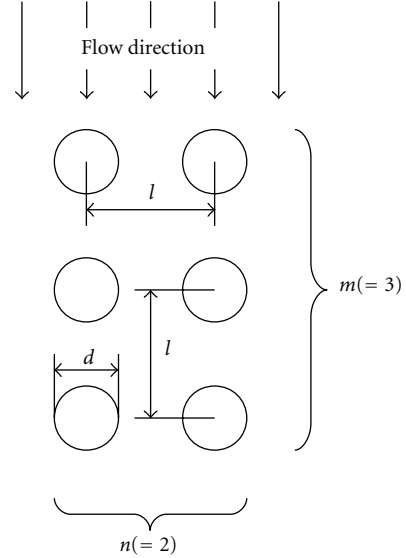


FIGURE 3: Plan view of the pile group and riprap mattress.

Taking into account the above result, in this work we will find an expression for the required extent (width) of the riprap mattress to protect a given pile group geometry. The approach is so that the required time of each experiment is reduced to few hours. In the next section, the proposed methodology is presented; followed by the experimental setup and results and finally, some concluding remarks are made.

2. Methodology

In this work we study the case in which only the pile group is exposed to flow (Figure 2), that is, the fifth case of those considered by Coleman [16].

Assuming uniform bed material and a normal flow to the pile group (i.e., with a zero skew angle, as shown in Figure 3), and negligible contraction and viscous effects, the required riprap mattress width, w , as defined in the same Figure 3, can be expressed as

$$w = \phi(u, h, \rho, \rho_s, d_{50}, g, d, \Gamma, n, m), \quad (1)$$

where u and h are the approaching mean velocity and water depth, ρ is the water density, d_{50} is the size of the bed sediment, ρ_s the sediment density (bed and riprap), g the gravity, d the diameter of the individual piers and $\Gamma \equiv l/d$, m and n dimensionless numbers defining the geometry of the pile group (Figure 3). We remark that the width w does not depend on the size of the riprap blocks [7].

Applying dimensional analysis to the above expression, and noting that in the pile group experiments $m = 3$ and $n = 2$, we get

$$\frac{w}{d} = \phi\left(\frac{u^2}{gd_{50}}, \frac{h}{d}, \frac{\rho_s}{\rho}, \frac{d_{50}}{d}, \Gamma\right) \quad (2)$$

or alternatively [17],

$$\frac{w}{d} = \phi \left(I \equiv \frac{u}{u_c}, \frac{h}{d}, \frac{\rho_s}{\rho}, \frac{d_{50}}{d}, \Gamma \right), \quad (3)$$

where u_c is computed ignoring any upstream viscous effects.

Since $\rho_s/\rho = 2.65$ in all experiments (as in real problems), the dimensionless group ρ_s/ρ can be ignored above. Furthermore, overlooking the influence of d_{50}/d [18], as the influence of d_{50} is described through u/u_c , we finally obtain

$$\frac{w}{d} = \phi \left(I \equiv \frac{u}{u_c}, \frac{h}{d}, \Gamma \right). \quad (4)$$

As mentioned above, in the literature for edge failure experiments, flow intensity I is set close to one ($I \approx 1$) and the experiment is run until an equilibrium condition is reached. “Equilibrium criteria,” such as those proposed by, for example, Cardoso and Bettess [19] or Melville and Chiew [20] are required to establish when the experiment is finished. These equilibrium criteria are subject to errors that can be of significance, as noted by Simarro et al. [21].

Here, we consider keeping flow conditions constant during the experiment, but use weak live bed conditions ($I \approx 1.3$) in order to speed up the local scour process occurring by the riprap mattress. In this way, bed-forms will be generated, so that bed-form undermining failure can occur. However, these bed-forms will be relatively small (2 cm) and their influence will be shown experimentally as negligible in our problem (the results of w/d will be compared for $I \approx 1$ and $I = 1.3$). This procedure will also be used for single piers (case $m = n = 1$), in order to compare the experimental results with those available in the literature for single piers.

3. Experimental Setup and Procedures

The experiments have been carried out at the Civil Engineering School hydraulics laboratory at the University of Castilla-La Mancha (UCLM), Spain. The 30 m-long and 75 cm-wide tilting flume described by Chreties et al. [22] was used.

The single pier (case $m = n = 1$) or the pile group model (considering always $m = 3$ and $n = 2$) was placed in a recess box about 20 meters downstream of the beginning of the flume. In all cases, $d = 6.3$ cm. The piles were built in plastic and filled with cement to ensure their stability. The bed sediment used is a quartz sand with $\rho_s = 2650$ kg/m³, $d_{50} = 1.65$ mm and granulometric dispersion $\sigma_g = 1.27$ (< 1.3 so that the sediment can be considered as uniform). Parameter Γ , which appears in (4), had a range of $2 \leq \Gamma \leq 3$. This is a usual range in engineering practice and group effects are likely to play a role according Ataie-Ashtiani and Beheshti [23] results for local scour in unprotected pile groups with zero skew angle. For $\Gamma > 3$, the group effect is negligible and for $\Gamma = 2$ the scour depth is 25% higher than that for the single pier.

The riprap mattress configuration used in the experimental campaign is shown in Figure 3. The medium size of the riprap blocks, d_{r50} , was always $d_{r50} = 16.44$ mm, which proved to resist shear failure in all cases. Winnowing failure

was avoided by using a synthetic flexible filter between the riprap and the sand bed below in the riprap zone. Mattress thickness, t , was set following recommendations as three times the block size, that is, $t = 3d_{r50}$. The top of the riprap layer was leveled with the surrounding bed. In the live bed experiments (i.e., $I = 1.3$ in Table 1), the bed-form height was measured upstream the pile group. It was checked to be $\lesssim 2$ cm, being the mattress thickness almost 5 cm. Within the scour hole, the dynamics of the sediment transport is modified, and the amplitude of the bed forms was slightly increased. In any case, it was verified that bed-form undermining did not occur. In fact, the whole influence of the bed forms in the problem was shown to be small (as shown in the following section). For live-bed experiments it was also checked that bed degradation is negligible at the working zone (which is 20 meters downstream the beginning of the flume).

For a given mattress width, w , and Γ , the volume of riprap stones was calculated from Figure 3, taking into account that $t = 3d_{r50}$. A flexible plastic plate was inserted vertically in the sand bed along the external perimeter of the idealized riprap mattress, and the same volume of sand was carefully removed from the space the stones were to fill. After deploying the filter, the volume of riprap was finally poured into the excavated sand bed, ensuring that the top level was the same as the surrounding sand bed. In all the tests, a row of red-painted stones were carefully hand-placed around each individual pile (see Figure 4(a)).

Once the pile group and riprap mattress were in position, the flume was slowly filled to the top with water and then driven to get (in this order) the desired flow rate and water depth. The water depth, controlled through a tail-gate downstream, was chosen to obtain the desired h/d , in expression (4), within the range $1.5 \leq h/d \leq 2.5$. The flow rate, controlled with an electromagnetic flowmeter with an accuracy of 1.1%, was set so as to get $I = 1$ or 1.3 (Table 1). In computing u_c , the expression by Neil [24] was considered. The maximum depth scour into scour holes was measured using a point gage after 1, 2, 5, 7.5, 10, 15, 20, 30, 45, and 60 minutes from the beginning, then every hour during the first 12 hours and less frequently after the first 12 hours.

Two different kinds of experiments were carried out: (a) canonical tests (C1 to C7), where $I = 1$ and (b) live bed tests (L1 to L18), where $I = 1.3$. For canonical tests, “C”, the flume slope was set at 0.07%, while for the live bed tests, “L”, the slope was set at 0.11%. In both cases it was assumed that edge failure occurred when at least one red-painted stone was dislodged from its original position (Figure 4(b)). Canonical experiments were run until edge failure occurred (“fail” in Table 1) or until Melville and Chiew [20] equilibrium criteria were satisfied for the scour developed at the bed around the mattress (i.e., the scour depth in 24 hours less than 5% of the pier diameter d). If “equilibrium” was reached and the red stones remained unaffected, the mattress was considered to resist (“no fail” in Table 1). For the live-bed tests, experiments were stopped if the mattress failed (i.e., “fail”) or after 24 hours (“no fail”), since under weak live conditions the (dynamical) equilibrium has shown to be reached much faster [18].

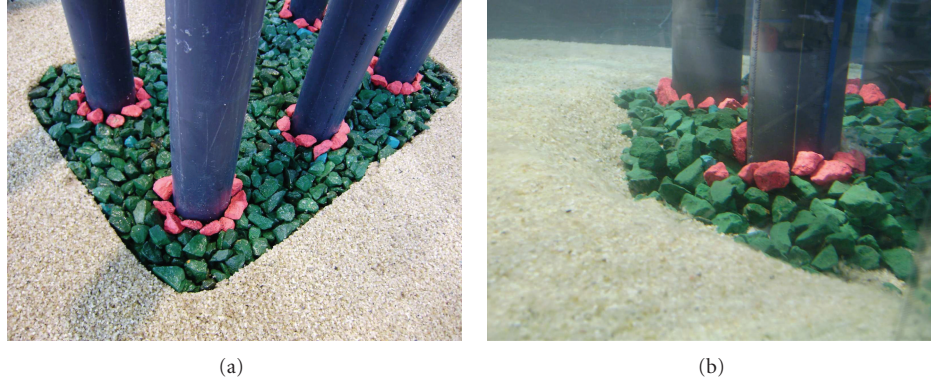


FIGURE 4: Edge failure test: experimental setup (a) and block dislodgement (b).

TABLE 1: Experimental conditions and results for pile groups and single piers.

Test	Model	Γ	I	h/d	w/d	result	Duration (h)
L1	Group	3	1.3	1.5	1.11	No fail	24
L2	Group	3	1.3	1.5	0.95	No fail	24
L3	Group	3	1.3	1.5	0.79	Fail	5
L4	Group	3	1.3	2.0	1.11	No fail	24
L5	Group	3	1.3	2.0	0.95	Fail	19
L6	Group	3	1.3	2.5	1.27	No fail	24
L7	Group	3	1.3	2.5	1.11	No fail	24
L8	Group	3	1.3	2.5	0.95	Fail	4
L9	Group	2	1.3	1.5	0.95	No fail	24
L10	Group	2	1.3	1.5	0.79	Fail	1
L11	Group	2	1.3	2.5	1.11	No fail	24
L12	Group	2	1.3	2.5	0.95	No fail	24
L13	Group	2	1.3	2.5	0.79	Fail	5
L14	Single	—	1.3	2.5	0.95	No fail	24
L15	Single	—	1.3	2.5	0.79	Fail	4
L16	Single	—	1.3	1.5	0.95	No fail	24
L17	Single	—	1.3	1.5	0.79	No fail	24
L18	Single	—	1.3	1.5	0.63	Fail	1
C1	Group	3	1.0	2.0	0.95	No fail	120
C2	Group	3	1.0	2.0	0.79	Fail	24
C3	Group	3	1.0	2.5	0.95	No fail	117
C4	Group	3	1.0	2.5	0.79	Fail	68
C5	Group	3	1.0	2.5	0.63	Fail	1
C6	Single	—	1.0	2.5	0.95	No fail	110
C7	Single	—	1.0	2.5	0.79	Fail	24

If, under given flow conditions, a mattress with a given width w resisted, a new width one centimeter smaller was tested in order to find the largest failing width and the minimum stable one.

4. Experimental Results and Discussion

The description of riprap edge failure observed in the experimental campaign corresponds, essentially, to that for single piers as described by Unger and Hager [1].

Table 1 shows the main features of each experiment. Recalling expression (4), it includes w/d , $I = u/u_c$, h/d and Γ (Γ only for the tests for pile groups). The table also describes whether the mattress failed or not as well as the experiment duration. A total of 18 tests were carried out for pile groups (5 of them canonical, “C”) and 7 for single piers (2 canonical ones).

In order to show the implications of setting $I = 1.3$ (L-tests) instead of $I \approx 1$ (C-tests) on the required time, Figure 5 shows the time history of the scour for tests L6 to L8 and C3. These four tests share $h/d = 2.5$ and $\Gamma = 3$. Also, tests

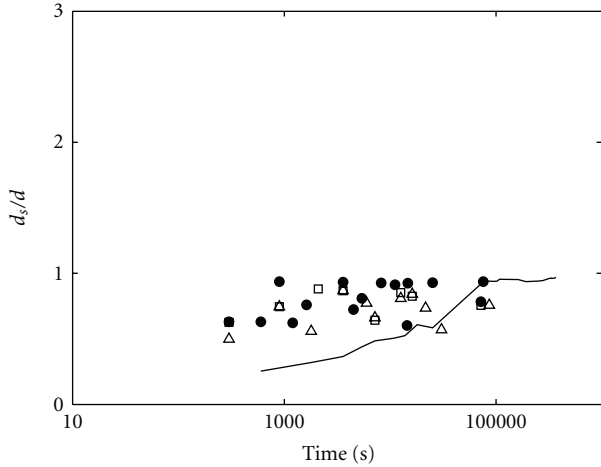


FIGURE 5: Canonical and live-bed results for $\Gamma = 3$. $I = 1$, $w/d = 0.95$ (line); $I = 1.3$, $w/d = 0.95$ (black circles); $I = 1.3$, $w/d = 1.11$ (squares); $I = 1.3$, $w/d = 1.27$ (triangles).

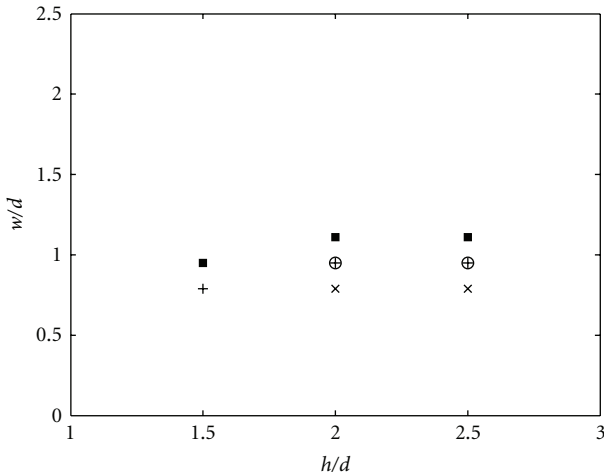


FIGURE 6: Canonical and live-bed results for the pile group with $\Gamma = 3$. $I = 1.3$ no fail (black squares); $I = 1.3$ fail (+); $I = 1$ no fail (circles); $I = 1$ fail (crossed).

L6 to L8 have $I = 1.3$ (with different w/d), while $I \approx 1$ for test C3. From Figure 5, several aspects are to be noted: first, the equilibrium depth for C3 is $d_{se}/d \approx 0.97$, notably smaller than if there had been no protection ($d_{se}/d \approx 2.4$ according to Melville [18]); secondly, and more interestingly for our purposes, the maximum scour depths, normalized by d , for tests L6 to L8, are 0.87, 0.88, and 0.94, respectively (noting that the scour depths now oscillate due to the passage of bed-forms). Hence, the aim of using $I \approx 1$ being to obtain the worse scour conditions in the surrounding bed mattress, using $I = 1.3$ will obtain similar conditions (significantly, the difference between L8 and C3, as those also sharing $w/d = 0.95$, is just 3%). Finally, regarding time evolution, from Figure 5 it is clear that time evolution is much faster for L-tests: the maximum scour is already reached after ≈ 3000 s, that is, less than one hour. Together with the fact that bed-form undermining will be small, as shown below, these

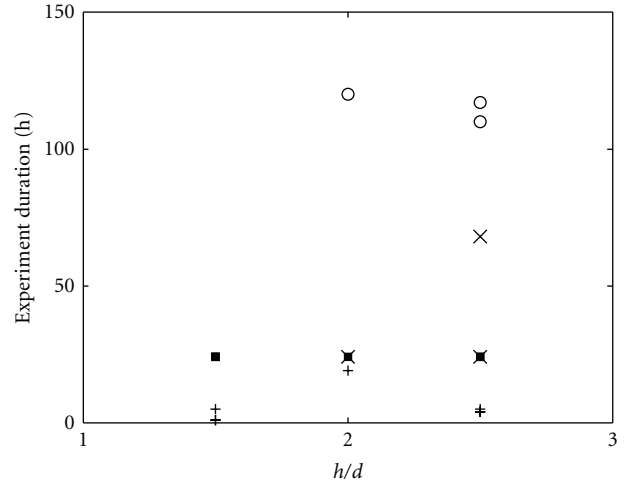


FIGURE 7: Experimental duration reduction. Canonical and live-bed experiments. $I = 1.3$ no fail (black squares); $I = 1.3$ fail (+); $I = 1$ no fail (circles); $I = 1$ fail (crossed).

results justify the use of $I = 1.3$ for speeding up riprap edge failure experiments in pile groups.

One main experimental result validating the use of live-bed tests is plotted in Figure 6. This figure shows, as a function of h/d , the results obtained for pile groups with $\Gamma = 3$ using $I \approx 1$ (C-tests) and $I = 1.3$ (L-tests). The minimum stable and maximum failing widths are plotted. As depicted from the figure, the results are similar and using L-tests fall slightly on the safety side. Because in L-tests there is sediment transport, bed-form undermining can have some (small) influence which makes the results slightly on the safety side.

We remark that L-tests are much shorter than canonical ones, and here comes the main advantage. This fact is stressed in Figure 7, showing the experimental time for C- and L-tests for all the experiments in Table 1. The longer tests (those where the mattress resists) took around 120 h for C-tests and only 24 h for the L-tests. Moreover, the results in Figure 5 suggest that this time could have been further reduced to few hours.

To further validate the use of weak live-bed conditions ($I = 1.3$), Figure 8 shows the results obtained for single piers (L14 to L18, C6 and C7) together with the upper and lower limits proposed by Lauchlan [26] (also see Melville et al. [25]), that consider

$$1.0 \leq \frac{w}{d} \leq 1.5. \quad (5)$$

First, the results using L- and C-tests in Figure 8 are, as in Figure 6, similar (in fact, now they coincide for $h/d = 2.5$, the only case where they can be compared). Secondly, our experimental results fall slightly below the lower limit proposed by Lauchlan [26], that is, $w/d = 1.0$. However, we recall that the expression by Lauchlan [26] is an envelope of the experimental data.

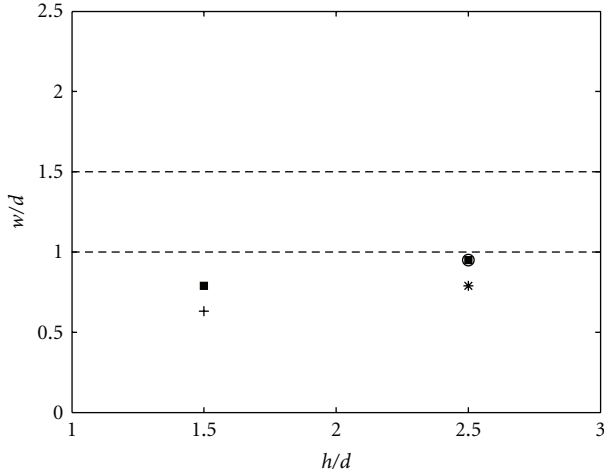


FIGURE 8: Canonical and live-bed results for the single pier compared with the expression by Melville et al. [25] upper and lower limits (dashed line). $I = 1.3$ no fail (black squares); $I = 1.3$ fail (+); $I = 1$ no fail (circles); $I = 1$ fail (crossed).

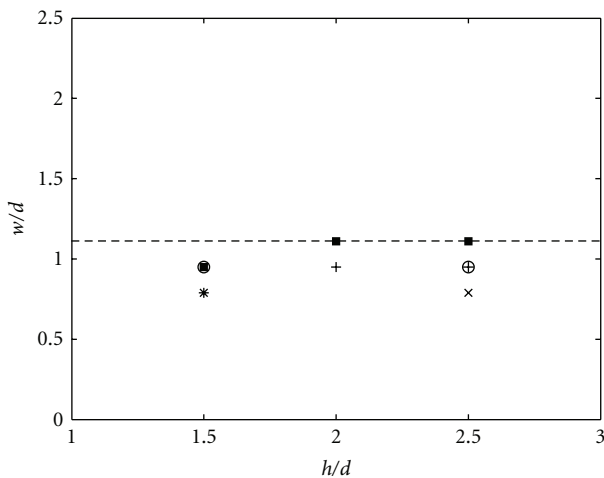


FIGURE 9: Experimental results for pile groups and proposed expression (7): $w/d = 1.11$ (dashed line). $\Gamma = 3$ no fail (black squares); $\Gamma = 3$ fail (+); $\Gamma = 2$ no fail (circles); $\Gamma = 2$ fail (crossed).

Finally, recalling expression (4) and recognizing that we are considering the most demanding situation in terms of flow intensity, we can write

$$\frac{w}{d} = \phi\left(\frac{h}{d}, \Gamma\right), \quad (6)$$

and, from the experimental data, we can give an expression for ϕ in our range. Figure 9 shows the experimental results to be used (all data for the pile group). From Figure 9, w/d has a weak dependence on both Γ and h/d (for $h/d \leq 2$). This is relatively unsurprising: on the one hand, although there is no clear consensus, group effects are usually small for $\Gamma \geq 2$; on the other hand, for $h/d \geq 2$ essentially we have “narrow piles” and, since we normalize w with d , the role of h/d becomes negligible [18]. The above is in good agreement

with the results by Simarro et al. [14] for riprap block design. The proposed expression is simply

$$\frac{w}{d} = 1.1, \quad (7)$$

for $2 \leq \Gamma \leq 3$, $1.5 \leq h/d \leq 2.5$, $d_{50}/d = 0.026$, $d_{r50}/d = 0.26$, $m = 3$, $n = 2$, and for zero skew angle. The above expression should also work well, in accordance with the arguments given above, for other values of $d_{50}/d = 0.026$ and $d_{r50}/d = 0.26$; for $h/d > 2.5$ and for $\Gamma > 3$.

5. Concluding Remarks

Using $I = 1.3$ instead of $I = 1$, the duration of experiments to assess required riprap mattress’ width to resist edge failure can be significantly reduced. Although we are mixing two different mechanisms (edge and weak bed-form undermining), the influence of the later appears to be small and gives results on the safety side, therefore justifying the use of weak live-bed conditions. An expression for the riprap width is given for a given pile group geometry, where $m = 3$ and $n = 2$.

Acknowledgments

C. Chreties was supported by the Agencia Nacional de Investigación e Innovación (ANII) Uruguay. G. Simarro is supported by the Spanish government through Ramón y Cajal program. All three authors thank Eduardo Diaz for his help in preparing the experiments.

References

- [1] J. Unger and W. H. Hager, “Riprap failure at circular bridge piers,” *Journal of Hydraulic Engineering*, vol. 132, no. 4, pp. 354–362, 2006.
- [2] J. E. Pagan-Ortiz, *Stability of Rock Riprap for Protection at the Toe Abutments Located at the Floodplain*, Federal Highway Administration, U.S. Department of Transportation, Washington, DC, USA, 1991.
- [3] B. Melville, S. van Ballegooy, S. Coleman, and B. Barkdoll, “Countermeasure toe protection at spill-through abutments,” *Journal of Hydraulic Engineering*, vol. 132, no. 3, pp. 235–245, 2006.
- [4] B. W. Melville, S. van Ballegooy, S. E. Coleman, and B. Barkdoll, “Riprap size selection at wing-wall abutments,” *Journal of Hydraulic Engineering*, vol. 133, no. 11, pp. 1265–1269, 2007.
- [5] A. H. Cardoso and C. M. S. Fael, “Protecting vertical-wall abutments with riprap mattresses,” *Journal of Hydraulic Engineering*, vol. 135, no. 6, pp. 457–465, 2009.
- [6] A. H. Cardoso, G. Simarro, O. Le Doucen, and A. Schleiss, “Sizing of riprap for spill-through abutments,” in *Proceedings of the Institution of Civil Engineers: Water Management*, vol. 163, no. 10, pp. 499–507, November 2010.
- [7] A. H. Cardoso, G. Simarro, C. Fael, O. Le Doucen, and A. J. Schleiss, “Toe protection for spill-through and vertical-wall abutments,” *Journal of Hydraulic Research*, vol. 48, no. 4, pp. 491–498, 2010.
- [8] Yee-Meng Chiew, “Mechanics of riprap failure at bridge piers,” *Journal of Hydraulic Engineering*, vol. 121, no. 9, pp. 635–643, 1995.

- [9] Y. M. Chiew and F. H. Lim, "Failure behavior of riprap layer at bridge piers under live-bed conditions," *Journal of Hydraulic Engineering*, vol. 126, no. 1, pp. 43–55, 2000.
- [10] C. S. Lauchlan and B. W. Melville, "Riprap protection at bridge piers," *Journal of Hydraulic Engineering*, vol. 127, no. 5, pp. 412–418, 2001.
- [11] Y. M. Chiew, "Local scour and riprap stability at bridge piers in a degrading channel," *Journal of Hydraulic Engineering*, vol. 130, no. 3, pp. 218–226, 2004.
- [12] N. Vittal, U. C. Kothyari, and M. Haghghat, "Clear-water scour around bridge pier group," *Journal of Hydraulic Engineering*, vol. 120, no. 11, pp. 1309–1319, 1994.
- [13] A. R. Zarrati, M. Nazahira, and M. B. Mashahir, "Reduction of local scour in the vicinity of bridge pier groups using collars and riprap," *Journal of Hydraulic Engineering*, vol. 132, no. 2, pp. 154–162, 2006.
- [14] G. Simarro, C. Chreties, and L. Teixeira, "Riprap sizing for pile groups," *Journal of Hydraulic Engineering*, vol. 137, no. 12, pp. 1676–1679, 2012.
- [15] F. Ballio, A. Radice, and S. Dey, "Temporal scales for live-bed scour at abutments," *Journal of Hydraulic Engineering*, vol. 136, no. 7, Article ID 003007QHY, pp. 395–402, 2010.
- [16] S. E. Coleman, "Clearwater local scour at complex piers," *Journal of Hydraulic Engineering*, vol. 131, no. 4, pp. 330–334, 2005.
- [17] G. Simarro, L. Teixeira, and A. H. Cardoso, "Flow intensity parameter in pier scour experiments," *Journal of Hydraulic Engineering*, vol. 133, no. 11, pp. 1261–1264, 2007.
- [18] B. W. Melville, "Pier and abutment scour: integrated approach," *Journal of Hydraulic Engineering*, vol. 123, no. 2, pp. 125–136, 1997.
- [19] A. H. Cardoso and R. Bettess, "Effects of time and channel geometry on scour at bridge abutments," *Journal of Hydraulic Engineering*, vol. 125, no. 4, pp. 388–398, 1999.
- [20] B. W. Melville and Y. M. Chiew, "Time scale for local scour at bridge piers," *Journal of Hydraulic Engineering*, vol. 125, no. 1, pp. 59–65, 1999.
- [21] G. Simarro, C. M.S. Fael, and A. H. Cardoso, "Estimating equilibrium scour depth at cylindrical piers in experimental studies," *Journal of Hydraulic Engineering*, vol. 137, no. 9, pp. 1089–1093, 2011.
- [22] C. Chreties, G. Simarro, and L. Teixeira, "New experimental method to find equilibrium scour at bridge piers," *Journal of Hydraulic Engineering*, vol. 134, no. 10, pp. 1491–1495, 2008.
- [23] B. Ataie-Ashtiani and A. A. Beheshti, "Experimental investigation of clear-water local scour at pile groups," *Journal of Hydraulic Engineering*, vol. 132, no. 10, pp. 1100–1104, 2006.
- [24] C. R. Neil, "Mean velocity criterion for scour of coarse uniform bed material," in *Proceedings of the 12th IAHR Congress*, pp. 46–54, Fort Collins, Colo, USA, 1967.
- [25] B. W. Melville, S. E. Coleman et al., *Bridge Scour*, Water Resources Publications, LLC, Colo, USA, 2000.
- [26] C. S. Lauchlan, *Pier scour countermeasures*, Ph.D. thesis, Civil and Resources Engineering, University of Auckland, Auckland, New Zealand, 1999.